



UNIVERSIDAD NACIONAL AUTÓNOMA DE MÉXICO
PROGRAMA DE MAESTRÍA Y DOCTORADO EN INGENIERÍA
INGENIERÍA CIVIL - ESTRUCTURAS

NUMERICAL APPROXIMATION OF THE NON-LINEAR BEHAVIOUR OF MASONRY
STRUCTURES THROUGH THE FINITE ELEMENT METHOD:
A COMPUTATIONALLY EFFICIENT STRATEGY

T E S I S

QUE PARA OPTAR POR EL GRADO DE:
DOCTOR EN INGENIERÍA

PRESENTA:

HÉCTOR RODRIGO AMEZCUA RIVERA

TUTOR PRINCIPAL

DR. A. GUSTAVO AYALA MILIÁN, INSTITUTO DE INGENIERÍA - UNAM

COMITÉ TUTOR

DR. FERNANDO PEÑA MONDRAGÓN, INSTITUTO DE INGENIERÍA – UNAM

DR. JAIME RETAMA VELASCO, FES ARAGÓN – UNAM

DR. AGUSTÍN ORDUÑA BUSTAMANTE, FACULTAD DE INGENIERÍA CIVIL – UCOL

DR. GELACIO JUÁREZ LUNA, UNIVERSIDAD AUTÓNOMA METROPOLITANA

CIUDAD DE MÉXICO, ENERO 2023



Universidad Nacional
Autónoma de México

Dirección General de Bibliotecas de la UNAM

Biblioteca Central



UNAM – Dirección General de Bibliotecas
Tesis Digitales
Restricciones de uso

DERECHOS RESERVADOS ©
PROHIBIDA SU REPRODUCCIÓN TOTAL O PARCIAL

Todo el material contenido en esta tesis esta protegido por la Ley Federal del Derecho de Autor (LFDA) de los Estados Unidos Mexicanos (México).

El uso de imágenes, fragmentos de videos, y demás material que sea objeto de protección de los derechos de autor, será exclusivamente para fines educativos e informativos y deberá citar la fuente donde la obtuvo mencionando el autor o autores. Cualquier uso distinto como el lucro, reproducción, edición o modificación, será perseguido y sancionado por el respectivo titular de los Derechos de Autor.

JURADO ASIGNADO:

Presidente: DR. FERNANDO PEÑA MONDRAGÓN

Secretario: DR. JAIME RETAMA VELASCO

1 er. Vocal: DR. AMADO GUSTAVO AYALA MILIÁN

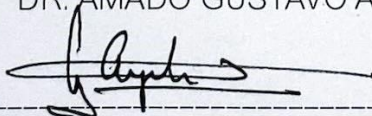
2 do. Vocal: DR. AGUSTÍN ORDUÑA BUSTAMANTE

3 er. Vocal: DR. GELACIO JUÁREZ LUNA

Lugar o lugares donde se realizó la tesis: INSTITUTO DE INGENIERÍA, UNAM

TUTOR DE TESIS:

DR. AMADO GUSTAVO AYALA MILIÁN



FIRMA

*To my parents, Ramona and Armando,
and, specially, to Itzel*

Acknowledgments

First, I would like to express my total admiration and deepest gratitude to Dr. Gustavo Ayala for his guidance during all these years. It was a real honor working under his supervision. His advice and teachings definitely transcend the academic growth and reach the personal one. I am especially grateful for his concern about my future. I will always be proud to mention, wherever I am, that I am his disciple.

I want to thank my family, especially my parents, Ramona Rivera and Armando Amezcua, I have never felt able to find the words that are enough to thank them for everything they have given me and to let them know how fortunate I am to be their son. I am totally convinced that this is their achievement. Also, all my gratitude and love goes to my life partner Itzel Núñez, who has been both my academic and emotional support during the development of this work. She, despite the distance, knew how to be present in difficult moments. I really appreciate all her sincere concern in every aspect of my life.

I am totally grateful to the members of my thesis committee: Dr. Agustín Orduña, Dr. Gelacio Juárez, Dr. Jaime Retama and Dr. Fernando Peña, for their insightful comments and patience for reviewing this document.

Thanks to my friends Isaías Hernández and Carlos Vargas for always been there in both social and academic interactions. Additionally, I would like to thank my colleagues from the research group of Dr. Ayala for all the moments we shared in the office. Special thanks to Juan Gutiérrez for always being willing to discuss my work and for sharing his valuable ideas.

This thesis was carried out at the *Instituto de Ingeniería (IINGEN)* of the *Universidad Nacional Autónoma de México (UNAM)* under the supervision of Dr. Gustavo Ayala. This research was possible thanks to the scholarship given by the *Consejo Nacional de Ciencia y Tecnología (CONACyT)*. Also, my gratitude goes to the General Directorate for Affairs of Academic Personnel (**DGAPA-UNAM**), for the economical support through the project titled “*Formulación e implementación de un nuevo modelo de elementos finitos y su aplicación al análisis no-lineal de estructuras de mampostería*” (**PAPIIT - IN106917**).

Abstract

Historically, masonry has been one of the most used structural materials around the world. It is well known that the mechanical behaviour of masonry is complex, despite its relatively easy construction process. Nowadays, there are many strategies to address this problem for both ancient and modern masonry constructions. Nevertheless, these strategies are either computationally demanding or based on some simplifying hypothesis that are only valid under certain conditions.

This dissertation presents a proposal for employing reduced numerical integration in the formulation of the 4-node quadrilateral solid finite element to perform non-linear analysis of structures. The proposed procedure allows the possibility of evaluating a given constitutive model only at one integration point, achieving an attractive computational cost reduction. A validation of the proposal is included and discussed throughout the document.

To represent the non-linear mechanical behaviour of masonry a plastic-damage model is implemented along with the proposed sub-integration scheme. Also, in order to have a full and computationally efficient strategy to determine the behaviour of masonry structures, including its evolution to collapse, a homogenization technique with a macro-modelling approach is used. Several validation and application examples of masonry structures are studied using different constitutive models and comparing the computed results to the ones obtained by a full integration scheme and, also, to experimental ones. These comparisons are discussed extensively all along this thesis.

In order to have an alternative, the sub-integration scheme is complemented with a sequentially linear analysis procedure. A computational tool to apply the resulting strategy is presented, validated and discussed. Finally the conclusions of this work, derived from the formulation of the method proposed and the analysis of the obtained results, are given.

Resumen

Históricamente, la mampostería ha sido uno de los materiales estructurales más utilizados en todo el mundo. Es bien sabido que el comportamiento mecánico de la mampostería es complejo, a pesar de que su proceso constructivo es relativamente fácil. Hoy en día, existen muchas estrategias para abordar este problema tanto en las construcciones de mampostería antiguas como en las modernas. Sin embargo, estas estrategias son computacionalmente exigentes o se basan en algunas hipótesis simplificadoras que solo son válidas bajo ciertas condiciones.

En esta tesis se presenta una propuesta para emplear integración numérica reducida en la formulación del elemento finito sólido cuadrilátero de 4 nodos para la ejecución de análisis no lineales de estructuras. El procedimiento propuesto permite la posibilidad de evaluar un determinado modelo constitutivo en un solo punto de integración, logrando una atractiva reducción del costo computacional. Se incluye una validación de la propuesta y se discute a lo largo del documento.

Para representar el comportamiento mecánico no lineal de la mampostería se implementa un modelo de daño plástico en conjunto el esquema de integración reducida propuesto. Asimismo, para tener una estrategia completa y computacionalmente eficiente para determinar el comportamiento de las estructuras de mampostería, involucrando su evolución hasta el colapso, se emplea una técnica de homogeneización con un enfoque de macro-modelado. Se estudian varios ejemplos de validación y aplicación de estructuras de mampostería utilizando diferentes modelos constitutivos y comparando los resultados calculados con los obtenidos por un esquema de integración completo y, además, con experimentos. Estas comparaciones se discuten ampliamente a lo largo de esta tesis.

Para tener una alternativa, el esquema de integración reducida se complementa con un procedimiento de análisis lineales secuenciales. Se presenta, valida y discute una herramienta computacional para aplicar la estrategia resultante. Finalmente se establecen las conclusiones de este trabajo, derivadas de la formulación del método propuesto y del análisis de los resultados obtenidos.

Contents

Acknowledgements	iii
Abstract	v
Resumen	vii
List of Figures	xiii
List of Tables	xix
1 Introduction	1
1.1 Problem statement	2
1.2 Objectives	6
1.3 Outline of the thesis	7
2 Reduced integration in the FEM	9
2.1 Introduction	9
2.2 Numerical integration in the FEM	9
2.2.1 Full integration (FI)	10
2.2.2 Reduced integration (RI)	11
2.3 Stabilization procedure	13
2.3.1 Formulation	13
2.3.2 Mathematical validation	16
2.3.3 Numerical implementation	17
2.4 Validation examples	17
2.4.1 Linear analysis	17
2.4.2 Algebraic eigen-value problem	20
2.4.3 Non-linear analysis	20
2.4.3.1 Cook's membrane	21
2.4.3.2 Shear wall with openings	24

2.4.3.3	Monastery of São Vicente de Fora	27
2.4.3.4	Typical colonial church of Puebla, Mexico	29
2.4.4	Experimental data	31
2.4.4.1	Wall panel	32
2.4.4.2	Arcade of São Vicente de Fora	35
3	Non-linear behaviour of masonry	39
3.1	Introduction	39
3.2	Numerical analysis of masonry by FEM	39
3.2.1	Modelling strategies	40
3.2.2	Mechanical behaviour	41
3.3	Plastic-damage constitutive model	42
3.3.1	Formulation	42
3.3.1.1	Internal variables (ϵ^p , κ^p y c)	42
3.3.1.2	Plastic yield criterion (\mathbb{F})	43
3.3.1.3	Angle of internal friction (ϕ)	44
3.3.1.4	Angle of dilatancy (ψ)	44
3.3.1.5	Hardening plastic parameter (A)	44
3.4	Numerical implementation	45
3.5	Debugging tests	47
3.5.1	Behaviour tests	47
3.5.2	Behaviour tests with SRI scheme	50
3.5.2.1	Unidimensional test	50
3.5.2.2	Bidimensional test	51
3.5.2.3	Internal variables evolution	53
3.6	Validation (macro-models)	54
3.7	Homogenization	57
3.7.1	Elastic parameters	58
3.7.1.1	Elasticity modulus	59
3.7.1.2	Shear modulus	59
3.7.1.3	Poisson's ratio	60
3.7.2	Numerical implementation	61
3.7.2.1	Debugging test	61
3.8	Homogenized plastic flow	62
3.8.1	Transformation spaces	63
3.8.2	Numerical implementation	64
3.8.2.1	Debugging tests	64

4	Application through a plastic-damage constitutive model	67
4.1	Introduction	67
4.2	Shear walls (TU Eindhoven)	67
4.2.1	Shear walls without openings	68
4.2.2	Shear walls with opening	71
5	Application through sequentially linear analysis	75
5.1	Introduction	75
5.2	Procedure for proportional loading	75
5.3	Saw-tooth softening law	76
5.4	Combined procedure of SLA with SRI	77
5.4.1	Numerical implementation	78
5.4.2	Validation examples	80
5.5	Mesh regularization procedure	83
5.5.1	Validation examples	84
5.6	Application	86
5.6.1	Variable cross-section notched beam	86
5.6.2	Notched beam	88
6	Conclusions	93
	References	97

List of Figures

1.1	Flow diagram for solving a problem from an engineering point of view	1
1.2	Notched beam subjected to vertical displacements: hourglass effect <i>(a)</i> present and <i>(b)</i> controlled	3
2.1	4-node quadrilateral finite element	10
2.2	Stiffness matrix deformation modes obtained with FI	11
2.3	Stiffness matrix deformation modes obtained with RI	12
2.4	Stiffness matrix deformation modes obtained with SRI	16
2.5	User routine flowchart implemented in <i>FEAP</i> (Taylor, 2017)	18
2.6	Cook's membrane geometry and boundary conditions	19
2.7	Cook's membrane convergence to analytical solution in strain energy	19
2.8	Cook's membrane first deformation mode obtained with <i>(a)</i> FI, <i>(b)</i> RI and <i>(c)</i> SRI	20
2.9	Cook's membrane second deformation mode obtained with <i>(a)</i> FI, <i>(b)</i> RI and <i>(c)</i> SRI	20
2.10	Cook's membrane: <i>(a)</i> mesh <i>A</i> and <i>(b)</i> mesh <i>B</i>	21
2.11	Von Mises stress distribution at the end of the analysis for mesh <i>A</i> with <i>(a)</i> SRI and <i>(b)</i> FI; and for the mesh <i>B</i> with <i>(c)</i> SRI and <i>(d)</i> FI	22
2.12	Reaction-displacement diagram of the Cook's Membrane	23
2.13	Six intermediate analysis states of Von Mises stress distribution for mesh <i>B</i> with SRI at displacement of <i>(a)</i> 0.3 mm, <i>(b)</i> 2 mm, <i>(c)</i> 3 mm, <i>(d)</i> 4 mm, <i>(e)</i> 5 mm and <i>(f)</i> 7 mm	23
2.14	Computing time comparison for the non-linear analysis of the Cook's mem- brane	24
2.15	Shear wall with openings: <i>(a)</i> mesh <i>A</i> and <i>(b)</i> mesh <i>B</i>	25
2.16	Reaction-displacement diagram of the shear wall with openings	25
2.17	Six intermediate analysis states of Von Mises stress distribution for mesh <i>B</i> with SRI at displacement of <i>(a)</i> 5 mm, <i>(b)</i> 10 mm, <i>(c)</i> 15 mm, <i>(d)</i> 20 mm, <i>(e)</i> 25 mm and <i>(f)</i> 35 mm	25

LIST OF FIGURES

2.18	Computing time comparison for the non-linear analysis of the shear wall with openings	26
2.19	Von Mises stress distribution for mesh <i>A</i> with (a) SRI and (b) FI; and for the mesh <i>B</i> with (c) SRI and (d) FI	26
2.20	Full-scale model at the ELSA Laboratory (Pegon et al., 2001)	27
2.21	Arcade of the Monastery of São Vicente de Fora: (a) mesh <i>A</i> and (b) mesh <i>B</i>	28
2.22	Reaction-displacement diagram of the arcade	28
2.23	Computing time comparison for the non-linear analysis of the arcade	28
2.24	Von Mises stress distribution for mesh <i>A</i> with (a) SRI and (b) FI; and for the mesh <i>B</i> with (c) SRI and (d) FI	29
2.25	Experimental model of a typical colonial church of Puebla, Mexico (Chávez, 2010)	30
2.26	First three modal shapes of the facade	30
2.27	Reaction-displacement numerically approximated curves	31
2.28	Computing time comparison for the non-linear analysis of the church’s facade	31
2.29	Wall panel tested in Heavy Structures Laboratory (Giamundo et al., 2014)	32
2.30	Mesh employed in the analysis of the wall panel	32
2.31	Reaction-displacement experimental and approximated curves	33
2.32	Computing times for the non-linear analyses of the wall panel	33
2.33	Six intermediate analysis states of principal stresses with SRI at displacement of (a) 0.112 mm, (b) 0.144 mm, (c) 0.240 mm, (d) 0.512 mm, (e) 0.704 mm and (f) 1.08 mm	34
2.34	Comparison between (a) the principal stresses distribution obtained with SRI and (b) smeared crack patterns numerically approximated by Giamundo et al. (2014)	34
2.35	Damage observed in the experiment (Giamundo et al., 2014)	34
2.36	Test set-up of the model (Ambrosetti, 2000)	35
2.37	Meshes employed in the analysis: (a) mesh <i>A</i> and (b) mesh <i>B</i>	35
2.38	Analysis steps: (a) vertical loads and (b) lateral displacements	36
2.39	Experimental and numerical displacement-reaction curves	36
2.40	Computing times for the non-linear analyses of the Arcade of São Vicente de Fora	37
2.41	Six intermediate analysis states of principal stresses distribution with SRI at displacement of (a) 0.3 mm, (b) 3 mm, (c) 4 mm, (d) 6 mm, (e) 15 mm and (f) 22.5 mm	37
2.42	Comparison between (a) the principal stresses distribution obtained with SRI and (b) damage observed in experiment at displacement of 30 mm (Ambrosetti, 2000)	38

3.1	Detailed micro-modelling strategy for masonry	40
3.2	Macro-modelling strategy for masonry	41
3.3	Yield surface transformation considering: (a) isotropic hardening and (b) kinematic hardening (Oller, 2001)	45
3.4	Plastic-damage constitutive model algorithm (Oller, 2001)	46
3.5	Radial return algorithm for the implicit integration of the constitutive equation	47
3.6	Flow diagram of plastic-damage constitutive model implementation in <i>FEAP</i> (Taylor, 2017)	48
3.7	Plastic-damage constitutive model behaviour test: (a) to compression y (b) to tension	49
3.8	Evolution of the internal variables: (a) plastic-damage variable, κ^p , and (b) cohesion, c	49
3.9	4-node quadrilateral finite element proposed for the unidimensional test	50
3.10	Unidimensional tension test	50
3.11	Transformation of the uniaxial strength measured in laboratory to the uniaxial strength employed in the plastic-damage constitutive model (Oller, 2001): (a) uniaxial strength in function of plastic deformation, (b) uniaxial strength in function of the plastic damage variable and (c) the cohesion depending of the plastic damage variable	51
3.12	Proposed mesh for the behaviour tests with the SRI scheme	51
3.13	Displacement-reaction diagram of the 4-element mesh for (a) tension, (b) compression and (c) shear displacements impositions	52
3.14	State of the internal variables at the end of the analysis (shear displacement imposition): (a) plastic-damage variable and and (b) cohesion	53
3.15	Displacement-reaction diagram	53
3.16	State of the internal variables at the end of the analysis: (a) plastic-damage variable and and (b) cohesion	54
3.17	Experiment of masonry wall conducted at Federal Institute of Technology in Zurich (ETH Zurich) (Lourenço, 1996)	55
3.18	Geometry of the specimen (dimensions in mm) (Lourenço, 1996)	55
3.19	Displacement-reaction diagram of the <i>W1</i> wall	56
3.20	Distribution of Von Mises stress at the end of the analysis	57
3.21	Damage patterns at the end of the experiment (Lourenço, 1996)	57
3.22	Basic masonry cell used for homogenization (López et al., 1998)	58
3.23	Flow diagram of the algorithms implemented in <i>FEAP</i> (Taylor, 2017)	61
3.24	Displacement-reaction diagram of the <i>W1</i> wall	62

LIST OF FIGURES

3.25	Schematic representation of the linear transformation for the isotropic an orthotropic spaces	63
3.26	Flow diagram of the algorithms implemented in <i>FEAP</i> (Taylor, 2017) . . .	64
3.27	Displacement-reaction diagram of the <i>W1</i> wall	65
3.28	Distribution of principal strains at the end of the analysis	65
4.1	Analysis steps of the shear wall without openings (JD) of TU Eindhoven: (a) pre-compression loads and (b) lateral displacement	68
4.2	Reaction-displacement experimental and numerical curves of the <i>J7D</i> wall .	69
4.3	Six intermediate analysis states of the plastic-damage variable at (a) 0.9 mm, (b) 1.35 mm, (c) 1.41 mm, (d) 1.50 mm, (e) 1.59 mm and (f) 1.80 mm	70
4.4	Final state of the constitutive model internal variables: (a) plastic-damage and (b) cohesion	70
4.5	Cracks observed at the end of the experiment on the wall <i>J7D</i> (Lourenço, 1996)	71
4.6	Geometry of the shear wall with openings of the TU Eindhoven	71
4.7	Reaction-displacement experimental and numerical curves of the <i>J2G</i> and <i>J3G</i> walls	72
4.8	Six intermediate analysis states of the plastic-damage variable at (a) 0.25 mm, (b) 0.50 mm, (c) 0.75 mm, (d) 1.00 mm, (e) 1.25 mm and (f) 7.00 mm	73
4.9	Final state of the constitutive model internal variables: (a) plastic-damage and (b) cohesion	73
4.10	Cracks observed at the end of the experiment on the walls (a) <i>J2G</i> and (b) <i>J3G</i> (Lourenço, 1996)	74
5.1	Softening in stress-strain curve (Rots, 2001b)	78
5.2	Flow diagram of the implemented algorithm	79
5.3	Screen capture of the developed software	79
5.4	Geometry of the notched beam	80
5.5	Mesh employed in the analysis of the notched beam	81
5.6	Reaction-displacement diagram for the notched beam (5 teeth)	81
5.7	Reaction-displacement diagram for the notched beam (10 teeth)	82
5.8	Reaction-displacement diagram for the notched beam (20 teeth)	82
5.9	Deformed configuration of the notched beam after the SLA-SRI procedure .	82
5.10	Underestimated area in the softening diagram through the saw-tooth approximation (Rots and Invernizzi, 2004)	83
5.11	Procedure for compensating the underestimated area in the softening diagram through the saw-tooth approximation (Rots and Invernizzi, 2004) . .	84
5.12	Reaction-displacement diagram for the notched beam (regularized, 5 teeth)	84

5.13	Reaction-displacement diagram for the notched beam (regularized, 10 teeth)	85
5.14	Reaction-displacement diagram for the notched beam (regularized, 20 teeth)	85
5.15	Geometry of the variable cross-section notched beam (Juárez and Ayala, 2010)	86
5.16	Mesh employed in the analysis of the variable cross-section notched beam	86
5.17	Reaction-displacement diagram for the variable cross-section notched beam	87
5.18	Reaction-displacement diagram for the variable cross-section notched beam (regularized)	88
5.19	Deformed configuration of the variable cross-section notched beam	88
5.20	Geometry of the notched beam (Juárez and Ayala, 2010)	89
5.21	Mesh employed in the analysis of the notched beam	89
5.22	Reaction-displacement diagram for the notched beam	90
5.23	Reaction-displacement diagram for the notched beam (regularized)	90
5.24	Deformed configuration of the notched beam	91
6.1	Computing-time reduction of the presented examples (comparison for same mesh density)	94
6.2	Computing-time reduction of the presented examples (comparison for different mesh density)	95

List of Tables

2.1	Comparison of a 4-node quadrilateral element deformation modes obtained with both FI and RI	13
2.2	Mechanical parameters considered in the analysis of the Cook's membrane .	21
2.3	Mechanical parameters considered in the analysis of the shear wall	24
2.4	Mechanical parameters considered in the analysis of the arcade	27
2.5	Mechanical parameters considered in the analysis of the church's facade . .	30
2.6	Mechanical parameters considered in the analysis of the wall panel	32
2.7	Experimental results for first cracking (Giamundo et al., 2014)	34
2.8	Mechanical parameters considered in the analysis of the arcade	36
3.1	Mechanical parameters considered for the bidimensional test	52
3.2	Mechanical parameters reported for the masonry wall	56
4.1	Mechanical parameters for the bricks considered in the analysis	68
4.2	Mechanical parameters for the mortar joints considered in the analysis . . .	69
5.1	Mechanical parameters considered for the stress-strain diagram of fig. 5.1 .	77
5.2	Mechanical parameters considered in the analysis of the notched beam . . .	81
5.3	Adjustment factors, k , for each model	84
5.4	Mechanical parameters considered in the analysis of the variable cross-section notched beam	87
5.5	Adjustment factor, k	87
5.6	Mechanical parameters considered in the analysis of the notched beam . . .	89
5.7	Adjustment factor, k	89

Introduction

Humans tend to both create and solve problems. Naturally, creating a problem is an easier task than solving it. In fact, several problems were created involuntarily and for some other problems its pure identification represent a problem itself. Whatever the reason, and as illogical as it may sound, efforts have been concentrated on solving problems rather than avoiding them.

Science and engineering are two useful tools to solve problems. Each of these tools has their own objective. While science is focused in providing new knowledge for understanding the problem, engineering is intended to apply this new knowledge to the solution of problems. In other words, science is rational creativity aimed at identifying and understanding problems and engineering is the approximation of their solution by controlling the error. Therefore, any problem that is attempted to be solved from an engineering point of view is supported in science.

Focusing on a real problem well identified and understood by science, the procedure to be followed by engineering in order to solve the problem is shown in fig. 1.1.

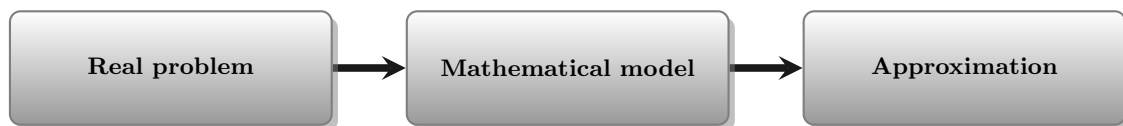


Figure 1.1. Flow diagram for solving a problem from an engineering point of view

Here, two main activities of every engineer can be identified by the arrows in the diagram. The first one corresponds to the translation of the problem to be solved into mathematical language, *i.e.*, the construction of the mathematical model. The second arrow is the approximation or, if possible, the solutions of the mathematical model.

For some well-studied problems, the mathematical model can be very close to reality. Actually, the constant evolution of science give us the possibility to build increasingly better mathematical models and, therefore, to recalculate its solution in order to obtain results closer to reality. Nevertheless, the more realistic the mathematical model, the more complex its solution or approximation. In fact, in some cases, even approximation is not

possible.

One strategy for solving these problems regards on the establishment of hypothesis to simplify the mathematical model. These simplifications allow the approximation of the solution of such a model. Other strategy, is the use of high-capacity computers which can achieve approximations of more mathematically complex problems. Both strategies have advantages and disadvantages and need to be carefully implemented. For example, the establishment of a not valid hypothesis implies that the problem that is actually solved is not the same that the original one. Additionally, the use of a high-capacity computers is related to the implementation of robust algorithms, capable of taking full advantage of it.

Thus, the flow diagram of fig. 1.1 is really an iterative process to find a close-enough to reality mathematical model that can be approximated by the available and applicable computational resources. Hence, higher computational resources and efficient algorithms allow the proposal of a mathematical model closer to the reality of the problem. The objective of this dissertation is to efficient the computational process of approximating the solution of a mathematical model that leads on the construction of a better one.

1.1 Problem statement

Non-linear structural analysis has become one of the most common challenges faced by structural engineers. Nowadays, it is implausible the accomplishment of the tasks involved in its application without the use of high-end computers and advanced numerical methods that are becoming more robust and efficient to improve the quality of the results. Nevertheless, performing a non-linear analysis is a complicated task, generally due to the mechanical characteristics of the composing materials and to the irregular geometry that is commonly present in both new and ancient structures. Most of the available solution strategies are based on the use of approximate numerical methods, such as the Finite Element Method (FEM). This method idealizes the irregular geometry of the structure as a discretized assemblage of elements of simpler geometry approximating the complex mechanical behaviour of the material by *ad hoc* constitutive models. As expected, the application of this solution strategy generally involves a high computational cost.

The use of computers in the execution of non-linear finite element analysis in all its stages, *i.e.*, pre-, actual- and post-processing, has encouraged the development of refined constitutive models which guarantee a better approximation of the real behaviour of the materials and, consequently, of the structures. However, the practical application of these models is not always feasible, since, in spite of the fact that computers are increasingly powerful, the computational cost of carrying out a non-linear analysis of a complex structure can be inconveniently high. Hence, the development of improved numerical procedures and solution strategies that reduce this computational cost is attractive to structural engineers and researchers.

One path for reducing the computational cost required to perform a non-linear analysis relies on the use of simplifying hypotheses regarding the overall behaviour of the problem,

which derives in the formulation of very straightforward numerical procedures. Despite the fact that in some applications the acceptance of such hypotheses is well or barely justified, in several other ones, its use may drastically impact the accuracy and even the usability of the obtained results.

Another approach to achieve a computational cost reduction, without compromising the quality of the results, is the use of low-order numerical integration rules in FEM analysis, *i.e.*, reduced numerical integration. The use of such a strategy is naturally attractive since the reduction in the number of calculations required in constructing the stiffness matrix. Furthermore, as it has been demonstrated in the work of Belytschko and Bachrach (1986), this type of procedures allows the possibility of using coarser meshes due to the inherited enrichment of the approximated results.

Nevertheless, as suggested by other studies, the use of reduced integration produces rank-deficient stiffness matrices which may lead to numerical instabilities and the appearance of the hourglass effect (Belytschko et al., 2013; Cook et al., 1989). Therefore, to avoid numerical issues when performing linear and non-linear analysis these instabilities need to be controlled. To illustrate this problem, an example of a notched beam subjected to vertical displacement imposition in which the appearance and control of the hourglass effect may be observed, is included in fig. 1.2.

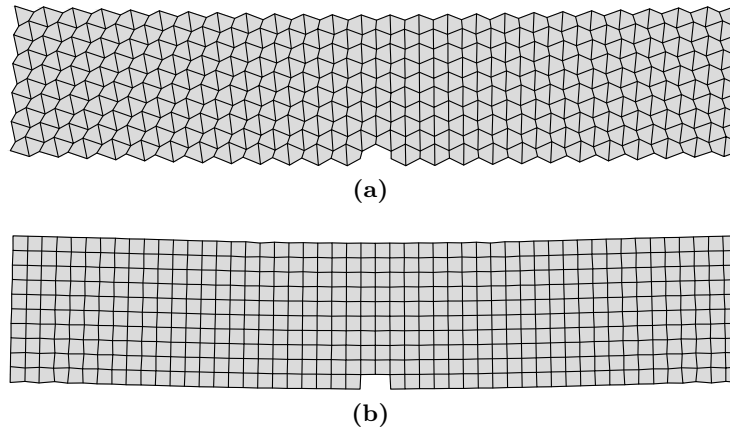


Figure 1.2. Notched beam subjected to vertical displacements: hourglass effect (a) present and (b) controlled

Despite this numerical instability, several researchers have focused their efforts on overcoming this hourglass effect to use reduced numerical integration in different FEM applications. Due to the fact that the attractiveness of using a reduced number of integration points outweighs the drawbacks. Therefore, the evolution of this research topic has developed into many different applications. For example, several developments and formulations have been published over the past decades on the so called solid-shell elements, *i.e.*, an element which combines both solid and shell formulations for 3D analyses of thin structures. These publications include both reduced-integration developments (Bettaieb et al., 2015) along with enhanced assumed strains (EAS) or assumed natural strains (ANS) to overcome shear locking problems (Bassa et al., 2012).

Existing literature shows that the 4-node quadrilateral finite element is frequently used in non-linear analysis formulations and applications of computational mechanics. Consequentially, this element is often used as a starting point in the developments of many reduced numerical integration stabilization schemes before being extrapolated to other finite elements, such as hexahedrals for 3D analysis.

One of the most popular and efficient schemes for controlling the hourglass effect is the proposed by Flanagan and Belytschko (1981) and, also, improved by Belytschko et al. (1984), Belytschko and Bachrach (1986), and Belytschko and Bindeman (1991). This scheme is based on the addition of a four-point numerically integrated stabilizer stiffness matrix to the sub-integrated stiffness matrix. The construction of the stabilizer matrix implies that the considered constitutive model needs to be evaluated at all four integration points. The application of this method successfully recovers the rank of the stiffness matrix and controls the numerical instabilities at the cost of the required additional computations.

In this dissertation an improvement to this method is presented. The proposed improvement is based on the formulation and use of an analytical expression of the stabilizer stiffness matrix instead of the numerically integrated one. Since the evaluation of a constitutive model needs to be performed at each integration point, the use of this proposal enables a one-point evaluation rather than the originally required four-point evaluation. This feature is attractive because of the significant reduction computing-time assured due to the substantial decrease of the computations at each step of a non-linear analysis. Additionally, with this proposal the convergence needs to be achieved at only one integration point instead of four, which is compelling for the use of computationally demanding constitutive models.

All the application examples included in this work correspond to masonry structures. Masonry has been used as a structural material probably since a nomad decided to become sedentary and built a shelter by laying pieces of stone together, approximately 10,000 years ago. One of the most attractive characteristics of masonry construction is its simplicity, which is maybe the reason why masonry is the oldest material that still is widely used nowadays (Lourenço, 1996). In fact, currently, masonry is one of the most popular construction material, especially in low-rise buildings and in social interest housing.

Over time, masonry has evolved considerably in several aspects, including construction techniques, manufacturing processes of bricks and the diversity of materials employed in its composition. Additionally, due to a better understanding of the mechanical behaviour of masonry, several techniques of reinforcement that are aimed at improving its structural performance, have been proposed by researchers and widely applied by constructors.

Although the evolution of masonry is undeniable, many of the ancient masonry constructions were built with poor quality materials and deficient constructions techniques, *e.g.*, the use of low-strength mortar or even none of it. Furthermore, owing to the purely empirical knowledge about the structural conception of constructions, many of these structures are highly vulnerable to external events, such as earthquakes, that can induce lateral de-

mands to the structure.

This vulnerability is not only a problem for ancient masonry constructions. Modern structures, including tall buildings, are structurally conceived by ductile frames of concrete or steel with infill masonry walls. This structural conception is based in the hypothesis that the masonry walls do not contribute to the structural performance of such a structure. However, recent seismic events have shown that this hypothesis is not always valid and, occasionally, these walls represent an additional stiffness to the structure, which can be suddenly modified when they are damaged during the earthquake. Accordingly, these walls can not be ignored as a structural elements in the stages of analysis and design.

Despite the simplicity of masonry construction, the non-linear structural analysis of such constructions is not straightforward. In the past decades, several researchers around the world have focused in the development of numerical tools that are aimed at assesing the structural behaviour of masonry constructions. Even though their advances are remarkable, the proposals in this topic are computationally demanding. The difficultness of the problem lays on the mechanical characterization of the masonry as a highly non-linear heterogeneous material and, also, on the frequent irregular geometry of the constructions built with this material. The complex mechanical behaviour of masonry as a quasi-fragile material is characterized for its non-linearity, evident even at small demands, its low tension strength and the presence of the softening effect. Furthermore, due to the non-homogeneous nature of its components, masonry often has orthotropic behaviour.

The proposal of this thesis is applied to the study of masonry constructions through two different scopes. First, the plastic-damage model proposed by Oller et al. (1988) and Lubliner et al. (1989) was implemented to apply the proposed reduced integration scheme. This constitutive model is aimed to represent the complex non-linear behaviour of masonry with high precision.

In spite that these complex constitutive models have demonstrated to be able to simulate the real behaviour of materials; their application is not generally efficient for due to the following requirements: computer programs that include the implementations of the models to be used; that these programs include robust and efficient algorithms that allow approximating the solution of the non-linear mathematical problem; computers with enough processing capacity and specialized engineer for the pre- and post-processing stages of the analysis.

Therefore, it is convenient to have simplified and computationally efficient alternatives that achieves good-enough approximations according the problem to apply the proposal of this dissertation. One of these strategies, originally proposed by Rots (2001b), consists of the application of Sequentially Linear Analysis (SLA), which approximate the non-linear behaviour of a structure through a series of linear analyses in which the mechanical properties of the material of the more demanded elements are reduced, following a softening law. This strategy is computationally efficient since, as it consists of a series of linear analyses, it is not necessary an iterative process to reach the convergence of the solution in each analysis.

Due to the formulation of the SLA procedure, it is to be expected that the area under the stress-strain curve of the material is underestimated. Therefore, the formulation was improved by Rots and Invernizzi (2004), who proposed a mesh regularization procedure to minimize the influence of the mesh on the performance of the analysis. This procedure consists of the inclusion of a factor that modifies the tensile strength and the ultimate strain of the material.

In the original proposal of Rots (2001b), a linear softening law of the material is proposed, which is approximated with a saw.tooth diagram. Rots et al. (2008) proposed new softening models, including a non-linear one. Furthermore, DeJong et al. (2008), Eliáš et al. (2010) and Yu et al. (2018) proposed innovative algorithms that enable the consideration of non-proportional loads in the application of SLA. This extends the scope of application of the strategy to other loading patterns, *e.g.*, pre-compression and lateral loading stages.

Regarding the fields of application of the strategy, Rots (2001b) and Rots (2001a) applied it to the study of ancient masonry and reinforced concrete buildings. Later, Invernizzi et al. (2011) and Slobbe et al. (2012) applied it to the study of concrete structural elements with very brittle failure. Additionally, Pari et al. (2021) developed a robust model that allows the use of SLA for the study of masonry structures in 2 and 3 dimensions, showing that their proposal is able to reproduce the complex masonry mechanical behaviour.

There are even some algorithms to reduce the computational cost in the application of SLA such as those of Pari et al. (2020), who propose two solution strategies to reuse some decompositions of the stiffness matrix performed in previous linear analyses. In this way, advantage is taken of the fact that the changes in the system of equations of the finite element model are only local.

In this dissertation, the proposed stabilized reduced integration scheme is also applied through the SLA procedure as an alternative to its application by the plastic-damage constitutive model previously mentioned. The description of this application, its validation with examples taken from the specialized literature on the subject and application examples are included to show the efficiency achieved in comparison with other more robust non-linear analysis proposals.

1.2 Objectives

The main objective of this work is to propose and validate a computationally efficient strategy to perform non-linear analysis of masonry structures considering a homogenized constitutive model, based on the theories of plasticity and damage, implemented through a numerical integration scheme for the 4-node quadrilateral finite element that allows a one-point evaluation of it.

In order to achieve the main objective the following specific tasks were established:

- Formulate, numerically implement in the *FEAP* environment and validate, for both linear and non-linear analysis, a reduced numerical integration scheme for the 4-node quadrilateral finite element with an stabilization procedure that allows a one-point evaluation of a certain constitutive model.
- Study, numerically implement in the *FEAP* environment and validate a constitutive model based on the theories of plasticity and damage, optimal to simulate the mechanical behaviour of masonry.
- Study, numerically implement in the *FEAP* environment and validate an homogenization technique for organized masonry to be applied within the reduced numerical integration scheme and the plastic-damage constitutive model.
- Apply the complete strategy through the numerical approximation of the non-linear behaviour of experimental models which represent masonry structures.
- Study and numerically implement in a programming language a computational tool capable of performing a sequence of linear analysis with saw-tooth softening.
- Apply and validate through the reduced numerical integration scheme the implementation based on sequentially linear analysis with saw-tooth softening.

1.3 Outline of the thesis

In the following paragraphs, a general description of the content of each chapter is presented.

In the second chapter, a proposal for employing reduced numerical integration for the 4-node quadrilateral finite element is described. First, the problem of using reduced integration is widely discussed. Then, the formulation of the proposal is presented and mathematically validated. Additionally, several validation examples are presented which include comparisons with experimental results. The results are presented and discussed, emphasizing in the computational cost reduction.

Chapter 3 includes an overview of some aspects of the computational modelling of masonry structures. The plastic-damage model proposed by Oller et al. (1988) and Lubliner et al. (1989) is studied in this chapter. Furthermore, in this chapter, the numerical implementation of this model is widely discussed and validated through several debugging test. Finally, some aspects of the numerical implementation of the homogenization technique proposed by López et al. (1999) are also included and validated in this chapter.

The application of the complete strategy is included in chapter 4. For this purpose, two specimen of masonry walls, with and without opening, selected from a set of experiments, are analyzed through the complete strategy. The numerically obtained results are compared to the ones reported in the experiments. A thorough discussion of the results comparison is presented.

1. INTRODUCTION

In the fifth chapter an alternative for the application of the proposal of this thesis is described and validated. First, the procedure based on sequentially linear analysis with saw-tooth softening, proposed by Rots (2001b and 2004) is studied. Additionally, the application of the procedure using the reduced integration scheme is discussed, applied and validated through examples. The results are discussed.

Finally, in chapter 6, final remarks and conclusions are listed.

Reduced integration in the FEM

2.1 Introduction

In this chapter, a general discussion about the use of reduced numerical integration in the FEM formulation of solid elements is included. Initially, the advantages and drawbacks of using different quadrature orders in the numerical evaluation of the stiffness matrix of a 4-node quadrilateral finite element are discussed. Accordingly, a proposal for overcoming the numerical issues generated for using reduced integration, such as the rank deficiency of the stiffness matrix, is formulated and widely described.

Additionally, the numerical implementation in the *FEAP* (Taylor, 2017) program of the above mentioned proposal is described in this chapter. In order to validate both the formulation and the numerical implementation, several validation application examples are included all along this chapter. These examples include mathematical validation, linear and non-linear analysis with comparisons to canonical integration orders and experimental data available in the reviewed literature. A special discussion of the achieved computational cost reduction and the quality of the approximation is included.

2.2 Numerical integration in the FEM

In the isoparametric formulation of a quadrilateral finite element, numerical integration techniques are generally required to evaluate its stiffness matrix, \mathbf{K} (eq. 2.1), and, therefore, if a non-linear material behaviour is considered, for the constitutive model evaluation (Zienkiewicz and Taylor, 2013).

$$\mathbf{K} = t \int_A \underbrace{\mathbf{B}^T \mathbf{C} \mathbf{B}}_{\phi(x,y)} dA \approx t \sum_{i=1}^n \sum_{j=1}^n \phi(\xi_i, \eta_j) |\mathbf{J}| w_i w_j \quad (2.1)$$

Here, t is the element thickness, \mathbf{B} is the strain-displacement matrix and \mathbf{C} is the constitutive matrix for a plane-stress/strain, an EAS or an ANS behaviour. Also, x and y are the coordinates of the real physical space, ξ and η are the ones from the reference parent space

and $|\mathbf{J}|$ is the determinant of the Jacobian matrix. The terms ξ_i, η_j and w_i, w_j stand for the sampling points and weights, respectively, of the selected Gauss-Legendre quadrature order. As expected, the computational cost of this numerical procedure is proportional to the number of integration points used. Nevertheless, the use of a low-order quadrature can lead to numerical instabilities, such as that commonly referred as the hourglass effect. Therefore, the selection and implementation of an optimal integration scheme may represent a highly important task in the execution of finite element analysis, especially if a non-linear material behaviour is considered.

In 4-node quadrilateral finite elements, such as the one shown in fig. 2.1, two numerical integration schemes can be generally identified; the full integration scheme (FI), referred to the use of a 2×2 quadrature, and the reduced integration scheme (RI), referred to the use of 1×1 quadrature. To discuss the effects of the numerical integration scheme used in the stiffness matrix evaluation, the 4-node quadrilateral element of fig. 2.1 is studied with both FI and RI scheme herein.

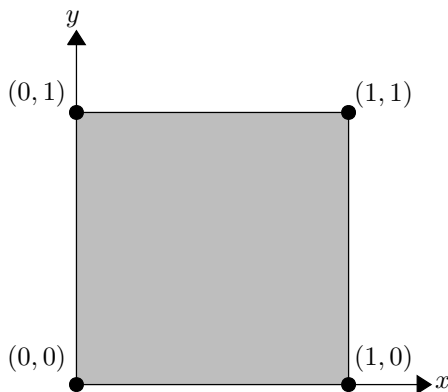


Figure 2.1. 4-node quadrilateral finite element

2.2.1 Full integration (FI)

In a canonical formulation of a 4-node quadrilateral, eq. 2.1 is evaluated with a FI scheme. Assuming an elasticity modulus of $E = 2000$ MPa, a Poisson's ratio of $\nu = 0.20$ the stiffness matrix is approximated through a 2×2 quadrature, $\mathbf{K}_{(4)}$ (eq. 2.2). Hereinafter, the subscript in parentheses indicates the number of integration points used to compute the corresponding matrix.

The deformation modes (eigenvectors) and its associated stiffness matrix (eigenvalues) obtained by the solution of the characteristic equation for the four-point stiffness matrix (eq. 2.3) are shown in figure 2.2. In this homogeneous linear equation, \mathbf{I}_8 is an eight-order identity matrix, λ is the eigenvalue and ϕ its corresponding eigenvector for which $\mathbf{K}_{(4)} \phi = \lambda \phi$.

$$\mathbf{K}_{(4)} = \begin{bmatrix} 972.2 & 312.5 & -555.6 & -104.2 & -486.1 & -312.5 & 69.4 & 104.2 \\ 312.5 & 972.2 & 104.2 & 69.4 & -312.5 & -486.1 & -104.2 & -555.6 \\ -555.6 & 104.2 & 972.2 & -312.5 & 69.4 & -104.2 & -486.1 & 312.5 \\ -104.2 & 69.4 & -312.5 & 972.2 & 104.2 & -555.6 & 312.5 & -486.1 \\ -486.1 & -312.5 & 69.4 & 104.2 & 972.2 & 312.5 & -555.6 & -104.2 \\ -312.5 & -486.1 & -104.2 & -555.6 & 312.5 & 972.2 & 104.2 & 69.4 \\ 69.4 & -104.2 & -486.1 & 312.5 & -555.6 & 104.2 & 972.2 & -312.5 \\ 104.2 & -555.6 & 312.5 & -486.1 & -104.2 & 69.4 & -312.5 & 972.2 \end{bmatrix} \quad (2.2)$$

$$(\mathbf{K}_{(4)} - \lambda \mathbf{I}_8) \phi = \mathbf{0} \quad (2.3)$$

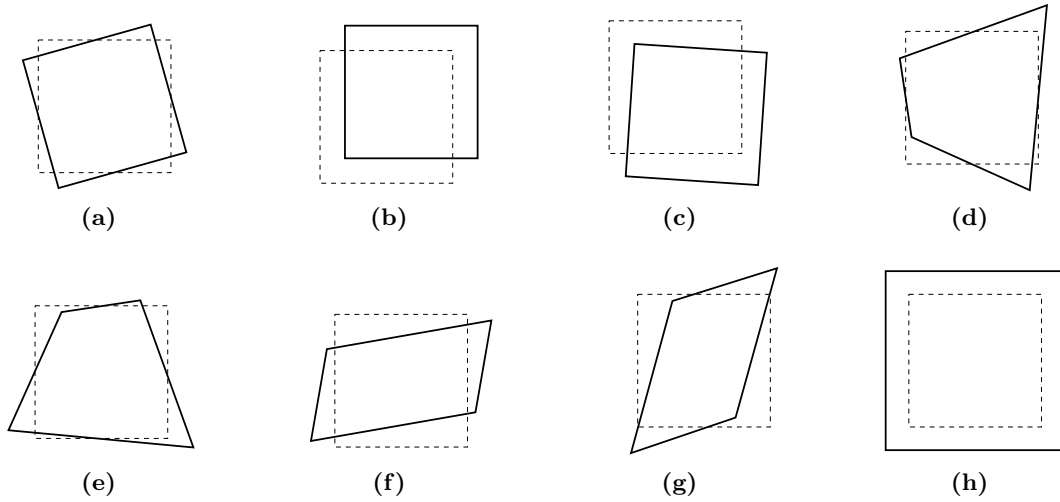


Figure 2.2. Stiffness matrix deformation modes obtained with FI

The first three are rigid-body modes (figs. 2.2a to 2.2c) for which the strain energy, U_e is zero. Modes from figs. 2.2d and 2.2e are the known as linear-strain or bending modes ($U_e > 0$). The last three are constant-strain modes (figs. 2.2f to 2.2h) with $U_e > 0$. There are 5 eigenvectors associated to a non-zero eigenvalue, thus, the rank of the stiffness matrix $\mathbf{K}_{(4)}$ is 5.

2.2.2 Reduced integration (RI)

Evaluating eq. 2.1 through RI considering the same parameters employed before with FI, a one-point stiffness matrix, $\mathbf{K}_{(1)}$, is obtained (eq. 2.4).

$$\mathbf{K}_{(1)} = \begin{bmatrix} 729.2 & 312.5 & -312.5 & -104.2 & -729.2 & -312.5 & 312.5 & 104.2 \\ 312.5 & 729.2 & 104.2 & 312.5 & -312.5 & -729.2 & -104.2 & -312.5 \\ -312.5 & 104.2 & 729.2 & -312.5 & 312.5 & -104.2 & -729.2 & 312.5 \\ -104.2 & 312.5 & -312.5 & 729.2 & 104.2 & -312.5 & 312.5 & -729.2 \\ -729.2 & -312.5 & 312.5 & 104.2 & 729.2 & 312.5 & -312.5 & -104.2 \\ -312.5 & -729.2 & -104.2 & -312.5 & 312.5 & 729.2 & 104.2 & 312.5 \\ 312.5 & -104.2 & -729.2 & 312.5 & -312.5 & 104.2 & 729.2 & -312.5 \\ 104.2 & -312.5 & 312.5 & -729.2 & -104.2 & 312.5 & -312.5 & 729.2 \end{bmatrix} \quad (2.4)$$

The characteristic equation, $(\mathbf{K}_{(1)} - \lambda \mathbf{I}_8)\boldsymbol{\phi} = \mathbf{0}$, is also solved in order to obtain the deformation modes of the $\mathbf{K}_{(1)}$ stiffness matrix. From fig. 2.3, it can be observed that the last three modes correspond to the so called constant-strain modes (figs. 2.3f to 2.3h), for which the corresponding strain energy, U_e , is greater than zero, regardless of the integration scheme employed in the numerical stiffness matrix evaluation. However, for the first five modes (figs. 2.3a to 2.3e) $U_e = 0$, but they are not rigid-body modes. These modes are called spurious or hourglass modes, due to because of their physical configuration when the assemblage of elements is performed (see fig. 1.2a). Therefore, the rank of the sub-integrated stiffness matrix is 3, in contrast to the fully integrated stiffness matrix which is 5.

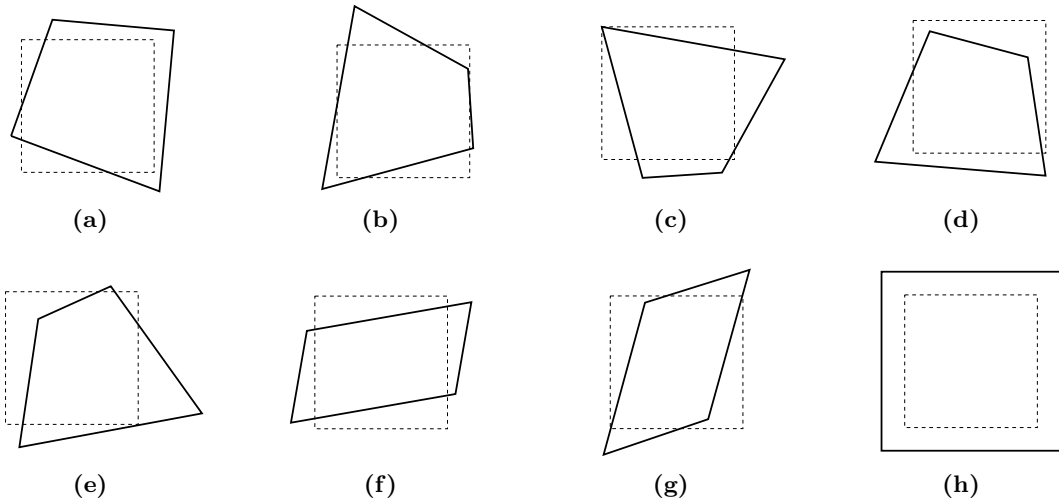


Figure 2.3. Stiffness matrix deformation modes obtained with RI

In table 2.1 a comparison of the deformation modes for a 4-node quadrilateral finite element, computed with both FI and RI, are included. In this table, it can be seen that the 5 spurious modes, that appeared when RI is used, replace the 3 constant deformation modes and 2 linear deformation modes that are generated when using IC. Therefore, to take advantage of the use of IR it is necessary to control this numerical inconsistency by a stabilization procedure.

In this dissertation, a stabilization procedure, mathematically based on the one-point stiffness matrix rank recovery, was studied, validated and applied. This stabilized reduced integration (SRI) scheme is described in the following sections.

Table 2.1. Comparison of a 4-node quadrilateral element deformation modes obtained with both FI and RI

Integration scheme	Integration points, i	Stiffness matrix rank, $R(\mathbf{K}_i)$	Deformation modes	Strain energy, U_e
FI	4	$R(\mathbf{K}_4) = 5$	3 constant-strain modes	$U_e > 0$
			2 linear-strain modes	$U_e > 0$
			3 rigid-body modes	$U_e = 0$
RI	1	$R(\mathbf{K}_1) = 3$	3 constant-strain modes	$U_e > 0$
			5 spurious modes	$U_e = 0$

2.3 Stabilization procedure

The method for controlling the hourglass effect developed by Belytschko et. al. (1986; 1991; 1984; 1981) is based on the addition of a stabilizer stiffness matrix, \mathbf{K}_{stab} , to the $\mathbf{K}_{(1)}$ stiffness matrix. This method was selected as a starting point of the proposal of this dissertation due to that the following advantages (Amezcuca, 2016):

- The possibility of using coarser meshes because of the improvement of the strain-energy representation of the linear-strain modes.
- The proved computational cost reduction in both linear and non-linear analysis.
- The successful control of the hourglass effect.
- The computational efficiency of the numerical implementation since no complex numerical procedures are required in the stabilizer stiffness matrix computation.

2.3.1 Formulation

From a mathematical point of view, the \mathbf{K}_{stab} matrix, for which $R(\mathbf{K}_{stab}) = 2$, controls the hourglass effect due to the rank recovery from 3 to 5 of $\mathbf{K}_{(1)}$ matrix, through the addition of the neglected terms when RI is used (eq. 2.5). An important remark is that this \mathbf{K}_{stab} addition only affects the hourglass modes, transforming them into rigid-body modes, with $U_e = 0$, and linear-strain modes, with $U_e > 0$ (see table 2.1).

$$\mathbf{K} = \mathbf{K}_{(1)} + \mathbf{K}_{stab} = \underbrace{t A \mathbf{B}_{(1)}^T \mathbf{C} \mathbf{B}_{(1)}}_{\mathbf{K}_{(1)}} + \mathbf{K}_{stab} \quad (2.5)$$

In this equation, A is the area of the quadrilateral element, $\mathbf{B}_{(1)}$ is the strain-displacement matrix evaluated in one integration point and, \mathbf{C} is the constitutive matrix. Consequentially, \mathbf{K}_{stab} is computed through the eq. 2.6 in which \mathbf{B}_{stab} stands for the stabilizer strain-displacement matrix (eq. 2.7).

$$\mathbf{K}_{stab} = t \int_A \mathbf{B}_{stab}^T \mathbf{C} \mathbf{B}_{stab} dA \quad (2.6)$$

$$\mathbf{B}_{stab} = \begin{bmatrix} h_{,x} \gamma_1 & 0 & h_{,x} \gamma_2 & 0 & h_{,x} \gamma_3 & 0 & h_{,x} \gamma_4 & 0 \\ 0 & h_{,y} \gamma_1 & 0 & h_{,y} \gamma_2 & 0 & h_{,y} \gamma_3 & 0 & h_{,y} \gamma_4 \\ h_{,x} \gamma_1 & h_{,x} \gamma_1 & h_{,x} \gamma_2 & h_{,x} \gamma_2 & h_{,x} \gamma_3 & h_{,x} \gamma_3 & h_{,x} \gamma_4 & h_{,x} \gamma_4 \end{bmatrix} \quad (2.7)$$

In eq. 2.7, h is the product of the natural coordinates, $h = \xi \eta$ and a comma preceding a lower-case subscript denotes partial differentiation with respect to the global coordinate system, x and y . Also, $\gamma_1, \gamma_2, \gamma_3$ and γ_4 are the components of the hourglass shape vector, γ , defined in the work of Flanagan and Belytschko (1981). By algebraic procedures applied to the integral of eq. 2.6 and the definition of eq. 2.7, an expression for the computation of the \mathbf{K}_{stab} is obtained (eq. 2.8).

$$\mathbf{K}_{stab} = t \begin{bmatrix} k_1 \gamma \gamma^T & k_3 \gamma \gamma^T \\ k_3 \gamma \gamma^T & k_2 \gamma \gamma^T \end{bmatrix} \quad (2.8)$$

where:

$$k_1 = C_{11} H_{xx} + C_{33} H_{yy} \quad (2.9a)$$

$$k_2 = C_{11} H_{yy} + C_{33} H_{xx} \quad (2.9b)$$

$$k_3 = (C_{12} + C_{33}) H_{xy} \quad (2.9c)$$

Here, the C_{ij} terms are elements of the plane-stress or plane-strain constitutive matrix, \mathbf{C} , or for a certain assumed material strain behaviour according to Belytschko and Bindeman (1991). In the original procedure, \mathbf{K}_{stab} is computed by means of numerical integration, since the H_{xx}, H_{yy} and H_{xy} terms in eq. 2.8 are obtained by the eq. 2.10 (Belytschko and Bachrach, 1986). Therefore, when a non-linear analysis is performed, the iterations for the approximation of stresses are evaluated at the considered integration points, *e.g.*, four integration points if a FI scheme is used. In the above-mentioned papers, it is demonstrated that this method successfully controls the hourglass effect and also allows the possibility, in some cases, of using coarser meshes (see Amezcua, 2016).

$$H_{xx} = \int_A h_{,x}^2 dA \quad (2.10a)$$

$$H_{yy} = \int_A h_{,y}^2 dA \quad (2.10b)$$

$$H_{xy} = \int_A h_{,x} h_{,y} dA \quad (2.10c)$$

Therefore, when \mathbf{K}_{stab} is computed through numerical integration, it is necessary to use a 2×2 Gauss-Legendre quadrature in order to numerically evaluate the terms H_{xx}, H_{yy} and H_{xy} of eqs. 2.10, otherwise, if RI is used, these become null terms. This implies that the stiffness matrix and, consequently, the strains and stresses are approximated at all

four integration points corresponding to a 2×2 quadrature. However, in this work, an analytical integration of the expressions of eq. 2.10 is performed, in order to obtain an analytical expression for \mathbf{K}_{stab} . Thus, the stabilized stiffness matrix and, consequently, the strains and stresses are approximated in only integration point corresponding to a 1×1 quadrature. Changing the integration domain of the expressions in eqs. 2.10 to that of the natural coordinate system, the following equations were obtained:

$$H_{xx} = \int_{-1}^{+1} \int_{-1}^{+1} h_{,x}^2 |\mathbf{J}| d\xi d\eta \quad (2.11a)$$

$$H_{yy} = \int_{-1}^{+1} \int_{-1}^{+1} h_{,y}^2 |\mathbf{J}| d\xi d\eta \quad (2.11b)$$

$$H_{xy} = \int_{-1}^{+1} \int_{-1}^{+1} h_{,x} h_{,y} |\mathbf{J}| d\xi d\eta \quad (2.11c)$$

Through algebraic procedures, it may be demonstrated that $h_{,x}$ and $h_{,y}$ can be computed using the following equations:

$$h_{,x} = -\frac{4}{\beta} (\mathbf{y} \boldsymbol{\alpha}_1 \xi - \mathbf{y} \boldsymbol{\alpha}_3 \eta) \quad (2.12a)$$

$$h_{,y} = \frac{4}{\beta} (\mathbf{x} \boldsymbol{\alpha}_1 \xi - \mathbf{x} \boldsymbol{\alpha}_3 \eta) \quad (2.12b)$$

where:

$$\boldsymbol{\alpha}_1^T = [-1 \quad 1 \quad 1 \quad -1] \quad (2.13a)$$

$$\boldsymbol{\alpha}_2^T = [1 \quad -1 \quad 1 \quad -1] \quad (2.13b)$$

$$\boldsymbol{\alpha}_3^T = [-1 \quad -1 \quad 1 \quad 1] \quad (2.13c)$$

Also, in eq. 2.12, β is a function of the natural coordinates and three constant terms (δ_1 , δ_2 and δ_3) that are dependent of the element geometry in global coordinates through $\mathbf{x} = [x_1 \quad x_2 \quad x_3 \quad x_4]$ and $\mathbf{y} = [y_1 \quad y_2 \quad y_3 \quad y_4]$ vectors, (eqs. 2.14 and 2.15). It can be inferred that the \mathbf{x} and \mathbf{y} vectors define the order of the expressions to be analytically integrated, and therefore, the complexity of this task.

$$\beta = \delta_1 + \delta_2 \xi + \delta_3 \eta \quad (2.14)$$

$$\delta_1 = (\mathbf{x} \boldsymbol{\alpha}_1) (\mathbf{y} \boldsymbol{\alpha}_3) - (\mathbf{x} \boldsymbol{\alpha}_3) (\mathbf{y} \boldsymbol{\alpha}_1) \quad (2.15a)$$

$$\delta_2 = (\mathbf{x} \boldsymbol{\alpha}_1) (\mathbf{y} \boldsymbol{\alpha}_2) - (\mathbf{x} \boldsymbol{\alpha}_2) (\mathbf{y} \boldsymbol{\alpha}_1) \quad (2.15b)$$

$$\delta_3 = (\mathbf{x} \boldsymbol{\alpha}_2) (\mathbf{y} \boldsymbol{\alpha}_3) - (\mathbf{x} \boldsymbol{\alpha}_3) (\mathbf{y} \boldsymbol{\alpha}_2) \quad (2.15c)$$

2.3.2 Mathematical validation

The formulation presented in section 2.3.1 was applied to the same 4-node quadrilateral element, studied with FI and RI, and a stabilized stiffness matrix is computed (eq. 2.16). Additionally, the deformation modes were obtained (fig. 2.4). From this figure, it can be stated that the first three modes, such as those obtained when FI is used, correspond to rigid body motions (figs. 2.4a to 2.4c), for which the corresponding strain energy is zero, $U_e = 0$. The subsequent two are linear-strain or bending modes (figs 2.4d and 2.4e), with $U_e > 0$. Finally, the last three modes are those of constant strain (figs. 2.4f to 2.4h), in which $U_e > 0$. As this stiffness matrix, computed by SRI, is composed of five modes with nonzero strain energy, *i.e.* linearly independents, the matrix rank is 5, as well as when the stiffness matrix is obtained by means of FI.

$$\mathbf{K} = \begin{bmatrix} 972.2 & 312.5 & -555.6 & -104.2 & -486.1 & -312.5 & 69.4 & 104.2 \\ 312.5 & 972.2 & 104.2 & 69.4 & -312.5 & -486.1 & -104.2 & -555.6 \\ -555.6 & 104.2 & 972.2 & -312.5 & 69.4 & -104.2 & -486.1 & 312.5 \\ -104.2 & 69.4 & -312.5 & 972.2 & 104.2 & -555.6 & 312.5 & -486.1 \\ -486.1 & -312.5 & 69.4 & 104.2 & 972.2 & 312.5 & -555.6 & -104.2 \\ -312.5 & -486.1 & -104.2 & -555.6 & 312.5 & 972.2 & 104.2 & 69.4 \\ 69.4 & -104.2 & -486.1 & 312.5 & -555.6 & 104.2 & 972.2 & -312.5 \\ 104.2 & -555.6 & 312.5 & -486.1 & -104.2 & 69.4 & -312.5 & 972.2 \end{bmatrix} \quad (2.16)$$

Accordingly, this SRI scheme correctly augments the rank of the one-point stiffness matrix by the addition of an analytical expression of the \mathbf{K}_{stab} matrix.

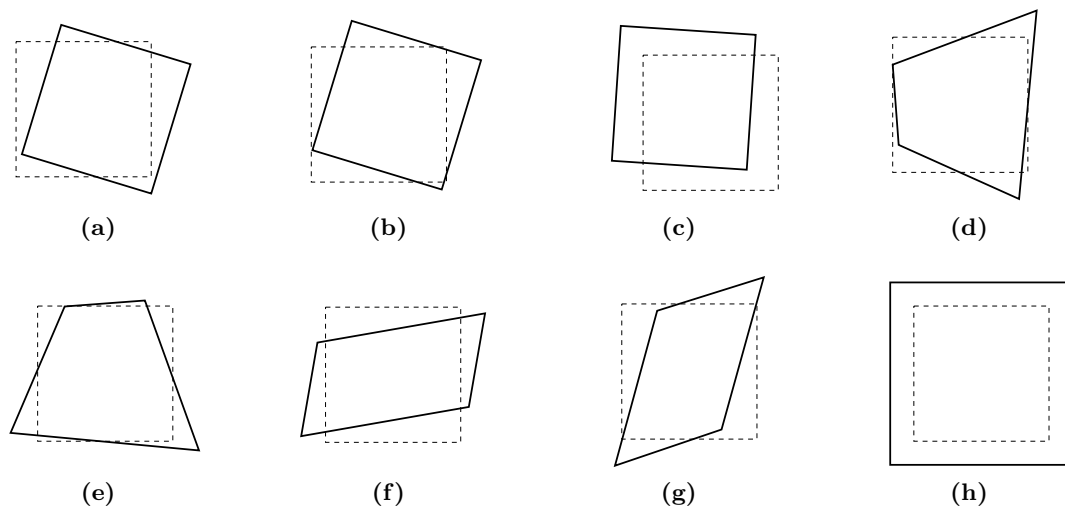


Figure 2.4. Stiffness matrix deformation modes obtained with SRI

2.3.3 Numerical implementation

To apply this SRI formulation to models representing structural engineering problems, it is necessary to perform a numerical implementation in a computer environment. For this purpose, the non-linear finite element program *FEAP* (Taylor, 2017) was selected. This user routine implemented follows the algorithm of the flowchart in fig. 2.5. It should be noted that the main differences, compared to the original method, are the following:

- In this routine, no numerical integration procedure are required to calculate the stabilizer stiffness matrix, \mathbf{K}_{stab} . Instead, the analytically integrated expression of \mathbf{K}_{stab} is numerically evaluated. Therefore, the stabilized stiffness matrix is composed of the contribution of one integration point and the contribution of the analytical integration.
- After computing the displacements, \mathbf{d} , the deformations are calculated with the eq. 2.17.

$$\boldsymbol{\varepsilon}_{(1)} = \mathbf{B} \mathbf{d} \quad (2.17)$$

- For a linear problem, the stresses are calculated directly with the eq. 2.18.

$$\boldsymbol{\sigma}_{(1)} = \mathbf{C} \boldsymbol{\varepsilon}_{(1)} \quad (2.18)$$

- For non-linear problems, three different constitutive model are considered for both validation and application purposes.

2.4 Validation examples

To validate the use of the SRI scheme, linear, eigen and non-linear analysis were performed in order to validate and to discuss the performance of the SRI scheme. Also, a comparison with experimental data is included in this section.

2.4.1 Linear analysis

First, the Cook's Membrane problem was selected (Cook, 1974). This problem is widely used by several authors to validate their developments due to the fact that its analytical solution for a linear analysis is known. For example, in the work of Fredriksson and Ottosen (2004) this problem was used as a numerical example to show the efficiency of a reduced integration technique for the 4-node quadrilateral element and, in the work of Flores (2016), was used to apply a proposal for the hexahedral solid-shell elements. In fig. 2.6, the geometric characteristics and the boundary conditions of such membrane are shown.

For analyzing the membrane, a Young's modulus $E = 1000$ MPa, Poisson's ratio $\nu = 0.33$ and an applied load $P = 1000$ N at the free end were considered. This P load has a

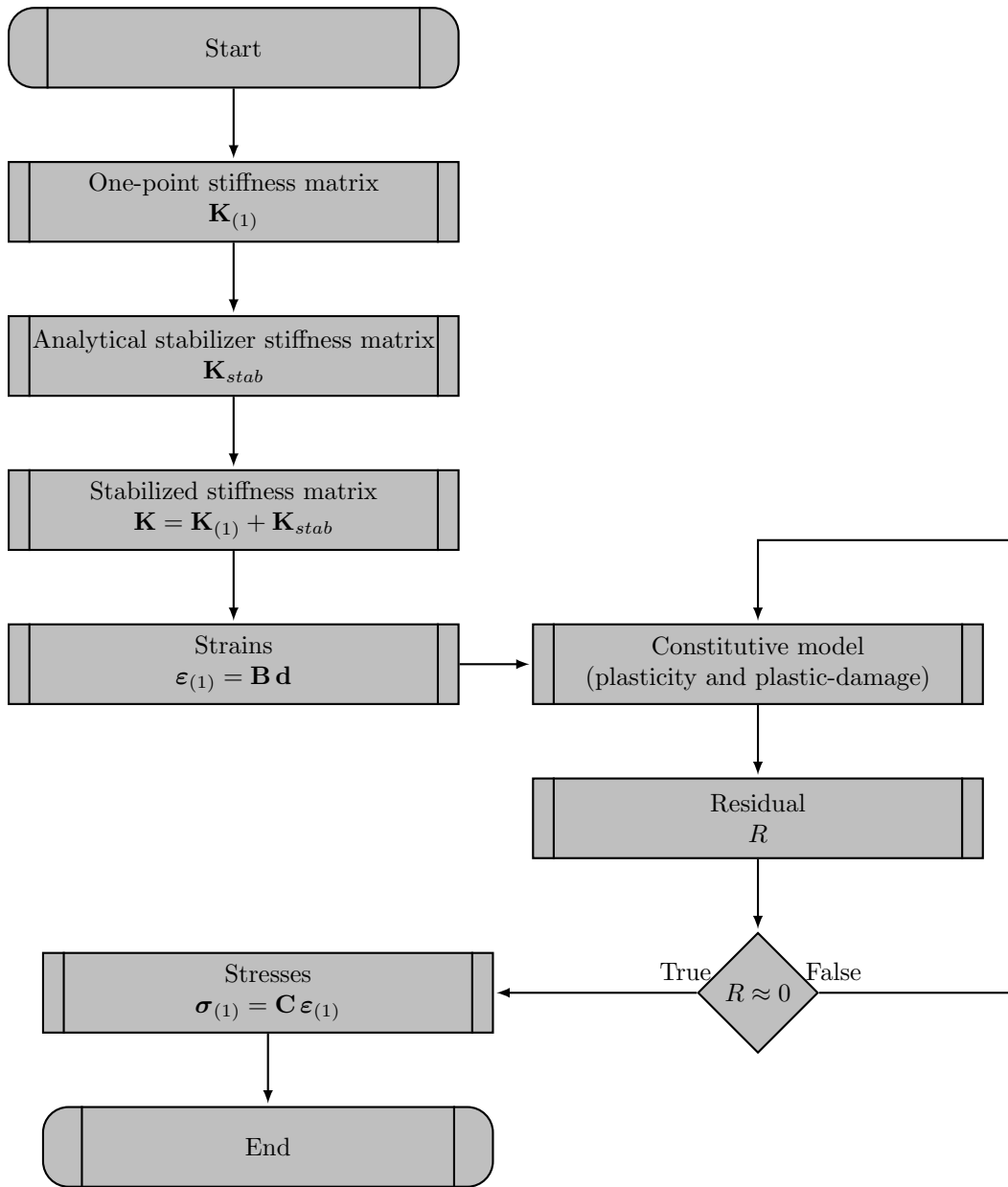


Figure 2.5. User routine flowchart implemented in *FEAP* (Taylor, 2017)

parabolic distribution, as shown in fig. 2.6. Five meshes were built, with 2, 4, 8, 16 and 32 4-node quadrilateral elements at the end where the load is applied. A plane-stress problem was analyzed with FI, RI and with the SRI schemes.

Convergence analysis to the analytical solution of the strain energy, for each mesh mentioned above, is included in figure 2.7. From this figure, it can be observed a change in the convergence direction when using RI. Hence, it can be concluded that while in FI the larger the number of elements, the more flexible is the membrane, in RI the opposite

occurs. According to Cook et al. (1989), the use of reduced numerical integration tends to soften the elements because the higher-order polynomial terms do not contribute to the strain energy, *i.e.*, some of the more complicated modes offer less resistance to deformation. Also, when applying the SRI scheme, the convergence direction is the same as in FI. An acceptable solution is reached with SRI in comparison with FI. Additionally, it is important to keep in mind that the SRI scheme is faster in computing-time terms for a mesh-to-mesh comparison. Although the computing time reduction in this example is not significantly attractive, it may be more attractive for non-linear cases, especially when the problem involves large computational processes.

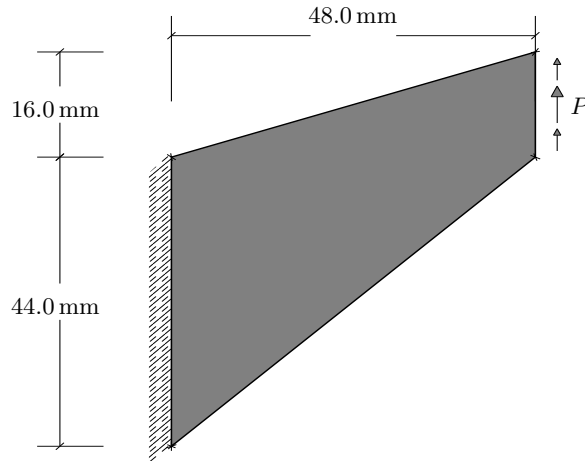


Figure 2.6. Cook's membrane geometry and boundary conditions

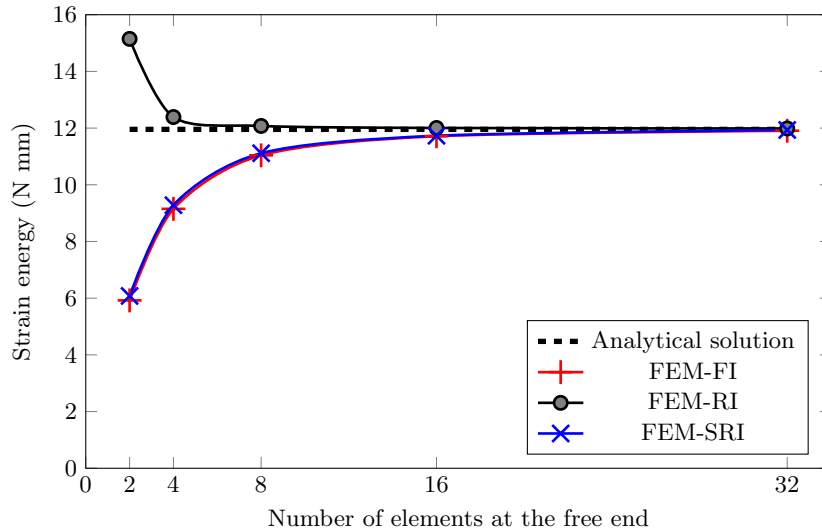


Figure 2.7. Cook's membrane convergence to analytical solution in strain energy

2.4.2 Algebraic eigen-value problem

Furthermore, an eigen-analysis of this membrane was carried out, the same mechanical properties used in the linear analysis were considered. The characteristic equation of the global stiffness matrix, $(\mathbf{K}_G - \lambda\mathbf{I})\phi = \mathbf{0}$, was solved, employing FI, RI and SRI, in order to compare the obtained deformation modes. The first and second deformation modes of the 16-element mesh of the membrane are plotted in figs. 2.8 and 2.9, respectively.

For comparing these graphs, the same factor scale was used. Similarly to the original stabilization scheme, the former figures show a notable resemblance in the deformed configuration and an evident hourglass effect control, which is more noticeable at the free end of the membrane and at the vertical lines of the mesh.

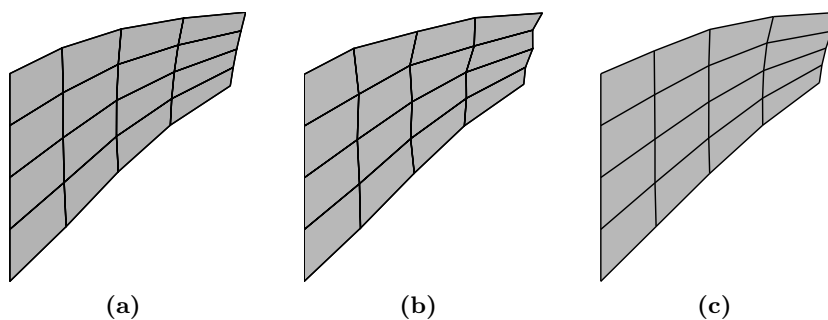


Figure 2.8. Cook's membrane first deformation mode obtained with (a) FI, (b) RI and (c) SRI

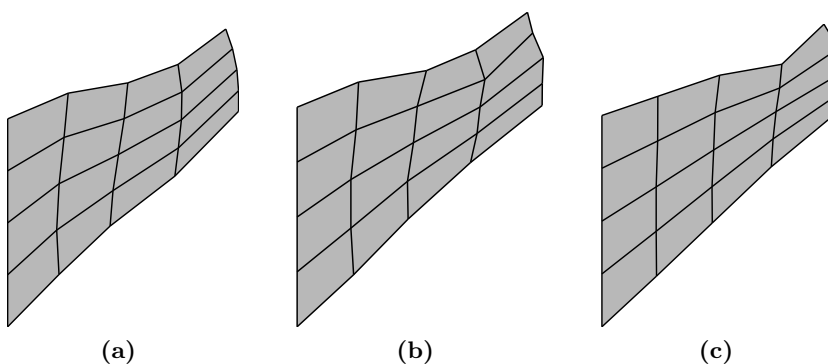


Figure 2.9. Cook's membrane second deformation mode obtained with (a) FI, (b) RI and (c) SRI

2.4.3 Non-linear analysis

As previously mentioned, this SRI scheme is aimed to be applied in non-linear problems in which the required computational cost is substantially high in comparison to a linear

problem. Accordingly, it is essential to validate the proposal through its application in non-linear analysis.

Four validation examples are included in this section. The examples were analyzed employing plasticity constitutive models with the Von Mises and Drucker and Prager yield criteria. These constitutive models are used only for comparing the results obtained through both FI and SRI numerical integration schemes.

2.4.3.1 Cook's membrane

As well as in the last two analysis (linear an eigen-analysis), Cook's membrane was used to validate the performance of the SRI scheme for non-linear analysis. Displacements were imposed at the free end to reduce convergence problems. Two meshes, *A* and *B*, composed of 64 and 1024 4-node quadrilateral elements, respectively, were built to show the advantages of the SRI scheme.

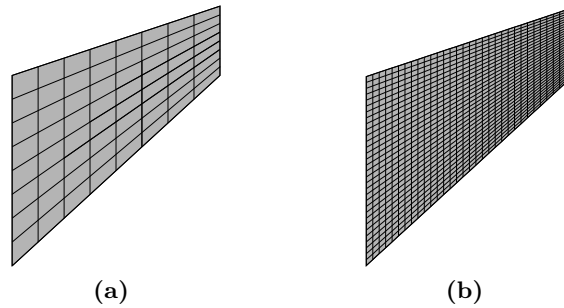


Figure 2.10. Cook's membrane: (a) mesh *A* and (b) mesh *B*

When analyzing the plane-stress problem, the mechanical properties of table 2.2 were considered. The non-linear material behaviour was simulated employing the algorithm proposed by Simo and Taylor (1986). In this elastoplastic constitutive model for plane stress, a non-linear isotropic hardening and the Von Mises yield criterion are considered. The non-linear mathematical problem was approximated through the application of the modified Newton-Raphson method, imposing a 10 mm displacement at all the free-end nodes. Both meshes, *A* and *B*, were analyzed with the previously described FI and SRI scheme. Von Mises stress distributions at the end of the analysis for both schemes and meshes are displayed in fig. 2.11. Here, it can be noted that the stress distribution is similar in both integration schemes, especially in the zones where the considered yield stress was reached.

Table 2.2. Mechanical parameters considered in the analysis of the Cook's membrane

Elasticity modulus	Poisson's ratio	Yield strength
$E = 2000 \text{ MPa}$	$\nu = 0.20$	$Y_0 = 0.50 \text{ MPa}$

In fig. 2.12 it is included the resulting reaction-displacement diagrams and are highlighted some intermediate states of the analysis for which its Von Mises stress distributions can

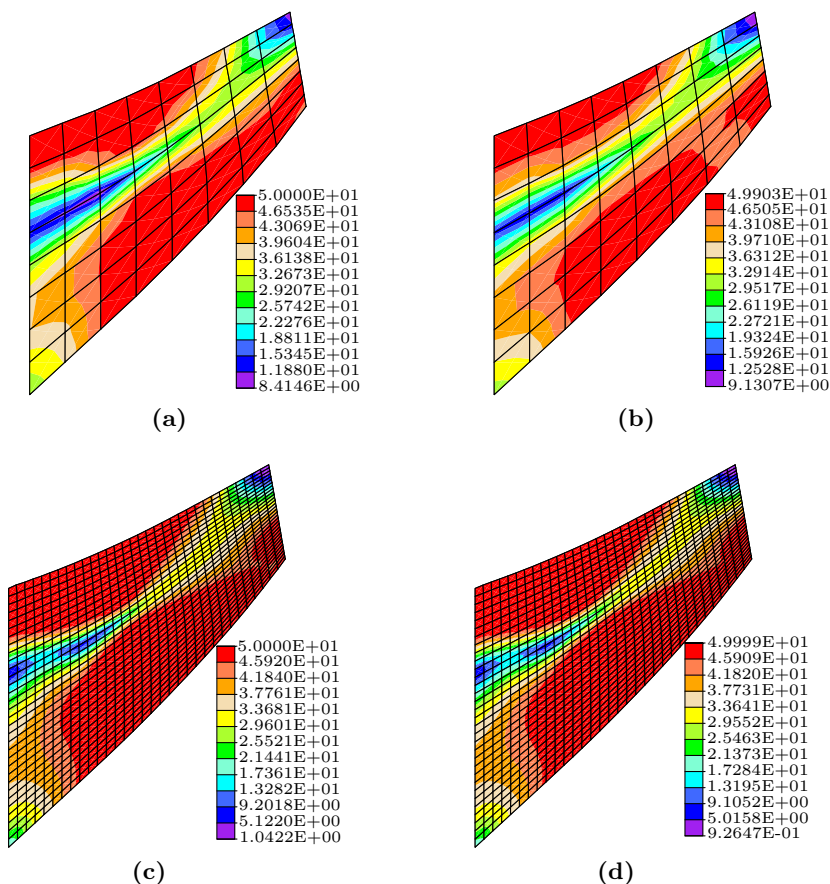


Figure 2.11. Von Mises stress distribution at the end of the analysis for mesh *A* with (a) SRI and (b) FI; and for the mesh *B* with (c) SRI and (d) FI

be seen in fig. 2.13. Based on this figures certain remarks can be addressed. First, the results from the SRI scheme are similar to those from FI. Nevertheless, the computing time employed with SRI decreased considerably, due to the evaluation at a unique integration point. Second, when comparing a specific mesh, the greater the number of elements, the better the concordance of results from both schemes. Third, the approximated behaviour of the mesh *A* through SRI are closer than those obtained by FI for the mesh *B*. Fourth, the approximation reached with SRI for mesh *A* represents an 86.03 % decrease of the computational cost with respect to that of the FI scheme applied to mesh *B*, *i.e.*, approximately 7.16 times faster (fig. 2.14).

The latter observation is the most attractive advantage of the implementation of SRI approach to non-linear problems. As the computational cost required for analyzing this type of problems is proportional to the number of elements, and the number of integration points thereof, within the mesh, the analysis is faster. The main impact of the reduction of the computational cost is the possibility of using sophisticated constitutive models, such as those involving plastic-damage (Oller et al., 1988), which are of great interest for practical engineering applications and not just for research purposes. Even though, the

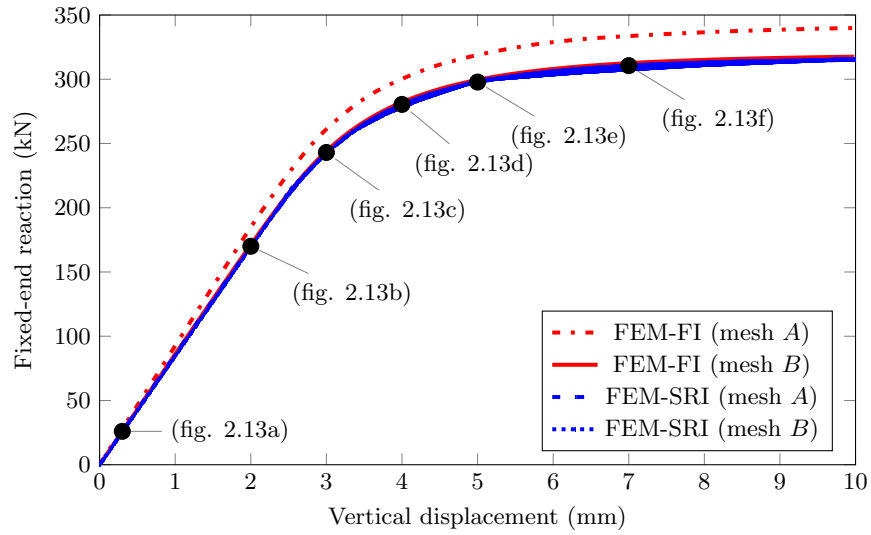


Figure 2.12. Reaction-displacement diagram of the Cook's Membrane

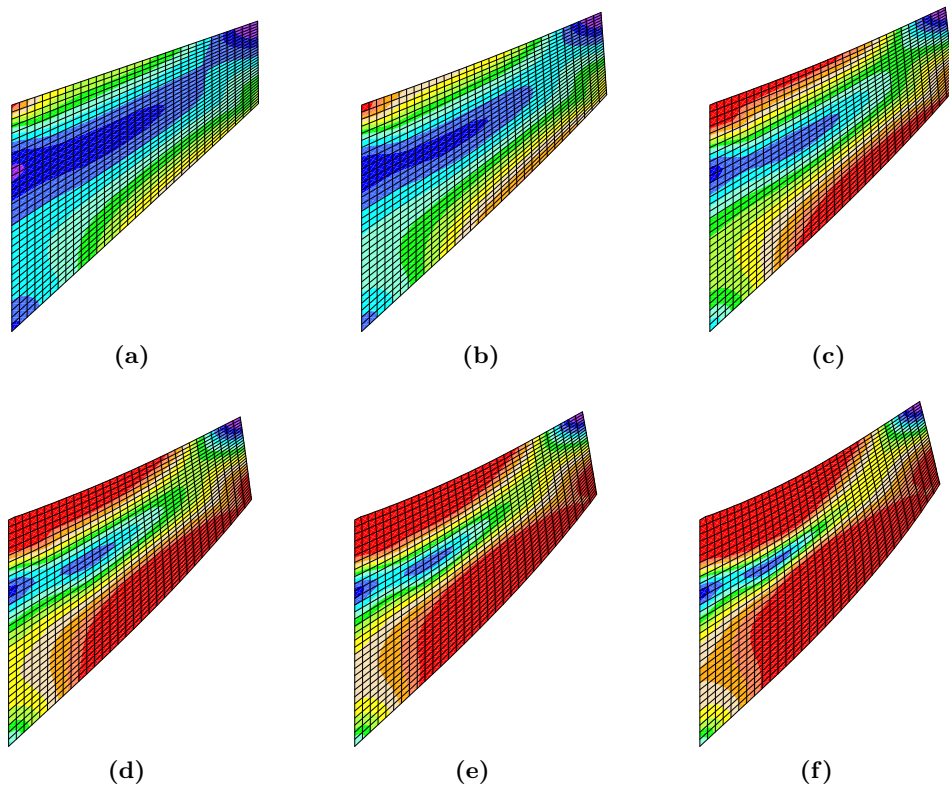


Figure 2.13. Six intermediate analysis states of Von Mises stress distribution for mesh *B* with SRI at displacement of (a) 0.3 mm, (b) 2 mm, (c) 3 mm, (d) 4 mm, (e) 5 mm and (f) 7 mm

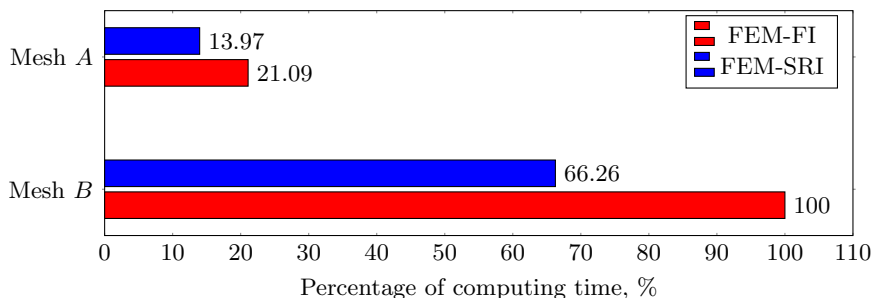


Figure 2.14. Computing time comparison for the non-linear analysis of the Cook’s membrane

real solution of a non-linear problem may be generally unknown, such as that from fig. 2.12, a finite element approximation of it closely approaches to what may be considered as a real solution when sufficiently fine meshes are used. Hence, a comparison between both numerical integration schemes should be sufficient for validating the approximation proposed.

2.4.3.2 Shear wall with openings

This masonry wall was tested by Bono et al. (1998) and studied with Rigid Block Models by Orduña (2003). The wall is 5800 mm long and 3600 mm high. It has two door openings of $1000 \times 2200 \text{ mm}^2$. For the masonry, the mechanical properties of table 2.3 were assumed. These mechanical properties were proposed according to the Complementary Technical Standards of the Mexico City Building Regulations (GDF, 2004). A constitutive model based on the Von Mises yield criterion was used (Simo and Taylor, 1986). Two meshes, named *A* and *B*, were built with 1,284 and 5,140 4-node quadrilateral finite elements, respectively (fig. 2.15). A 50 mm displacement was imposed on all nodes at the top of the wall.

The reaction-displacement diagrams for each mesh analyzed with FI and SRI are included in fig. 2.16 and, in the figs. 2.17a to 2.17f, the evolution of the Von Mises Stress distribution is showed. In this example, observations analogous to those pointed out in the Cook’s membrane validation example with non-linear behaviour can be stated. In this case, the maximum difference between the approximated results using SRI (mesh *A*) and FI (mesh *B*) is 1.05% and the computing time reduction is 86.44%, which is 7.4 times faster (fig. 2.18).

Table 2.3. Mechanical parameters considered in the analysis of the shear wall

Elasticity modulus	Poisson’s ratio	Yield strength
$E = 1750 \text{ MPa}$	$\nu = 0.20$	$Y_0 = 3.50 \text{ MPa}$

In the fig. 2.19 the approximated distribution of the Von Mises stresses by FI and SRI with the meshes *A* and *B* are compared. A clear similarity can be seen in all of them. However, as mentioned above, the computational cost using SRI is significantly lower than

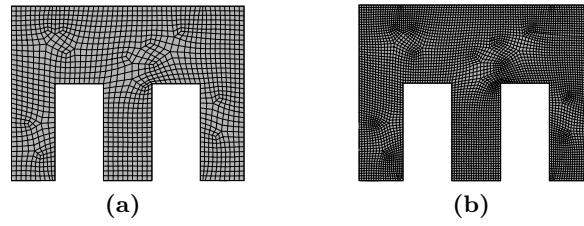


Figure 2.15. Shear wall with openings: (a) mesh *A* and (b) mesh *B*

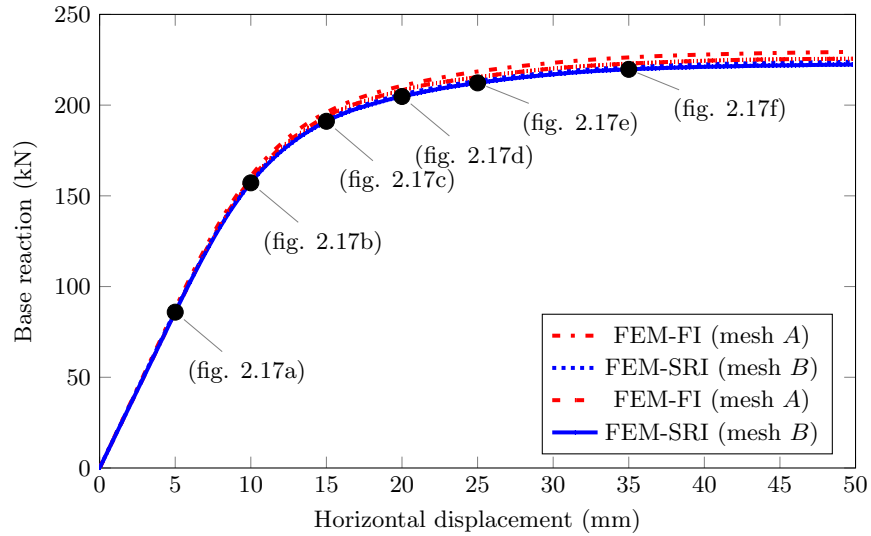


Figure 2.16. Reaction-displacement diagram of the shear wall with openings

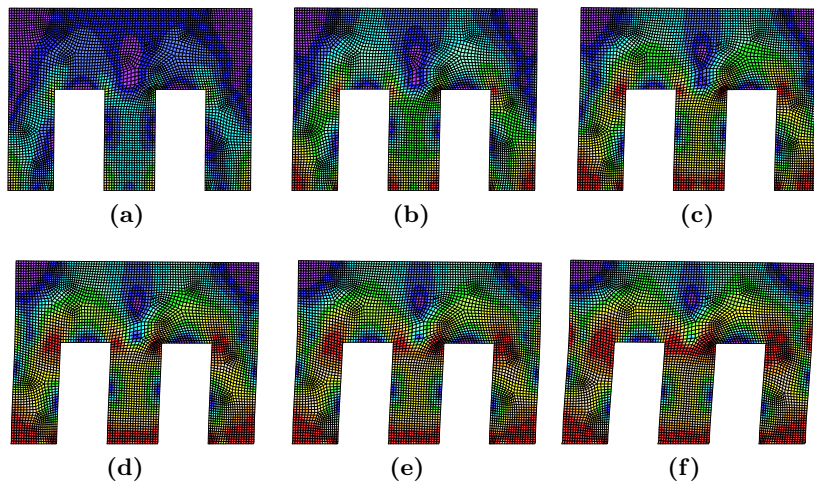


Figure 2.17. Six intermediate analysis states of Von Mises stress distribution for mesh *B* with SRI at displacement of (a) 5 mm, (b) 10 mm, (c) 15 mm, (d) 20 mm, (e) 25 mm and (f) 35 mm

2. REDUCED INTEGRATION IN THE FEM

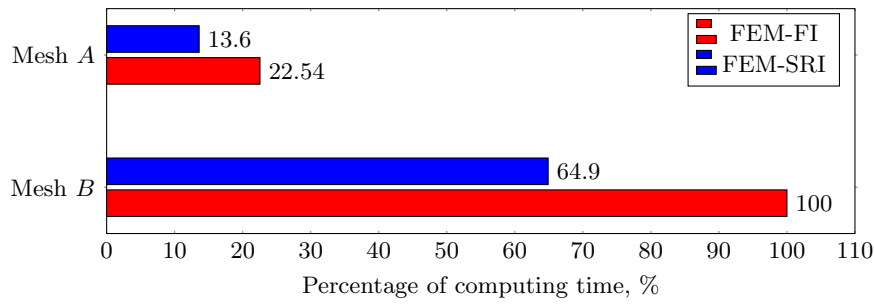


Figure 2.18. Computing time comparison for the non-linear analysis of the shear wall with openings

that of FI. It is known that the Von Mises yield criterion is not suitable for modelling the mechanical behaviour of materials such as masonry since these materials have different compressive and tensile strengths. Nevertheless, the objective of this example is to compare the computing time of FI and SRI integration schemes and not to compare with experimental tests. In the section 2.4.4 and in chapter 4 a comparison with experimental results is performed and widely discussed.

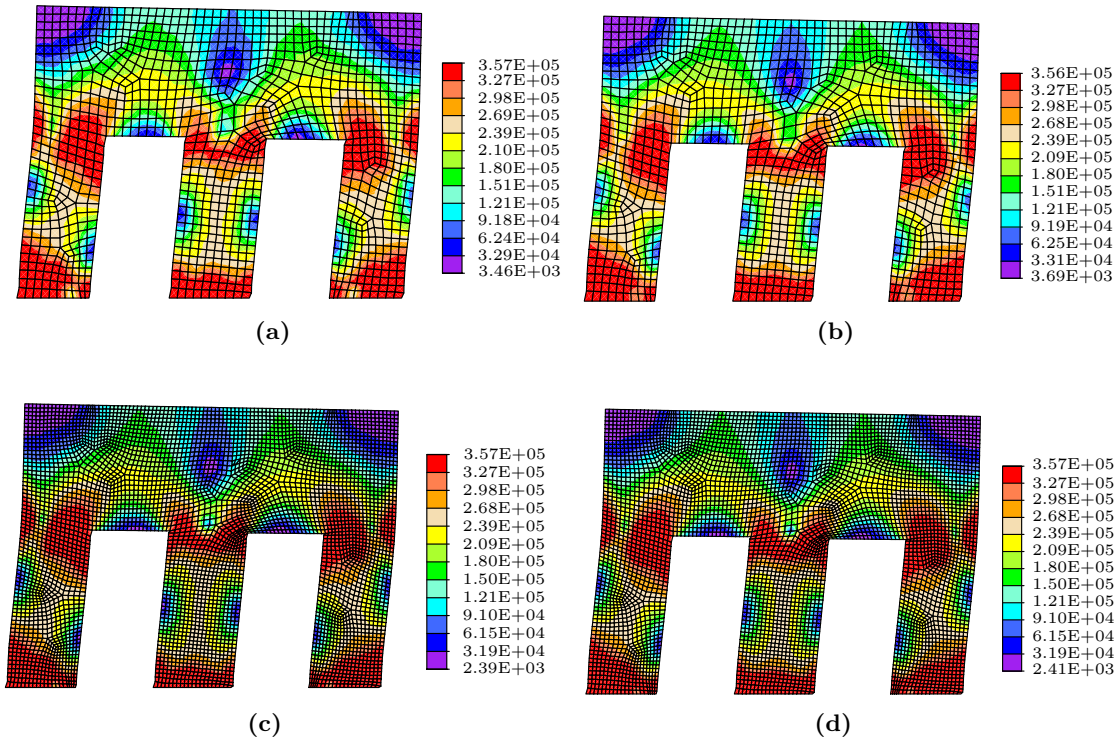


Figure 2.19. Von Mises stress distribution for mesh A with (a) SRI and (b) FI; and for the mesh B with (c) SRI and (d) FI

2.4.3.3 Monastery of São Vicente de Fora

This monastery, founded in 1147 by D. Alfonso Henriques, was built on one of the east hills of the city of Lisbon, in Portugal. The Lisbon earthquake of 1755 caused serious damage to the church and the monastery (Correia et al., 2007). Because of the history behind this building and its architectural beauty, there is a high interest in guaranteeing its structural safety, especially when subjected to future seismic events.

The monastery is mainly structured by columns and arches of stone blocks joined with mortar. In the European Laboratory for Structural Assessment (ELSA), located at Ispra, Italy, many experiments were performed on a full-scale model of a monastery section that includes three columns, two arches and two semi-arches (Pegon et al., 2001). A photograph of the experimental model is included in fig. 2.20.

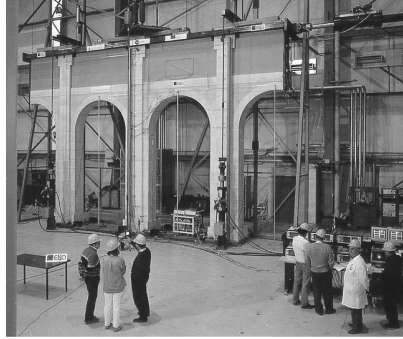


Figure 2.20. Full-scale model at the ELSA Laboratory (Pegon et al., 2001)

Several researchers have used the results of these experiments in order to validate or to apply numerical models, that were proposed for simulating the masonry behaviour as a structural material, for example Orduña et al. (2007) and Giordano et al. (2002). In this work, these results were also used, comparing them to those obtained using the SRI scheme in the next section. In this section, only comparisons between FI and SRI schemes are discussed. The geometry used for the finite element mesh was consistent with the full-scale model (fig. 2.20). The model was 7450 mm high and 10800 mm long. The three columns were spaced 3600 mm to each other with a rectangular section 800 mm wide and 910 mm deep. The arches were 1250 mm high.

Two meshes were built, while the mesh *A* is made up of 1,323 elements, the mesh *B* has 5,352 elements (fig. 2.21). The constitutive model based on the Von Mises yield criterion proposed by Simo and Taylor (1986) was used. The mechanical parameters for the material are summarized in table 2.4.

Table 2.4. Mechanical parameters considered in the analysis of the arcade

Elasticity modulus	Poisson's ratio	Yield strength
$E = 1000 \text{ MPa}$	$\nu = 0.20$	$Y_0 = 0.10 \text{ MPa}$

Displacements of 50 mm were imposed on all the top nodes of the arcade. The reaction-displacement diagrams are shown in fig. 2.22 for both meshes analyzed with both FI and

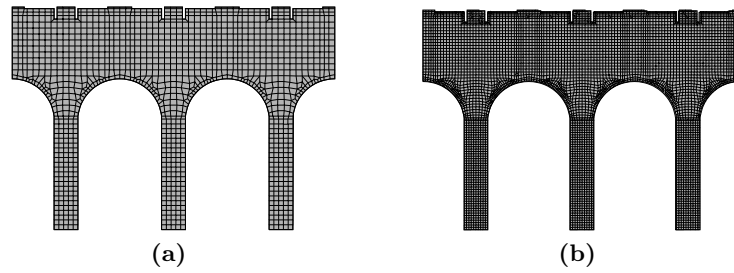


Figure 2.21. Arcade of the Monastery of São Vicente de Fora: (a) mesh A and (b) mesh B

SRI. In this example, observations can be made analogous to those pointed out in the previous examples (Cook’s membrane and shear wall with openings). In this case, the maximum difference between the approximated results by SRI (mesh A) and by FI (mesh B) is 1.42% and the reduction in computing time is 85.90% which is 7.1 times faster (2.23).

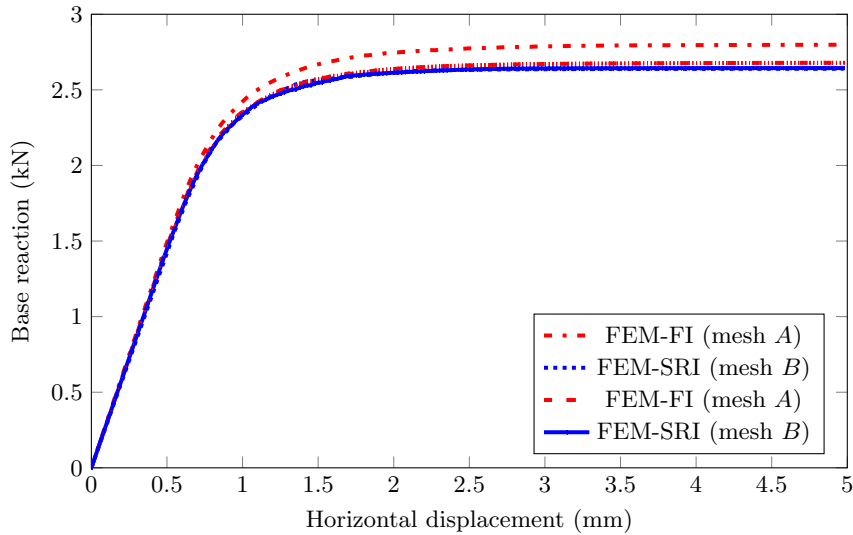


Figure 2.22. Reaction-displacement diagram of the arcade

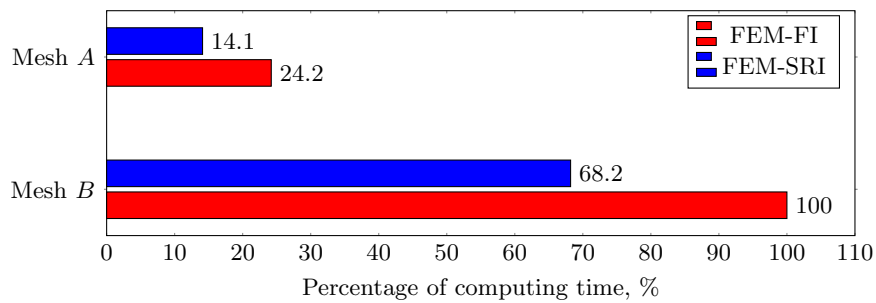


Figure 2.23. Computing time comparison for the non-linear analysis of the arcade

In fig. 2.24 can be seen the distribution of Von Mises stresses obtained for the four analyzed

cases. A clear similarity between the stress states for both cases can be observed, especially in the areas where the yield stress is reached.

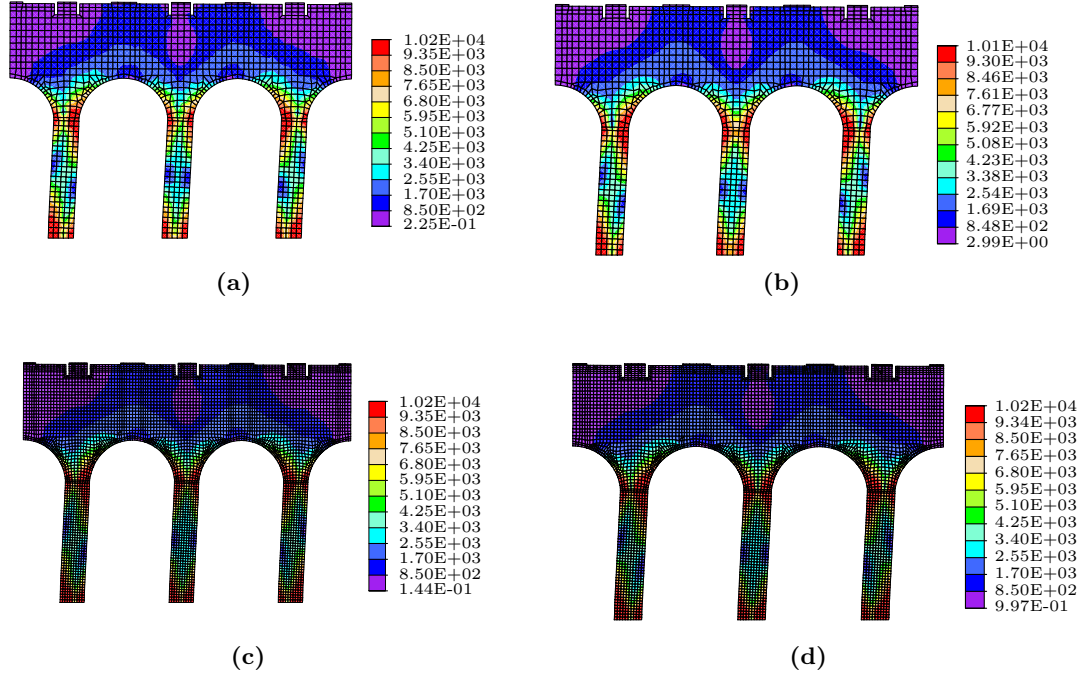


Figure 2.24. Von Mises stress distribution for mesh *A* with (a) SRI and (b) FI; and for the mesh *B* with (c) SRI and (d) FI

2.4.3.4 Typical colonial church of Puebla, Mexico

Additionally, a typical facade of a colonial church of Puebla, Mexico, was selected as another validation example. The purpose of this example is to compare the results numerically approximated by both FI and SRI. This facade is part of the scaled model tested by Chávez (2010) at the Institute of Engineering of the National Autonomous University of Mexico. The model was built using the construction techniques and materials accordingly to the period of time in which this kind of churches were built. A photograph of the experimental set-up of the model is shown in fig. 2.25.

As in the validation examples analyzed in the preceding subsections, the finite element method within SRI scheme was employed to numerically approximate the behaviour of the church facade. Following a macro-modelling approach, the mesh was proposed according to the geometry of the experimental model, shown in fig. 2.25. As in the previous examples, a strain-energy convergence test was carried out to select a good enough mesh density, and only 4-node quadrilateral elements were used so that the SRI scheme could be applied.

In this example, a plasticity constitutive model, based in the yield criterion developed by Drucker and Prager, was used. This model accurately describes pressure-sensitive



Figure 2.25. Experimental model of a typical colonial church of Puebla, Mexico (Chávez, 2010)

materials like concrete, masonry and soils. The mechanical parameters of the masonry, as homogenized material, were selected from the experimental test results reported in the work of Chávez (2010) (Table 2.5). In a first step, an eigenvalue analysis was performed in order to obtain the modal shapes of the facade. The first modal shape was used to create a displacement pattern that was imposed in the second step of the analysis, so that a possible deformed shape of the structure was simulated. The first three modal shapes of the facade are included in fig. 2.26.

Table 2.5. Mechanical parameters considered in the analysis of the church’s facade

Elasticity modulus	Poisson’s ratio	Tensile strength	Compressive strength
$E = 471 \text{ MPa}$	$\nu = 0.20$	$\sigma_t = 0.49 \text{ MPa}$	$\sigma_c = 3.9 \text{ MPa}$

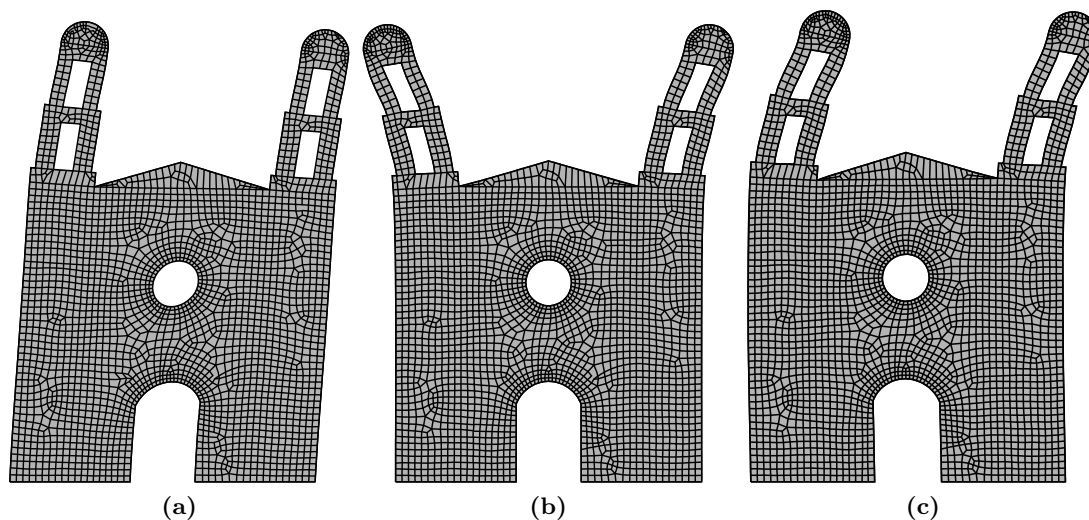


Figure 2.26. First three modal shapes of the facade

Here, three classical deformation modes of church facades can be identified. The main objective of this example is to demonstrate the efficiency of the numerical method proposed and how the solution for the aimed problems can be correctly computed using this proposal. Even though the lack of experimental results of this model to compare with the numerically

calculated using the SRI scheme, from the results shown in the reaction-displacement curve obtained from this analysis, fig. 2.27, it can be stated that the behaviour of the facade was coherent with the observations of the experiment. As a reference this figure also shows the results of the FI approximation. As it may be observed there is a high similarity of both curves for this mesh density; however, the computing time required by the SRI scheme is lower than that of the FI scheme (fig. 2.28).

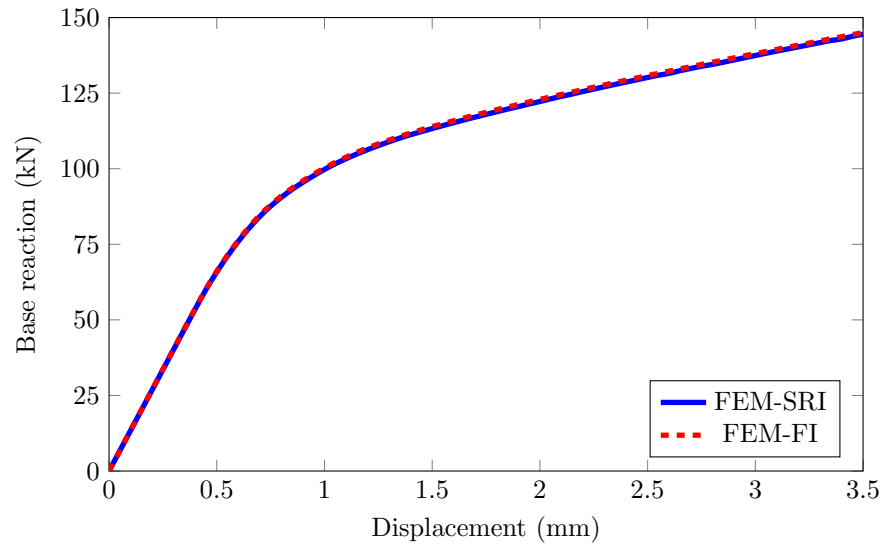


Figure 2.27. Reaction-displacement numerically approximated curves

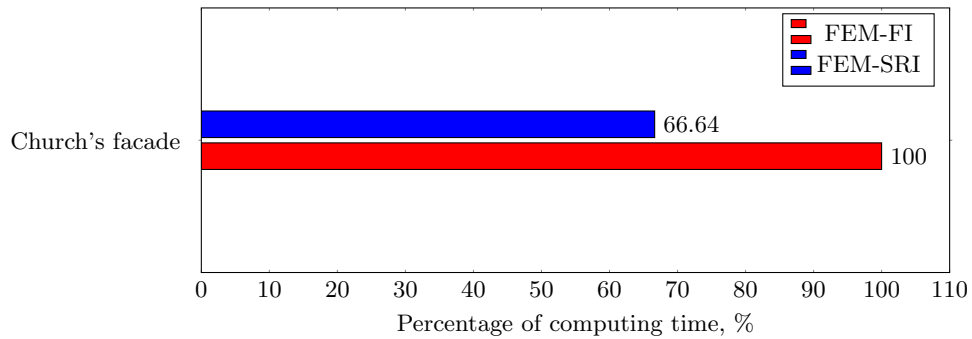


Figure 2.28. Computing time comparison for the non-linear analysis of the church's facade

2.4.4 Experimental data

In order to validate the SRI scheme, through a comparison against experimental data, this section includes two non-linear validation examples of masonry specimens which include a comparison with experimental data.

2.4.4.1 Wall panel

The test results of four single-leaf masonry wall panels, tested in the Heavy Structures Laboratory (Sarhosis, 2011), were used in this example. These wall panels, named as S1, S2, S3 and S4, were built to represent an external wall containing window openings. All panels were built with a row of bricks disposed vertically above the aperture, as shown in fig. 2.29 (Giamundo et al., 2014). According to the test description, each wall panel was subjected to a single vertical incremental load applied to a steel spreader plate placed in the upper central part of the wall (see fig. 2.29). This load was applied monotonically, and the central deflection was recorded at each load increment, so that the results could be compared to a numerical approximation.

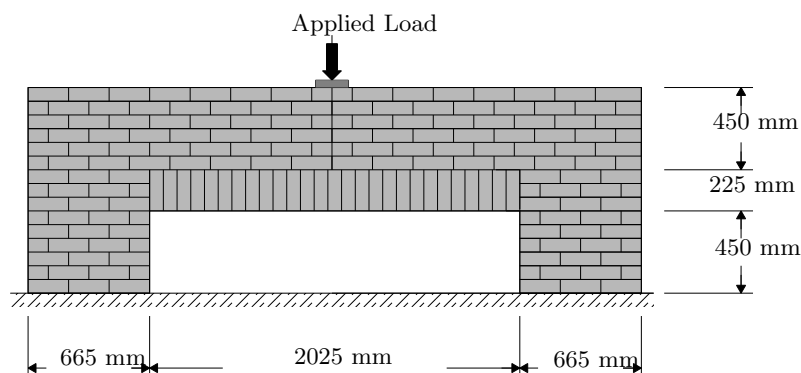


Figure 2.29. Wall panel tested in Heavy Structures Laboratory (Giamundo et al., 2014)

Following a macro-modelling approach, the mesh was proposed according to the geometry of the experimental model. Only 4-node quadrilateral elements were used so that the SRI scheme can be applied. A strain-energy convergence test was carried out to select a good enough mesh density (fig. 2.30). A plasticity constitutive model, based in the yield criterion developed by Drucker and Prager, was used. The mechanical parameters of the masonry component materials were selected from the experimental test report (Sarhosis, 2011) (table 2.6).

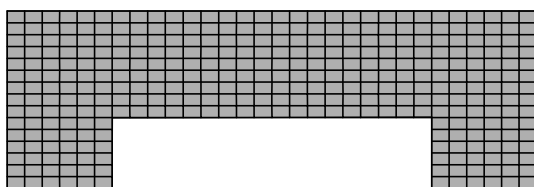


Figure 2.30. Mesh employed in the analysis of the wall panel

Table 2.6. Mechanical parameters considered in the analysis of the wall panel

Elasticity modulus	Poisson's ratio	Tensile strength	Compressive strength
$E = 111 \text{ MPa}$	$\nu = 0.15$	$\sigma_t = 0.05 \text{ MPa}$	$\sigma_c = 0.60 \text{ MPa}$

Both SRI and FI were used to analyze the non-linear problem. In fig. 2.31 the numerically approximated and experimental reaction-displacement curves are shown. From this

figure, it can be noted that the behaviour approximated by both integration schemes are similar to the results of three of the four tested specimens as the results of the specimen S1 were discarded due to construction issues (Sarhosis, 2011). This similarity is especially noticeable in the approximation of the load and displacement in which the yield state was started. Additionally, in fig. 2.32 a comparison in the computing-time required in the analysis for each integration scheme is included.

In fig. 2.33 are included six intermediate states of principal stresses of the analysis. These states are also indicated in fig. 2.31. The contours included in fig. 2.33b, corresponding to a 0.144 mm of deflection, where selected since is the displacement when the plastic deformation started to appear. This result is comparable with the reported by Giamundo et al. (2014) as the first crack deflection in the experiments which are included in table 2.7.

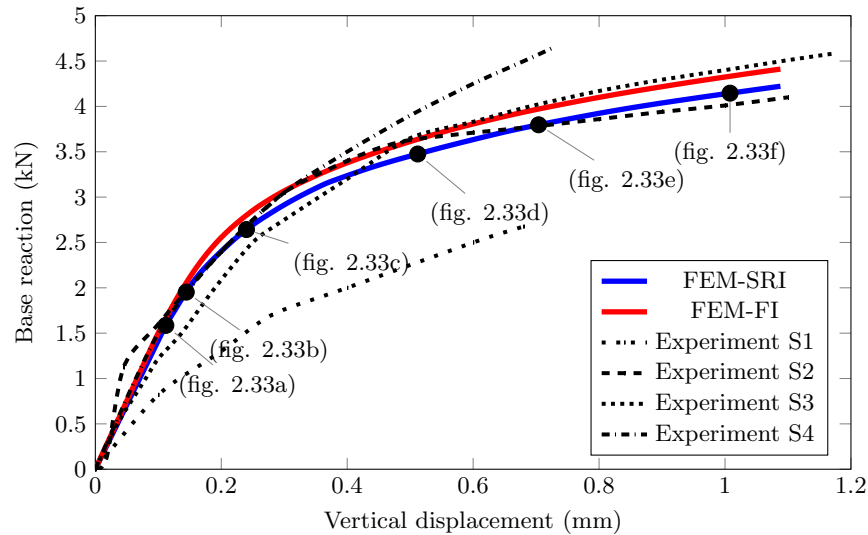


Figure 2.31. Reaction-displacement experimental and approximated curves

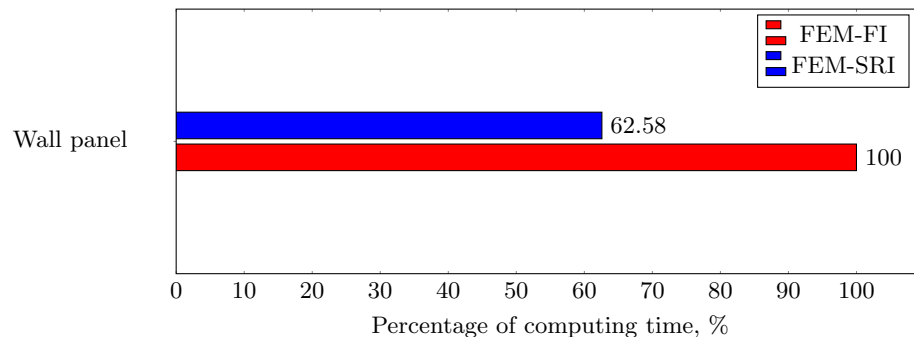


Figure 2.32. Computing times for the non-linear analyses of the wall panel

In fig. 2.34 a comparison of the FEM-SRI analysis against the numerical approximation obtained by Giamundo et al. (2014) through a micro-modelling approach is included. Here,

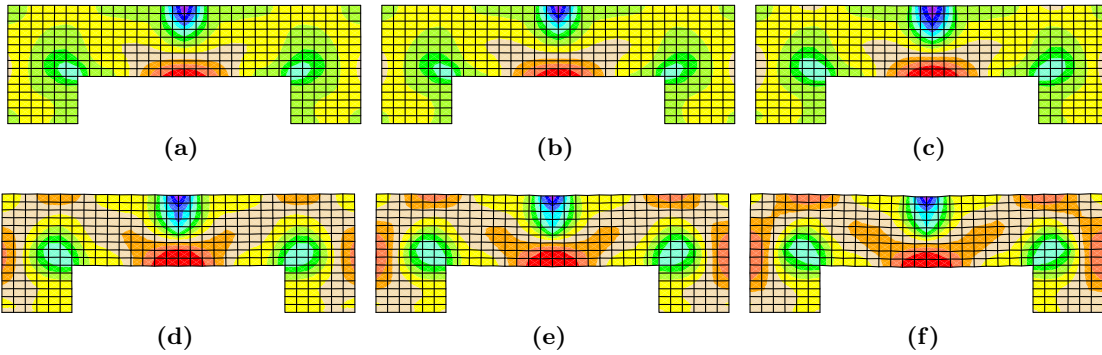


Figure 2.33. Six intermediate analysis states of principal stresses with SRI at displacement of (a) 0.112 mm, (b) 0.144 mm, (c) 0.240 mm, (d) 0.512 mm, (e) 0.704 mm and (f) 1.08 mm

Table 2.7. Experimental results for first cracking (Giamundo et al., 2014)

Panel ID	First crack load	First crack deflection
S1	1.60 kN	0.15 mm
S2	1.60 kN	0.10 mm
S3	1.71 kN	0.12 mm
S4	0.72 kN	0.08 mm

it can be seen that the zones where the principal stresses are high (fig. 2.34a) coincide with the smeared crack patterns (fig. 2.34b). Additionally, the damage observed un the wall panels at the end of the experiments are included in fig. 2.35.

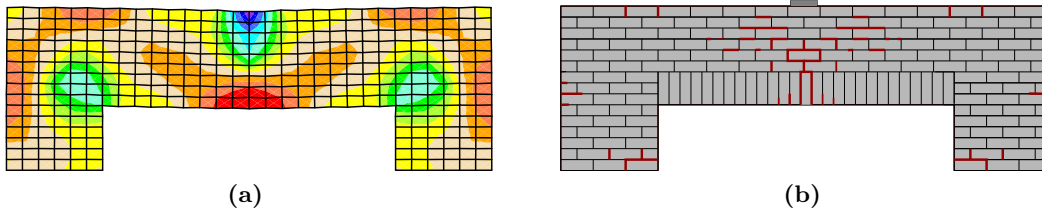


Figure 2.34. Comparison between (a) the principal stresses distribution obtained with SRI and (b) smeared crack patterns numerically approximated by Giamundo et al. (2014)



Figure 2.35. Damage observed in the experiment (Giamundo et al., 2014)

2.4.4.2 Arcade of São Vicente de Fora

The experimental results of the full-scale model of an arcade of the monastery (fig. 2.20), numerically analyzed in section 2.4.3.3, were used in this section. According to Pegon et al. (2001), the test model was built using materials and constructions techniques similar to the original structure. The test set-up is shown schematically in fig. 2.36. In order to

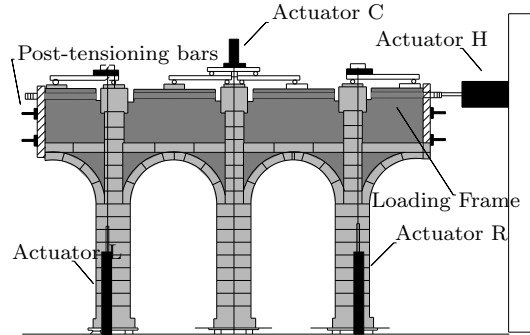


Figure 2.36. Test set-up of the model (Ambrosetti, 2000)

simulate the complete structure interaction, post-tensioning bars were confining the upper part of the specimen. Also, seven constant loads were imposed in the top of the model, simulating the presence of the upper levels. Furthermore, these vertical loads were useful to guarantee the stability of both experimental and numerical procedures. The seismic excitations were simulated by means of the imposition of incremental lateral loads, equally distributed to all the upper part of the full-scale model, through a loading frame. The testing program consists on several experiments such as the initial dynamic characterization, pseudo-dynamic and cyclic tests (Pinto et al., 1998). Therefore, the ultimate displacement of the experimental results, used in this work, was selected in order to guarantee that the specimen, after retrofitting, is still capable to complete such testing program. Accordingly, the numerical simulation was carried out with this ultimate displacement imposition. Two meshes were built, mesh *A* and mesh *B*, composed by 2161 and 7446 4-node quadrilateral finite elements, respectively (fig. 2.37). The numerical analysis was divided into two steps

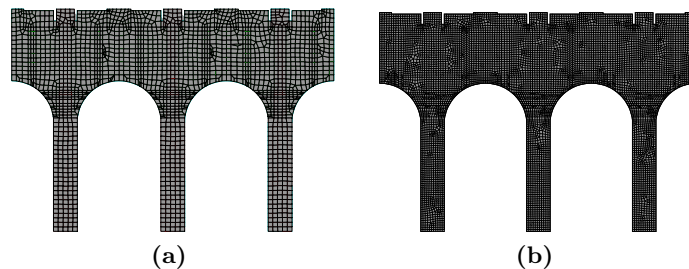


Figure 2.37. Meshes employed in the analysis: (a) mesh *A* and (b) mesh *B*

(figs. 2.38). In the first one, the effects of the vertical loads, such as the self-weight of the arcade and the columns from upper levels, were computed (fig. 2.38a). In a second step, lateral displacements were imposed all along the top-arcade elements in order to simulate the post-tensioning bars of the full-scale model (fig. 2.38b). A plasticity constitutive

2. REDUCED INTEGRATION IN THE FEM

model, based in the yield criterion developed by Drucker and Prager, was used. The mechanical parameters of the masonry were selected from the experimental test report (Table 2.8). Figure 2.39 shows the reaction-displacement curves of the experimental results and its numerical approximation employing both SRI scheme for mesh *A* and the FI scheme for mesh *B*.

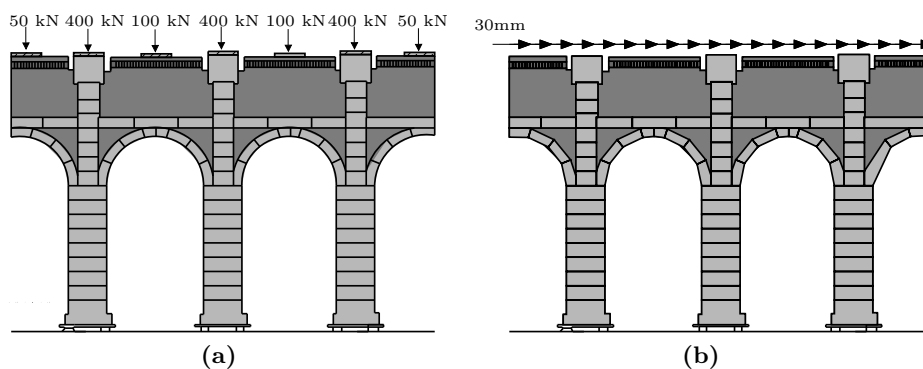


Figure 2.38. Analysis steps: (a) vertical loads and (b) lateral displacements

Table 2.8. Mechanical parameters considered in the analysis of the arcade

Elasticity modulus	Poisson's ratio	Tensile strength	Compressive strength
$E = 10500 \text{ MPa}$	$\nu = 0.20$	$\sigma_t = 2.65 \text{ MPa}$	$\sigma_c = 30.75 \text{ MPa}$

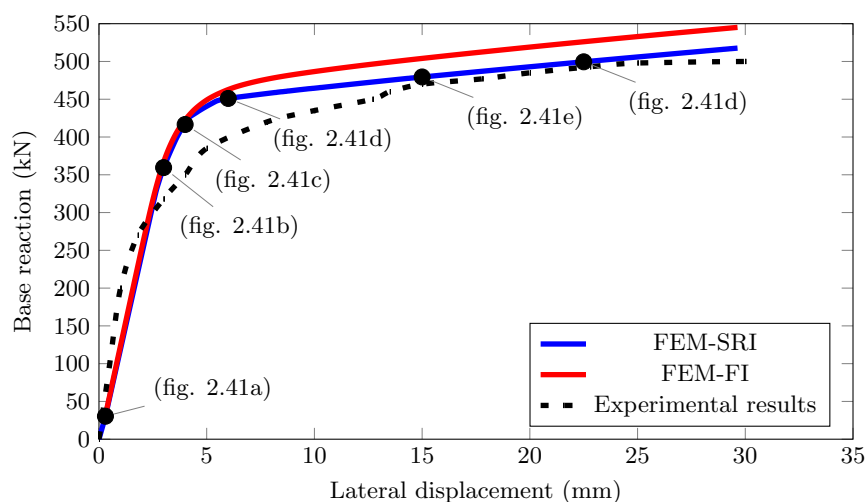


Figure 2.39. Experimental and numerical displacement-reaction curves

The curves of fig. 2.39 depict the evolution of the base shear forces with the lateral displacements imposed to the numerical model. From this figure, some remarks can be stated: (i) experimental and numerical curves, show similar behaviour, regardless the integration scheme employed, (ii) the results approximated through SRI and mesh *A* are closer to the reported in the experiment than the ones computed through FI and the

mesh B , and (iii) the yield displacement and the ultimate base reaction approximated with the SRI scheme have 5% of difference when compared to the experiment. These results obtained show the efficiency of the proposed SRI scheme for solving non-linear structural problems. The approximation reached with SRI for mesh A represents an 84.65 % decrease of the computational cost with respect to that of the FI scheme applied to mesh B , *i.e.*, approximately 6.51 times faster (fig. 2.40). The adopted constitutive model, used to reproduce the masonry behaviour, could be the cause of some differences between both curves, such as those on the total energy related to each one. Furthermore, the local hardening shown by the experimental results at 4 mm and 13 mm of lateral displacement was not reproduced by the numerical model. Six different intermediate analysis states of the maximum principal stresses distribution at several displacements are included in figs. 2.41a to 2.41f.

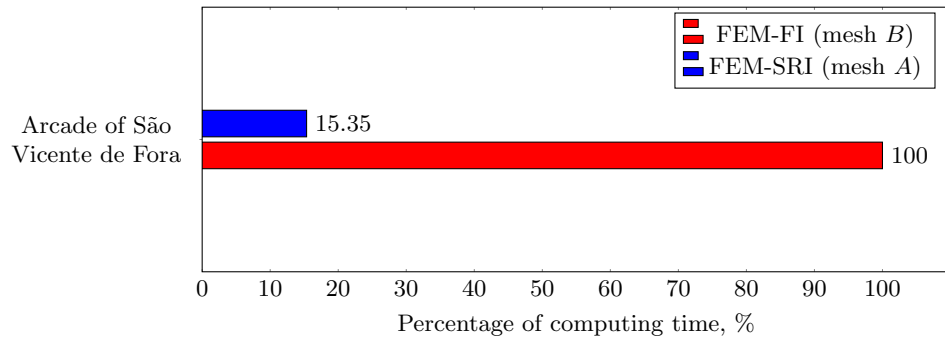


Figure 2.40. Computing times for the non-linear analyses of the Arcade of São Vicente de Fora

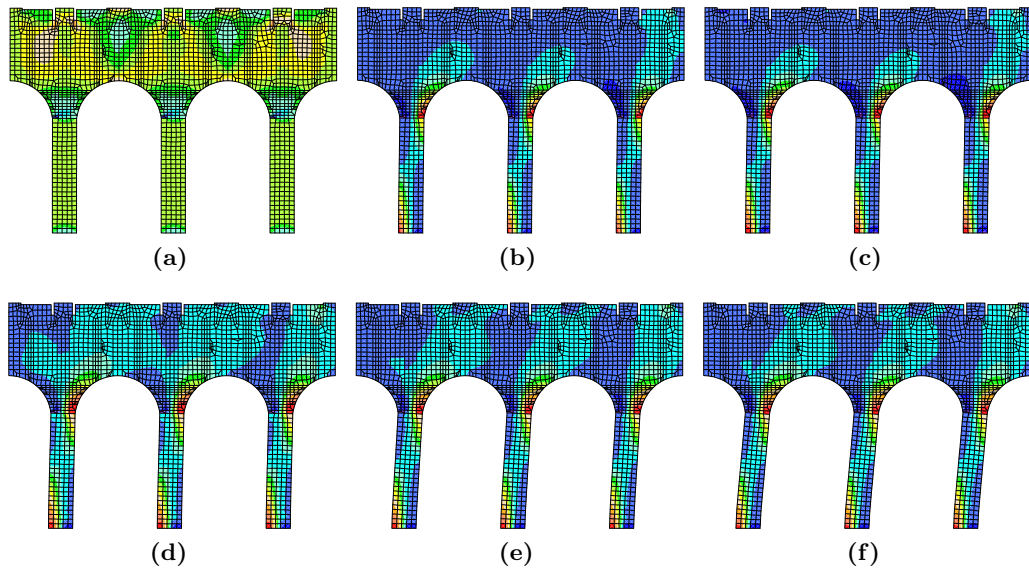


Figure 2.41. Six intermediate analysis states of principal stresses distribution with SRI at displacement of (a) 0.3 mm, (b) 3 mm, (c) 4 mm, (d) 6 mm, (e) 15 mm and (f) 22.5 mm

2. REDUCED INTEGRATION IN THE FEM

In fig. 2.42a the final state of the analysis can be observed and compared to the reported in experiments (fig. 2.42b). In this figures, it can be seen that the the regions where the highest principal stresses are numerical approximated match with the cracks reported in the experiment (Ambrosetti, 2000).

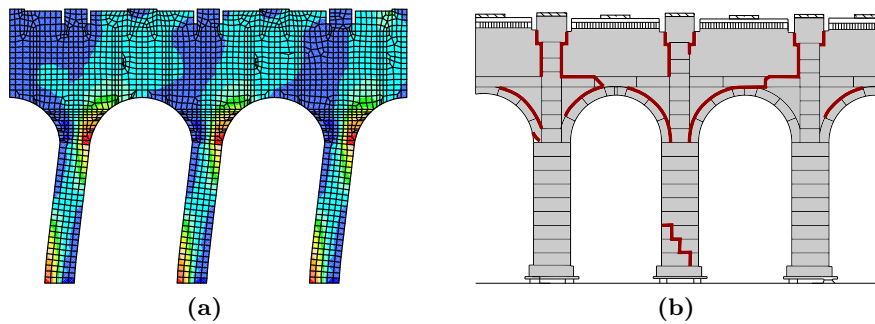


Figure 2.42. Comparison between (a) the principal stresses distribution obtained with SRI and (b) damage observed in experiment at displacement of 30 mm (Ambrosetti, 2000)

Non-linear behaviour of masonry

3.1 Introduction

In this chapter, computational aspects for modelling the non-linear mechanical behaviour of masonry are widely discussed. This discussion starts with discretization strategies of the masonry and, also, with a general description of the constitutive modelling for masonry as a structural material.

Moreover, the formulation of a constitutive model, based on the theories of plasticity and damage, suitable for cohesive-frictional materials, such as masonry and concrete, is studied and numerically implemented within the program *FEAP* (Taylor, 2017). Several debugging and validation tests were included along this chapter. These examples were analyzed employing the SRI scheme studied in the chapter 2.

In order to apply a complete and computationally efficient strategy for analyzing masonry structures, a homogenization strategy is described and numerically implemented. As well as in the numerical implementation of the constitutive model some debugging and validation examples were included in this section.

3.2 Numerical analysis of masonry by FEM

As mentioned in the introduction of this dissertation, the structural analysis of masonry constructions is a complicated task due to their irregular geometry and to the complex mechanical behaviour of masonry as a structural material. Nowadays, there are strategies for analyzing this type of problems, for example the Rigid Block Models, which consists on the modelling a structure as a set of rigid blocks interacting through their plane interfaces (Orduña, 2017). Also, the FEM, which solves the issue of an irregular geometry through the discretization of the structure into an ensemble of elements of simpler geometry. As this method requires the implementation of constitutive models to simulate the mechanical behaviour of masonry, its application involves a high computational cost in order to have a good enough approximation of the global performance of complex structures. Hence,

any strategy that reduces this computational cost is attractive to structural engineers.

3.2.1 Modelling strategies

The behaviour of masonry is highly dependent of the mechanical properties of its composing materials and, also, of the geometrical arrangement of them. For this reason, is important to know the behaviour of the units and the mortar by testing them separately and arranged as masonry. Consequently, masonry can be numerically modeled through two different approaches: micro- and macro-modelling. Whilst in the micro-models the units, the mortar, and the unit/mortar interface are discretized separately, in the macro-models masonry is treated as a unique composite material (Lourenço, 1996).

According to Lourenço (1996), micro-models are, probably, the best tool available to understand the behaviour of masonry. This is especially obvious when the main interest lays in the study of the local behavior of a masonry specimen, since all the different failure mechanisms are captured in this type of models. Moreover, since the units and the mortar are discretized separately, the behaviour of each material can be approximated through different constitutive models *ad hoc* to each one. Therefore, in micro-models is essential to know the mechanical properties of the units and the mortar independently.

In spite of the high sophistication level of the micro-models, they can be classified in detailed and simplified. In the detailed micro-models, the units and mortar in the joints are represented by continuum elements whereas the unit-mortar interface is represented by discontinuous elements (fig. 3.1); and in the simplified micro-models, expanded units are represented by continuum elements whereas the behaviour of the mortar joints and unit-mortar interface is lumped in discontinuous elements (Lourenço, 1996).

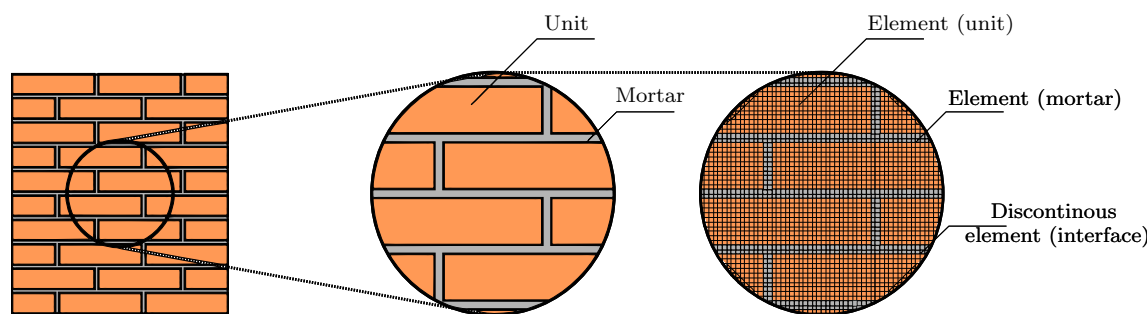


Figure 3.1. Detailed micro-modelling strategy for masonry

The main drawbacks of the micro-models is the high computational cost required for carrying out an analysis, and for building the mesh, avoiding all the compatibility issues, *e.g.*, pre-process stage. This is specially inconvenient when the structure to be analyzed is considerably large in size, which is common in the massive masonry structures.

As mentioned above, in the macro-models, the masonry is idealized as an unique homogeneous material in spite of its heterogeneous nature (fig. 3.2). Thus, the application of macro-models usually relies on the use of homogenization techniques. These techniques

are formulated to capture the behaviour of an isolated portion of the masonry, as an heterogeneous material, in the constitutive formulation of a new homogenized material. Some techniques for the homogenization process of masonry existing in the literature are those presented by Page (1978), Pietruszczak and Niu (1992), Anthoine (1995), Lourenço (1996) and López et al. (1998).

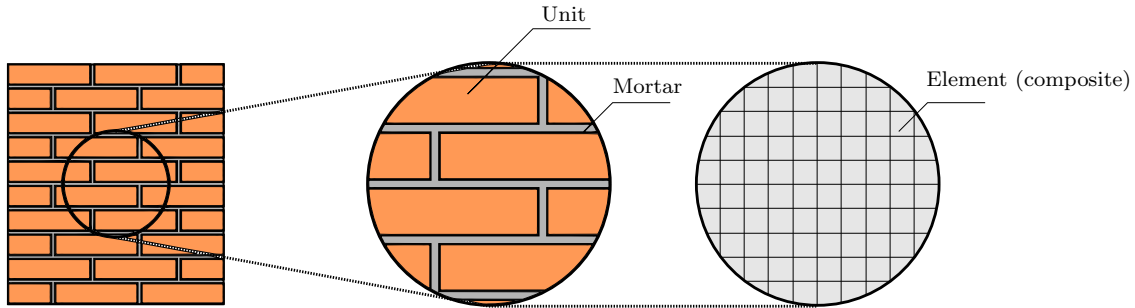


Figure 3.2. Macro-modelling strategy for masonry

Accordingly, the pre-process in macro-models is much more easier than in micro-models. Additionally, regarding the possibility of using macro-elements, *i.e.*, big portions of the structure which contains both mortar and units indistinctly, this strategy is computationally optimal for analyzing large-sized structures. Nevertheless, it should be taken into consideration that its application is focused for those analysis in which the objective is to study the global behaviour of the specimen and, for local behaviour analysis, micro-models, as mentioned above, are the best tool.

3.2.2 Mechanical behaviour

It is well known that the compressive strength of masonry is high in comparison to its tensile strength. Accordingly, the cracking is commonly caused by tensile stresses that are produced for different patterns of lateral loads, such as the ones generated for seismic movements (López et al., 1998). Therefore, those constitutive models based on yield criteria that consider a different strength for tension and for compression are ideal to model the masonry, *e.g.*, Mohr-Coulomb and Drucker-Prager yield criteria.

According to Oller (2001), a constitutive model is a mathematical formulation capable of describing the macroscopic physical behaviour of an ideal solid, which results from applying simplifying hypotheses to a real solid. Hence, the formulation of constitutive models only represents a reality conditioned by certain simplifying hypotheses and consequently their use must be carried out accordingly.

In the academic literature, the constitutive models are classified depending on the theories in which are based. Thus, generally, there are constitutive models based on the elasticity, plasticity or damage theory. The suitability of the application of each type of model depends on the material and/or the considered loading conditions of the analysis. Nevertheless, as stated above, these models are aimed to idealized materials, *e.g.*, materials that can be perfectly modeled with certain constitutive model, but not to real materi-

als. Therefore, in order to have a good enough approximation of the behaviour of real materials, constitutive models which combine more than one theory become attractive.

3.3 Plastic-damage constitutive model

In the case of masonry, as a cohesive-frictional material, *i.e.*, those whose behaviour depends on the angle of internal friction and exhibit the phenomenon of dilatancy (Oller, 2001), a constitutive model, which combines both plasticity and damage theories is optimal. Accordingly, in this research, the plastic-damage constitutive model proposed by Oller et al. (1988) and Lubliner et al. (1989) is used. Initially, this constitutive model was formulated for concrete (Oller, 1991), but in the work of López et al. (1998) was particularized for masonry. This particularization is essentially based on adjusting the domain of the yield function so that it adequately represents the values of the angle of internal friction and the ratio of tensile and compressive strengths for a given material.

3.3.1 Formulation

For describing a certain constitutive model formulation is important to establish the simplifying hypotheses on which it is based. Some of the most relevant hypotheses that Oller (2001) stated for this plastic-damage constitutive model are the following:

- The permanent deformations of the cohesive-frictional material, *i.e.* plastic deformations, can be interpreted as micro-cracks.
- The material can present a volume change behaviour, which can be identified as the dilatancy phenomenon, during the inelastic stage.
- The strength of the material evolves with the evolutionary process of loading, *i.e.* tension-tension, tension-compression and compression-compression.
- During the entire process of loading there is a continuous and increasing degradation of stiffness.

The formulation of the constitutive model is based on an extension of the basic principles of the theory of plasticity, reinterpreting its fundamental variables. For example, from the classic hardening variable the plastic-damage variable is formulated as an internal variable (Oller, 2001).

3.3.1.1 Internal variables (ε^p , κ^p y c)

This plastic-damage constitutive model uses in its definition three internal variables that are grouped in a vector \mathbf{q} defined in eq. 3.1.

$$\mathbf{q} = \begin{Bmatrix} \varepsilon^p \\ \mathbf{q}_\alpha \end{Bmatrix} = \begin{Bmatrix} \varepsilon^p \\ \kappa^p \\ c \end{Bmatrix} \quad (3.1)$$

Here, $\boldsymbol{\varepsilon}^p$, the fundamental internal variable, is the plastic deformation, κ^p is the plastic-damage variable and c is the cohesion of the material. The plastic-damage variable is treated as a dimensionless variable that varies from 0 to 1, $0 \leq \kappa^p \leq 1$. As expected, when $\kappa^p = 0$ there is no plastic damage and $\kappa^p = 1$ represents total damage for certain point of the solid which can be interpreted as total loss of strength and, from a physical point of view, as a dismemberment of the mass, *i.e.*, physical discontinuity (Oller, 2001).

The cohesion is also treated as a magnitude that evolves with the plastic-damage variable. At the start of the analysis, when $\kappa^p = 0$, an initial cohesion is defined as an input parameter for the material. Accordingly, a final cohesion is defined for $\kappa^p = 1$ corresponding to a totally damaged material, $c = 0$ (Oller, 2001). Each of these variables evolves according to certain law (eq. 3.2).

$$\dot{\mathbf{q}} = \begin{Bmatrix} \dot{\boldsymbol{\varepsilon}}^p \\ \dot{\kappa}^p \\ \dot{c} \end{Bmatrix} \equiv \dot{\lambda} \cdot \mathbf{H} = \dot{\lambda} \cdot \begin{Bmatrix} \frac{\partial \mathbb{G}}{\partial \boldsymbol{\sigma}} \\ \mathbf{h}_\kappa : \frac{\partial \mathbb{G}}{\partial \boldsymbol{\sigma}} \\ h_c \cdot \mathbf{h}_\kappa : \frac{\partial \mathbb{G}}{\partial \boldsymbol{\sigma}} \end{Bmatrix} \equiv \begin{Bmatrix} \dot{\boldsymbol{\varepsilon}}^p \\ \mathbf{h}_\kappa : \dot{\boldsymbol{\varepsilon}}^p \\ h_c \cdot \mathbf{h}_\kappa : \dot{\boldsymbol{\varepsilon}}^p \end{Bmatrix} \quad (3.2)$$

In this equation, \mathbb{G} is the plastic potential criterion and the terms \mathbf{h}_κ and h_c are a second order tensor and a scalar function respectively, which depend on the current state of the elastic deformations and the rest of the internal variables (Oller, 2001). From the above, it can be observed that the fundamental internal variable is the plastic deformation, $\boldsymbol{\varepsilon}^p$, since the remaining variables depend on it (κ^p and c). Also, λ is the plastic consistency parameter which is computed and verified through the radial return algorithm described in the work of Oller (1991) (see fig. 3.5).

3.3.1.2 Plastic yield criterion (\mathbb{F})

The plastic yield criterion of this plastic-damage constitutive model can be mathematically expressed as the following equation:

$$\mathbb{F}(\boldsymbol{\sigma}, c) = f(\boldsymbol{\sigma}) - c = 0 \quad (3.3)$$

where $f(\boldsymbol{\sigma})$ is the plastic yield function that depends of the components of stress tensor, $\boldsymbol{\sigma}$, and c is the cohesion defined above as a internal variable. In this research, the Mohr-Coulomb yield function, modified by López et al. (1998), is used (eq. 3.4).

$$f(\boldsymbol{\sigma}) = \frac{I_1}{3} K_3 + \sqrt{J_2} \left[K_1 \cos \theta - K_2 \frac{\sin \theta \sin \phi}{\sqrt{3}} \right] \quad (3.4)$$

Here, I_1 y J_2 are the invariants of the volumetric and deviatoric part of the stress tensor; θ is the Lode's angle; ϕ is the angle of internal friction (for masonry: $30^\circ \leq \phi \leq 35^\circ$); and the constants K_1 , K_2 and K_3 that are computed using eq. 3.5.

$$\begin{aligned}
 K_1 &= \left[\frac{1 + \alpha_R}{2} - \frac{1 - \alpha_R}{2} \sin \phi \right] \\
 K_2 &= \left[\frac{1 + \alpha_R}{2} - \frac{1 - \alpha_R}{2} \frac{1}{\sin \phi} \right] \\
 K_3 &= K_2 \sin \phi
 \end{aligned} \tag{3.5}$$

Constants K_1 , K_2 y K_3 work as a setting parameter so that the value of the ratio of tensile and compressive strengths is the desired one for the masonry, while maintaining the angle of internal friction in the common domain of the masonry.

3.3.1.3 Angle of internal friction (ϕ)

According to Oller (2001), in fragile materials with high initial cohesion, such as masonry, it is possible to use a constant and maximum internal angle of friction during the whole plastic process without this leading to unsatisfactory results in the approach of multidimensional problems. Nevertheless, in this plastic-damage constitutive model the angle of friction can be also defined as an internal variable through a evolution law that depends on the elastic-plastic process.

3.3.1.4 Angle of dilatancy (ψ)

Commonly, the so called angle of dilatancy is an appropriate parameter to asses the phenomenon of dilatancy, *i.e.* the apparent change in inelastic volume due to plastic distortion effect, that is present in frictional materials, such as masonry. This angle represents the relationship between the increase in plastic volume and plastic distortion. In this plastic-damage constitutive model, the dilatancy is controlled using a non-associated plasticity, which means that the plastic yield function is different from the plastic potential function, $\mathbb{F}(\boldsymbol{\sigma}, \mathbf{q}) \neq \mathbb{G}(\boldsymbol{\sigma})$ (Oller, 2001).

3.3.1.5 Hardening plastic parameter (A)

According to the theory of plasticity, there are two types of hardening: isotropic and kinematic. The isotropic hardening corresponds to a homothetic transformation of the yield surface either expansion or contraction, *i.e.*, isotropic elastic-plastic process with hardening or softening, respectively (fig. 3.3a). On the other hand, the kinematic hardening is represented through a translation movement of the yield surface (fig. 3.3b) (Olivella and de Saracibar, 2002). This plastic-damage constitutive model is formulated to consider both isotropic and kinematic hardening through the plastic hardening parameter, A (eq. 3.6).

$$A = \underbrace{-c_k \frac{\partial \mathbb{F}}{\partial \boldsymbol{\eta}} : \frac{\partial \mathbb{G}}{\partial \boldsymbol{\sigma}}}_{\text{Kinematic}} + \underbrace{h_{\kappa} \mathbf{h}_{\kappa} : \frac{\partial \mathbb{G}}{\partial \boldsymbol{\sigma}}}_{\text{Isotropic}} \tag{3.6}$$

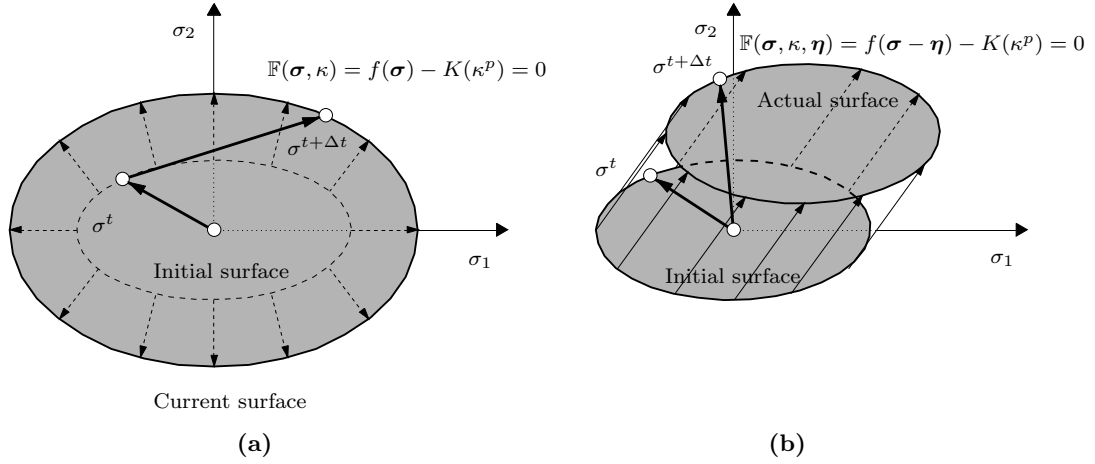


Figure 3.3. Yield surface transformation considering: (a) isotropic hardening and (b) kinematic hardening (Oller, 2001)

Regarding the kinematic hardening, η is the variable of kinematic plastic hardening, which is included in the modified Mohr-Coulomb yield function: $f(\boldsymbol{\sigma} - \boldsymbol{\eta})$ (eq. 3.4). The isotropic hardening is considered through the plastic hardening function $K(\kappa^p)$ which depends on the plastic-damage variable, κ^p . Therefore, in the most general case, the yield criterion can be written as in the following equation (eq. 3.7) (Oller, 2001).

$$\mathbb{F}(\boldsymbol{\sigma}, \mathbf{q}) = f(\boldsymbol{\sigma} - \boldsymbol{\eta}) - K(\kappa^p) = 0 \quad (3.7)$$

3.4 Numerical implementation

In order to apply the formulation of the plastic-damage constitutive model briefly described along the chapter, it is required to perform a numerical implementation. According to this dissertation objectives, the implementation was carried out through the proposed SRI scheme for the FEM. Therefore, the computational environment selected for the numerical implementation is the non-linear analysis program *FEAP* (Taylor, 2017), since the SRI scheme was also implemented in this program. This software allows the edition of user routines to include certain constitutive model.

In general terms, the implemented user routine follows the steps summarized in the fig. 3.4. Particularly, for the integration of the constitutive equation which corresponds to the step number 3 in the diagram of fig. 3.4, an iterative process is required to calculate the increment of the plastic consistency parameter, $\Delta\lambda$, which projects, to the yield surface, the stress prediction that is initially outside of it, *i.e.*, plastic step. This radial return algorithm for the implicit integration process is summarized in the fig. 3.5.

Additionally, a flow diagram of the plastic-damage constitutive model implementation in the program *FEAP* (Taylor, 2017) is included in fig. 3.6. The flow diagram starts when

3. NON-LINEAR BEHAVIOUR OF MASONRY

an increment of displacement, $\Delta \mathbf{d}$, is imposed to the structure, *i.e.*, step of the non-linear analysis. A trial stresses are computed assuming that the material remains elastic and, then, this assumption is reviewed by the evaluation of the yield condition. This evaluation allows the classification of the step as either elastic or plastic.

1. Computation of the stress prediction for the current time, $t + \Delta t$. Here, the equilibrium iteration is represented by i , and the convergence counter starts at $k = 1$

$$\begin{aligned} {}^i_{k-1}[\boldsymbol{\sigma}]^{t+\Delta t} &= \mathbb{C} : ([\boldsymbol{\epsilon}]^{t+\Delta t} - {}^{i-1}[\boldsymbol{\epsilon}^p]^{t+\Delta t}) \\ {}^i_{k-1}[\mathbf{q}]^{t+\Delta t} &= {}^{i-1}[\mathbf{q}]^{t+\Delta t} \end{aligned} \quad (3.8)$$

2. Evaluation of the plastic yield condition

- a. If $\mathbb{F}({}^i_{k-1}[\boldsymbol{\sigma}]^{t+\Delta t}, {}^i_{k-1}[\mathbf{q}]^{t+\Delta t}) < 0$, $\left\{ \begin{array}{l} {}^i[\boldsymbol{\sigma}]^{t+\Delta t} = {}^i_{k-1}[\boldsymbol{\sigma}]^{t+\Delta t} \\ {}^i[\mathbf{q}]^{t+\Delta t} = {}^i_{k-1}[\mathbf{q}]^{t+\Delta t} \end{array} \right\}$ and ends
- b. If $\mathbb{F}({}^i_{k-1}[\boldsymbol{\sigma}]^{t+\Delta t}, {}^i_{k-1}[\mathbf{q}]^{t+\Delta t}) \geq 0$, go to step 3

3. Integration of the constitutive equation

$$\Delta \lambda = \frac{\mathbb{F}({}^i_{k-1}[\boldsymbol{\sigma}]^{t+\Delta t}, {}^i_{k-1}[\mathbf{q}]^{t+\Delta t})}{\underbrace{\left[-c_k \frac{\partial \mathbb{F}}{\partial \boldsymbol{\eta}} : \frac{\partial \mathbb{G}}{\partial \boldsymbol{\sigma}} + h_\kappa \mathbf{h}_k : \frac{\partial \mathbb{G}}{\partial \boldsymbol{\sigma}} \right]}_{{}^i_{k-1}A^{t+\Delta t}} + \underbrace{\left(\frac{\partial \mathbb{F}}{\partial \boldsymbol{\eta}} : \mathbb{C} : \frac{\partial \mathbb{G}}{\partial \boldsymbol{\sigma}} \right)}_{{}^i_{k-1}T^{t+\Delta t}}} \quad (3.10)$$

$${}^i_k[\boldsymbol{\sigma}]^{t+\Delta t} = {}^{i-1}[\boldsymbol{\sigma}]^{t+\Delta t} - \Delta \lambda \mathbb{C} : \left(\frac{\partial \mathbb{G}}{\partial \boldsymbol{\sigma}} \right)$$

4. Update of the internal variables and the constitutive tangent tensor with the new stress state

$$\begin{aligned} {}^i_k[\mathbf{q}]^{t+\Delta t} &= {}^{i-1}[\mathbf{q}]^{t+\Delta t} \\ {}^i_k[\mathbb{C}_T]^{t+\Delta t} &= \left[\mathbb{C} - \frac{\left[\mathbb{C} : \frac{\partial \mathbb{F}}{\partial \boldsymbol{\eta}} \right] \otimes \left[\frac{\partial \mathbb{G}}{\partial \boldsymbol{\sigma}} : \mathbb{C} \right]}{\left[-c_k \frac{\partial \mathbb{F}}{\partial \boldsymbol{\eta}} : \frac{\partial \mathbb{G}}{\partial \boldsymbol{\sigma}} + h_\kappa \mathbf{h}_k : \frac{\partial \mathbb{G}}{\partial \boldsymbol{\sigma}} \right] + \left(\frac{\partial \mathbb{F}}{\partial \boldsymbol{\eta}} : \mathbb{C} : \frac{\partial \mathbb{G}}{\partial \boldsymbol{\sigma}} \right)} \right] \end{aligned} \quad (3.11)$$

5. $k = k + 1$ and returns to step 2

Figure 3.4. Plastic-damage constitutive model algorithm (Oller, 2001)

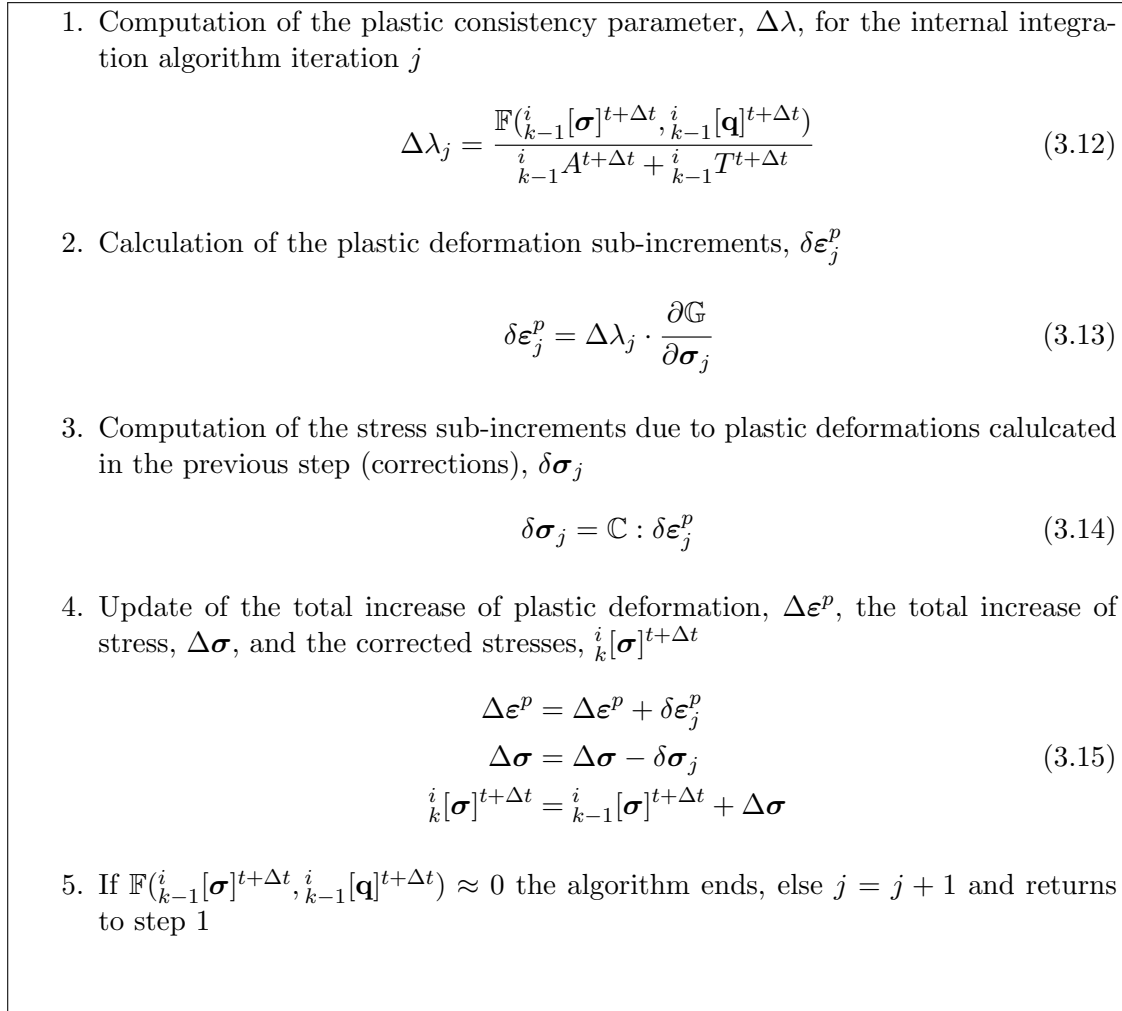


Figure 3.5. Radial return algorithm for the implicit integration of the constitutive equation

3.5 Debugging tests

One of the most time-consuming stages required for programming an algorithm is the debugging process, especially in large or complex algorithms as the that of the plastic-damage constitutive model described above. In this phase, several test must be carried out in order to detect code errors and, consequentially, to solve them. Also, these tests are useful to make comparison between the obtained results with the expected ones. The following tests, among others, were carried out to debug the numerical implementation of the plastic-damage constitutive model.

3.5.1 Behaviour tests

First, the algorithms described in the section 3.4 were implemented in the program *MATLAB* (MathWorks, 2019) to obtain the stress-strain characteristic curve of this constitu-

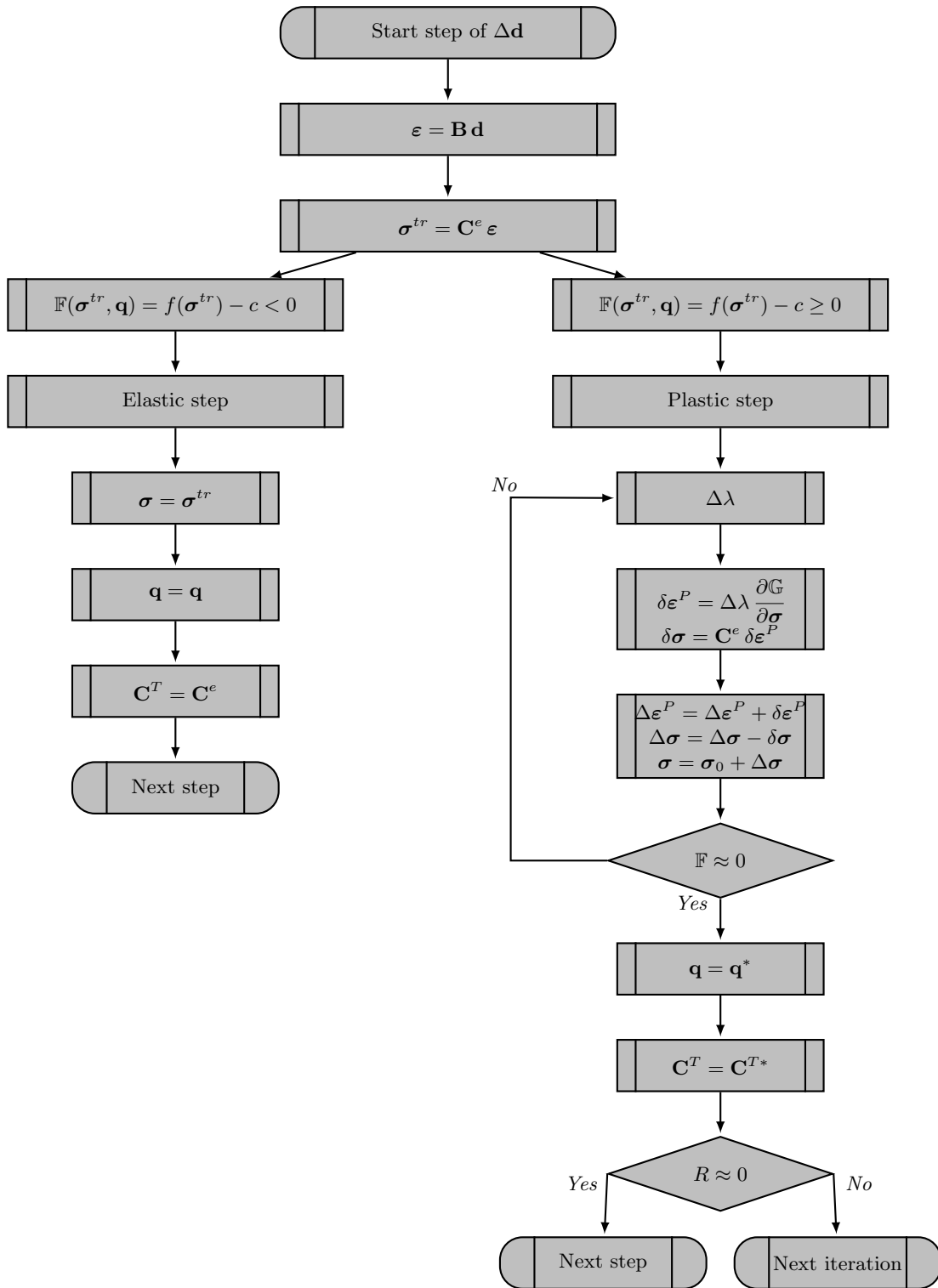


Figure 3.6. Flow diagram of plastic-damage constitutive model implementation in *FEAP* (Taylor, 2017)

tive model. For this purpose, incremental one-dimensional deformations were imposed at compression and tension and the corresponding stresses were computed. The resulting stress-strain curves are shown in fig. 3.7 for both tension and compression.

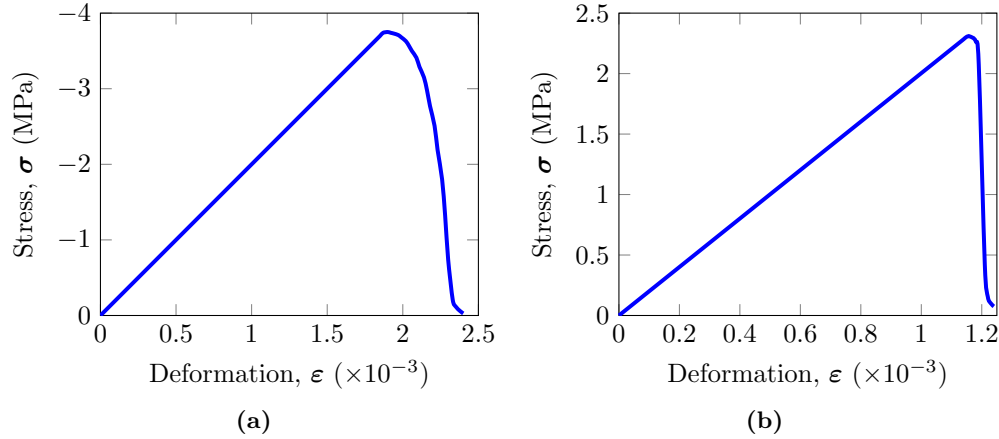


Figure 3.7. Plastic-damage constitutive model behaviour test: (a) to compression y (b) to tension

In addition to these curves, the evolutions of the internal variables of plastic damage, κ^p , and cohesion, c , were obtained. These evolutions are shown in fig. 3.8. Here, it can be seen how the plastic damage variable grows from 0 to 1, as the plastic deformation increases, and the cohesion of the material degrades from its initial value to 0, as expected.

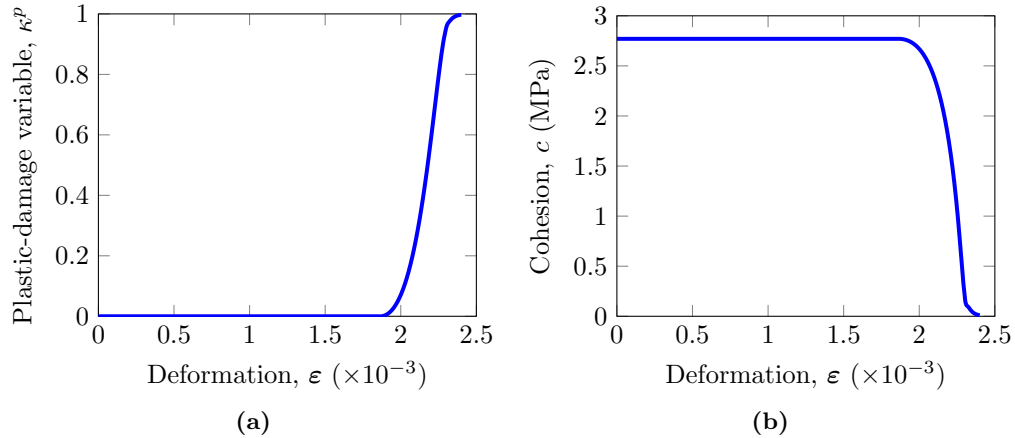


Figure 3.8. Evolution of the internal variables: (a) plastic-damage variable, κ^p , and (b) cohesion, c

These tests were useful to state that the behaviour of the implemented algorithm is the expected one, so the mathematical expressions, derived from the ones stated in the formulation of the plastic-damage constitutive model, can be assumed as correct (see fig. 3.11).

3.5.2 Behaviour tests with SRI scheme

As a second step, the plastic-damage constitutive model was implemented in FEAP (Taylor, 2017) following the flow diagram of fig. 3.6. This implementation was coded to be applied through the SRI scheme, proposal of this thesis. Accordingly, special care was taken in order to guarantee the compatibility with the element user routine implemented for the SRI scheme.

3.5.2.1 Unidimensional test

The debugging process of the implemented user routine started with the analysis of an unidimensional problem. For this purpose, a mesh, composed by a single 4-node quadrilateral finite element, was built with the restraints shown in fig. 3.9. Displacements, δ , were imposed on this element in horizontal direction, as indicated in fig. 3.9, in such a way that tension and compression behaviour were generated. The analysis was carried out with a null value of Poisson's ratio, $\nu = 0$, with mechanical properties that are usual for masonry and employing the SRI scheme. One of the curves obtained, corresponding to a tension behaviour, is shown in fig. 3.10. In this figure it can be seen that the approximated behaviour is the expected one for a tension displacement imposition, *i.e.*, the shape of the curve correspond to the one established in the formulation of the plastic-damage constitutive model (fig. 3.11).

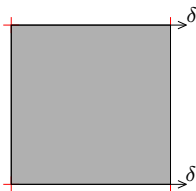


Figure 3.9. 4-node quadrilateral finite element proposed for the unidimensional test

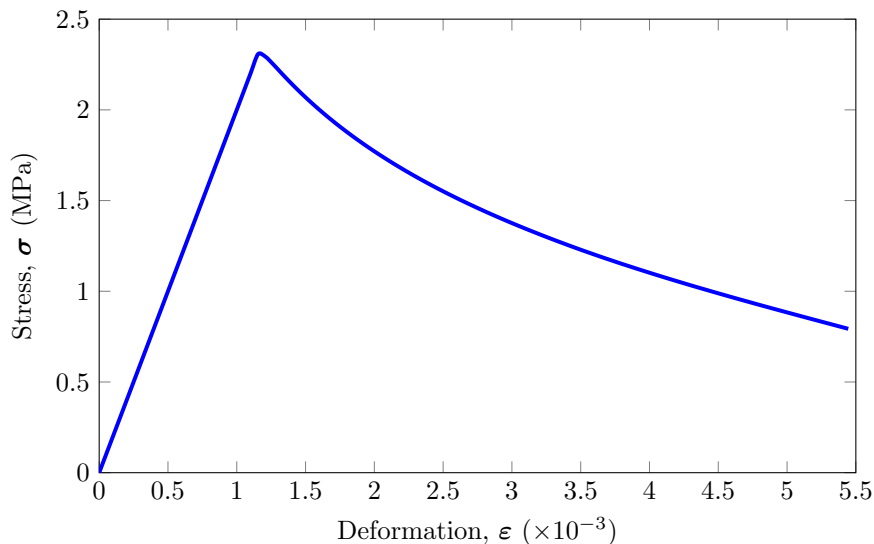


Figure 3.10. Unidimensional tension test

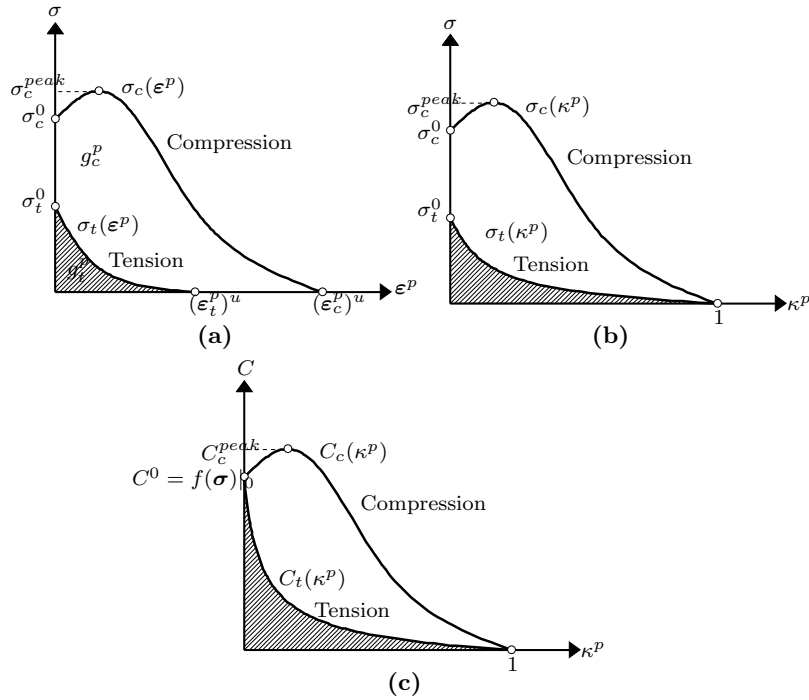


Figure 3.11. Transformation of the uniaxial strength measured in laboratory to the uniaxial strength employed in the plastic-damage constitutive model (Oller, 2001): (a) uniaxial strength in function of plastic deformation, (b) uniaxial strength in function of the plastic damage variable and (c) the cohesion depending of the plastic damage variable

3.5.2.2 Bidimensional test

Additionally, a mesh composed of 4 quadrilateral finite elements of linear approximation was built (fig. 3.12). The SRI scheme, proposed in this research, was also used in these tests. The material behaviour was approximated employing the plastic-damage constitutive model considering the mechanical parameters of table 3.1 and, also a tensile-compressive strength ratio $\sigma_c/\sigma_t = 8$ and an ultimate compressive strain $\varepsilon_c = 1.25$.

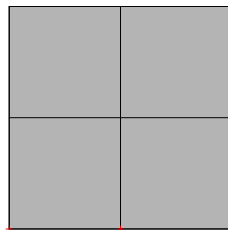


Figure 3.12. Proposed mesh for the behaviour tests with the SRI scheme

The modified Newton-Raphson method was used for the numerical approximation of the non-linear problem. To analyze the proposed problem positive vertical, negative vertical and lateral positive displacements were imposed on all the upper nodes of the mesh shown in fig. 3.12, so that the generated behaviour corresponded to tension, compression and shear, respectively.

3. NON-LINEAR BEHAVIOUR OF MASONRY

Table 3.1. Mechanical parameters considered for the bidimensional test

Elasticity modulus	Poisson's ratio	Angle of friction	Compressive strength
$E = 2000 \text{ MPa}$	$\nu = 0.20$	$\phi = 0.60$	$\sigma_c = 50 \text{ MPa}$

The reaction-displacement diagrams obtained for tension and compression are shown in figs. 3.13a and 3.13b. In these diagrams, it can be seen that the numerically approximated behaviours are consistent with the expected ones (see fig. 3.11). It is worth mentioning that no convergence problems were presented due to the simplicity of the analyzed problems. Furthermore, fig. 3.13c contains the reaction-displacement diagram for the positive lateral displacement imposition. According to the uniaxial curves of 3.11, it can be stated that the shear behaviour is mostly governed by tension.

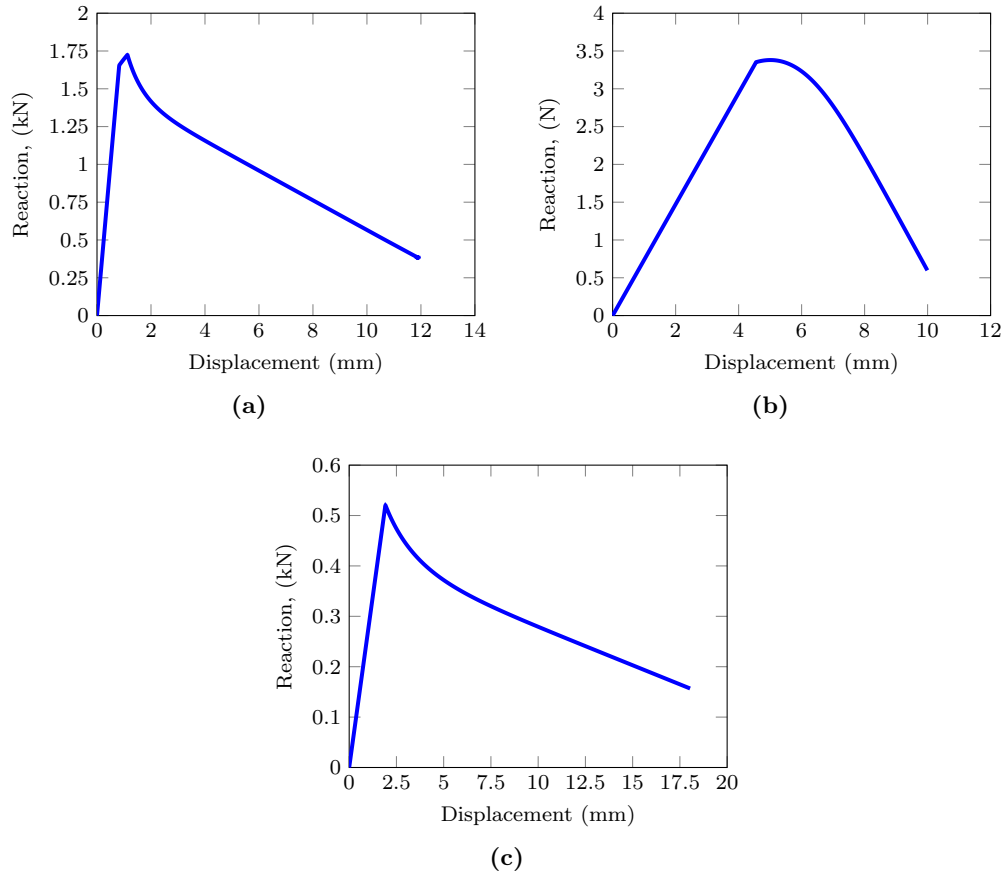


Figure 3.13. Displacement-reaction diagram of the 4-element mesh for (a) tension, (b) compression and (c) shear displacements impositions

Additionally, in the figs. 3.14a and 3.14b are included the states of the plastic-damage variable and cohesion corresponding to the last step of the incremental shear displacements imposition, respectively. In these figures the influence of the plastic-damage variable on the degradation of the cohesion of the material can be observed. This is consistent with the degradation of the material reflected in the downward branch of the reaction-displacement

curve of fig. 3.13c.

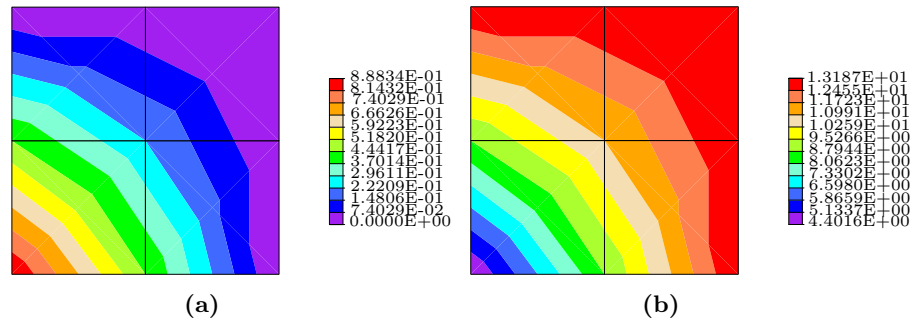


Figure 3.14. State of the internal variables at the end of the analysis (shear displacement imposition): (a) plastic-damage variable and (b) cohesion

3.5.2.3 Internal variables evolution

In this section, an additional example to show the influence of the plastic-damage variable on the degradation of the cohesion of the masonry, is included. For this example, a mesh with 420 4-node quadrilateral finite elements was built and analyzed using the SRI scheme studied in this dissertation. Lateral displacements were imposed on the upper nodes of the mesh to simulate the behaviour of a wall under lateral loads. The fig. 3.15 includes the numerically computed reaction-displacement diagram.

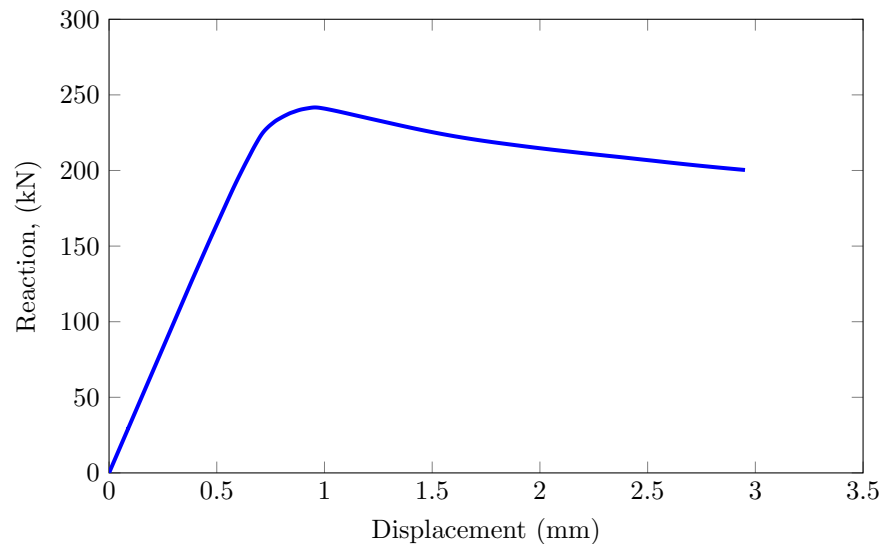


Figure 3.15. Displacement-reaction diagram

Additionally, fig. 3.16 includes the states of the plastic-damage variable and the cohesion of the material corresponding to the last step of the incremental analysis, respectively. Again, in these figures it is possible to observe the direct influence that the plastic-damage variable has on the degradation of the cohesion of the material.

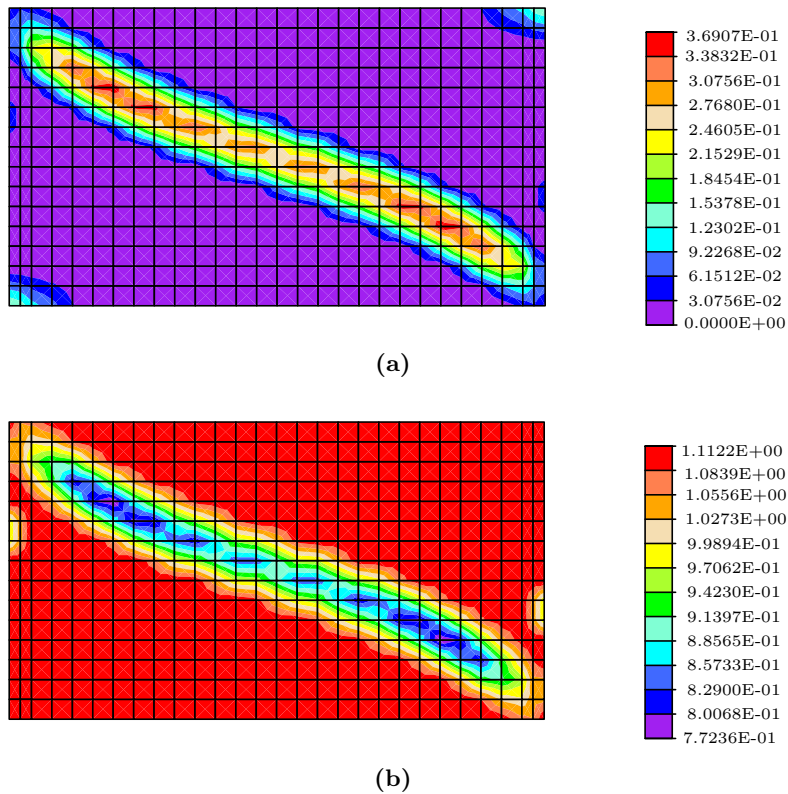


Figure 3.16. State of the internal variables at the end of the analysis: (a) plastic-damage variable and (b) cohesion

3.6 Validation (macro-models)

In this research, the use of macro-models is of special interest because the main objective is to reduce the computational cost of the non-linear analysis of massive masonry structures. According to Lourenço (1996), the field of application of macro-models is necessarily in large structures, subjected to boundary conditions and loads in such a way that the global behaviour of the structure is not governed by the local behaviour of the masonry.

Due to the difficulty and high economical cost of testing large specimens, most experiments available in the literature are small in size (Lourenço, 1996). For this type of experiments, a macro-modelling strategy is not suitable and the constituent materials of the masonry must be discretized independently, *i.e.*, micro-modeled.

For this reason, an experiment was selected from a series of tests conducted at the Federal Institute of Technology in Zurich (ETH Zurich), reported in the works of Lurati and Thürlimann (1990) and Lurati et al. (1990) (fig. 3.17). Because of their size, these real-scale experiments are suitable for the validation of macro-models. Additionally, there are enough reported parameters for the application of the plastic-damage constitutive model.

The geometry of the specimen is shown in fig. 3.18. This specimen consists of a masonry wall of $3600 \times 2000 \times 150 \text{ mm}^3$ and two columns of $150 \times 2000 \times 600 \text{ mm}^3$. Also, there is a concrete slab at the top and another one at the bottom of the wall. As usual, the specimen was initially subjected to vertical loads and then to lateral ones.



Figure 3.17. Experiment of masonry wall conducted at Federal Institute of Technology in Zurich (ETH Zurich) (Lourenço, 1996)

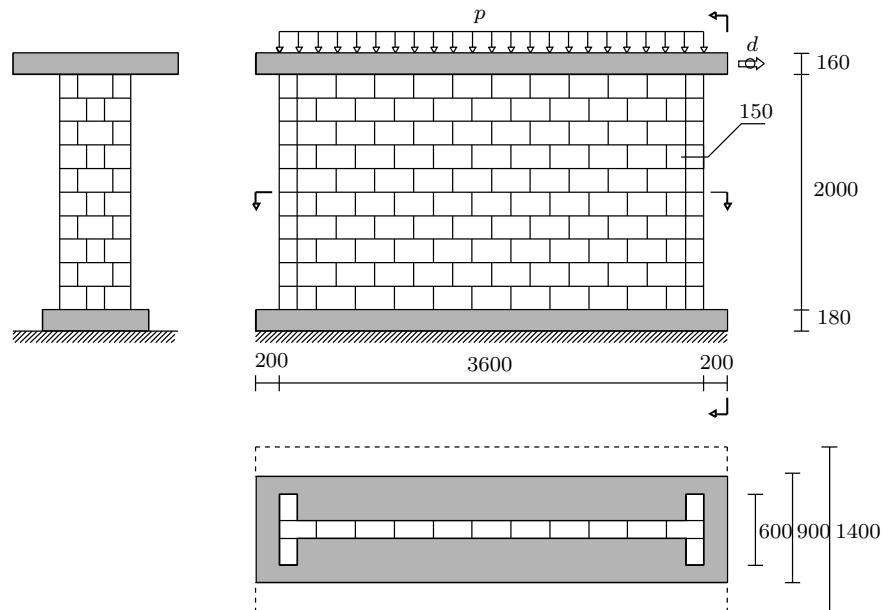


Figure 3.18. Geometry of the specimen (dimensions in mm) (Lourenço, 1996)

The first set of experiments were conducted by Ganz and Thürlimann (1984). The selected wall, called *W1* in the published report, was previously subjected to a vertical load $P = 415 \text{ kN}$ and then to lateral loads. This *W1* wall shows a very ductile behaviour. The reported mechanical properties of the experiment are included in the table 3.2. Additionally, a shear modulus of $G_{yx} = 1130 \text{ MPa}$ were considered.

3. NON-LINEAR BEHAVIOUR OF MASONRY

Table 3.2. Mechanical parameters reported for the masonry wall

Elasticity modulus	Poisson's ratio	Compressive strength	Tensile strength
$E_x = 2460$ MPa	$\nu_{xy} = 0.20$	$\sigma_{c_x} = 1.87$ Mpa	$\sigma_{t_x} = 0.28$ MPa
$E_y = 5460$ MPa	$\nu_{xy} = 0.20$	$\sigma_{c_y} = 7.61$ Mpa	$\sigma_{t_y} = 0.005$ MPa

In this section, no homogenization technique was employed, so all mechanical properties used in the analysis were averaged without any specific criteria. In the section 3.8.2.1 this wall is analyzed employing a homogenization technique. A mesh with 420 4-node quadrilateral finite elements was built and analyzed through the SRI scheme. To simulate the conditions of the experiment, all the upper nodes are vertically restrained. In a first step, vertical displacements equivalent to the initial vertical load P were imposed. In a second step, lateral displacements were imposed. The reaction-displacement diagram resulting from the analysis is shown in fig. 3.19.

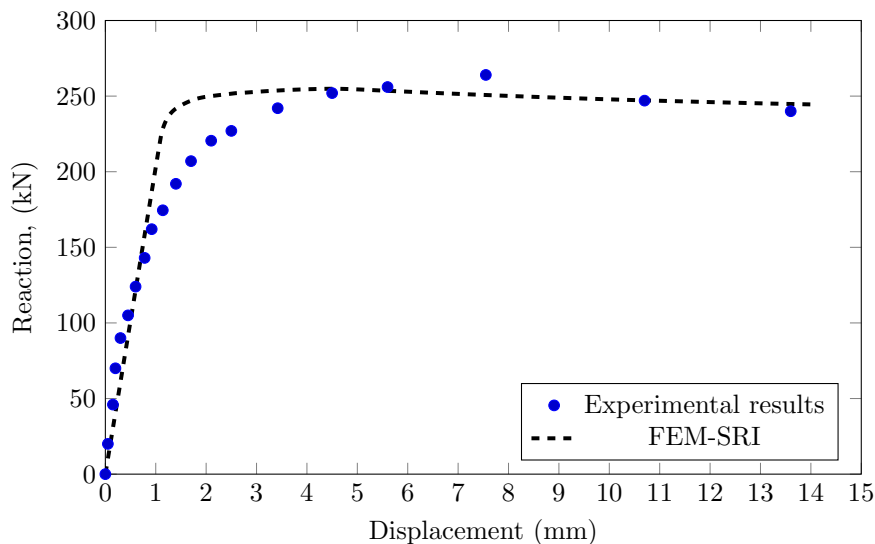


Figure 3.19. Displacement-reaction diagram of the $W1$ wall

It can be observed that the numerically approximated behaviour is similar to the one reported for the experiment. However, it can be noticed that the ascending elastic branch is not well reproduced, which suggests the need to consider a homogenization criterion of elastic parameters. Also, it can be noted that the gradual yielding is not well reproduced in the numerical approximation. Although this experiment does not have a behaviour that allows the evaluation of the most attractive characteristics of the implemented model, such as the degradation of the cohesion, it worked for the debugging process of the coded algorithms. Additionally, the distribution of the so-called Von Mises principal stress at the end of the analysis is included in fig. 3.20, which is comparable to that reported in the experiments (fig. 3.21).

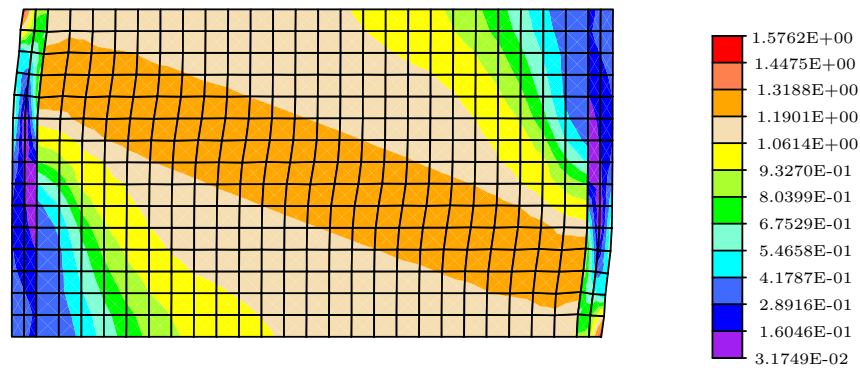


Figure 3.20. Distribution of Von Mises stress at the end of the analysis

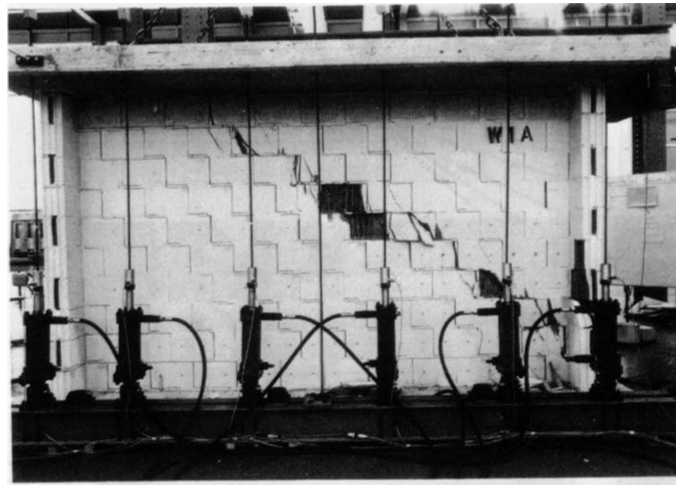


Figure 3.21. Damage patterns at the end of the experiment (Lourenço, 1996)

3.7 Homogenization

In this section, the homogenization strategy that was selected, from the academic literature, to be implemented within the *FEAP* program (Taylor, 2017) is briefly described. This implementation was performed in this program so that it can be applied through the plastic-damage constitutive model and the SRI scheme proposed in this work. Thus, the complete strategy allows the use of macro-models to economize computationally the non-linear analysis of massive masonry structures.

In order to have a controlled debugging process, this implementation was performed in two stages. In the first one, the homogenization of elastic parameters of the masonry was implemented, completely ignoring the directions of plastic flow of the masonry as a homogenized material. In a second stage, the complete strategy was implemented, which includes a homogenized plastic flow.

3.7.1 Elastic parameters

López et al. (1999) proposed a homogenized model such that its properties intrinsically contain both geometrical and mechanical properties of the masonry structure from the basic definition of the constituent materials, *i.e.*, units and mortar.

This model is based on a detailed analysis of the deformation modes of a basic cell which represents a portion of the usual organized masonry arrangement. López et al. (1999) highlights two hypotheses that are taken as valid: (i) the height and width dimensions are large in relation to the thickness of the structural element, ensuring the validity of the hypothesis of the plane stress of the structure; (ii) the hypothesis of orthotropy of the masonry is taken as valid. The basic masonry cell used by López et al. (1999) is shown in fig. 3.22.

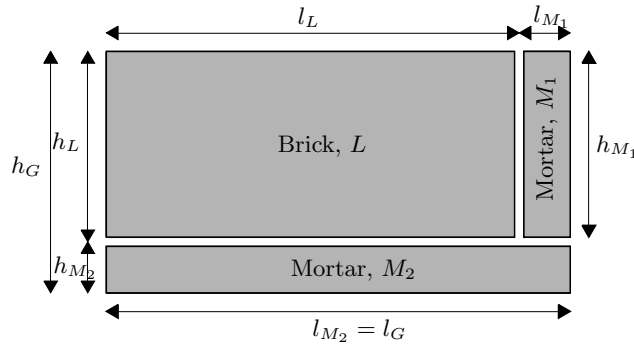


Figure 3.22. Basic masonry cell used for homogenization (López et al., 1998)

In this figure, and hereinafter, the indexes L , M_1 , M_2 and G are associated to the brick, mortar in the vertical direction, mortar in the horizontal direction and to the global measures of the basic cell already homogenized, respectively. In addition, l is related to horizontal lengths, h to vertical lengths and t to thickness.

Four deformation modes are proposed for the geometrical arrangement of the basic unit:

- *Mode 1.* Tension-compression on the x axis
- *Mode 2.* Tension-compression on the y axis
- *Mode 3.* Shear stress on the xy plane
- *Mode 4.* Deformation field out of the xy plane

Given the acceptance of the plane-stress hypothesis, the out-of-plane xy deformations are exclusively owing to deformations produced by the Poisson's effect (López et al., 1999). In the following lines, the some of the expressions for computing the homogenized mechanical parameters derived by López et al. (1999) are included as reference.

3.7.1.1 Elasticity modulus

The expressions to compute the elasticity modulus in x , y and z directions are included in eqs. 3.16, 3.19 and 3.21, respectively.

$${}^x E_G = \frac{1}{{}^x B_L {}^x D} \quad (3.16)$$

where:

$${}^x D = \frac{l_L}{{}^x E_L l_G} + \frac{l_{M_1}}{{}^x E_{M_1} l_G} \quad {}^x B_L = \frac{{}^x A_L l_{M_2} h_G}{{}^x E_{M_2} h_{M_2}} \quad (3.17)$$

$${}^x A_L = \frac{{}^x E_L {}^x E_{M_1} {}^x E_{M_2} h_{M_1}}{{}^x E_{M_1} {}^x E_{M_2} h_{M_2} l_L + {}^x E_L {}^x E_{M_2} h_{M_2} l_{M_1} + {}^x E_L {}^x E_{M_1} h_L l_{M_2}} \quad (3.18)$$

$${}^y E_G = \frac{1}{{}^y B_L h_L + \frac{h_{M_2}}{{}^y E_L h_G} + \frac{h_{M_2}}{{}^y E_{M_2} h_G}} \quad (3.19)$$

where:

$${}^y B_L = \frac{{}^y A_L l_G h_{M_1}}{{}^y E_{M_1} h_{M_1}} \quad {}^y A_L = \frac{{}^y E_L {}^y E_{M_1} l_{M_1}}{{}^x E_{M_1} l_{M_1} h_L + {}^x E_L l_L h_{M_1}} \quad (3.20)$$

$${}^z E_G = \frac{1}{{}^z B_L {}^z D} \quad (3.21)$$

where:

$${}^z D = \frac{t_L}{{}^z E_L t_G} + \frac{l_{M_1}}{{}^z E_{M_1} l_G} \quad {}^z B_L = \frac{{}^z A_L t_{M_2} h_G}{{}^z E_{M_2} h_{M_2}} \quad (3.22)$$

$${}^z A_L = \frac{{}^x E_L {}^x E_{M_1} {}^x E_{M_2} h_{M_1}}{{}^x E_{M_1} {}^x E_{M_2} h_{M_2} t_L + {}^x E_L {}^x E_{M_2} h_{M_2} t_{M_3} + {}^x E_L {}^x E_{M_1} h_L t_{M_2}} \quad (3.23)$$

3.7.1.2 Shear modulus

The shear modulus are described by the planes xy , yx , xz , zx , zy and yz in the eqs. 3.24, 3.26, 3.28, 3.30, 3.32 and 3.34, respectively.

$${}^{xy} G_G = \frac{1}{{}^{xy} A_L h_L + \frac{h_{M_2}}{{}^{xy} G_L h_G} + \frac{h_{M_2}}{{}^{xy} G_{M_2} h_G}} \quad (3.24)$$

where:

$${}^{xy} A_L = \frac{{}^{xy} G_L l_G}{{}^{xy} G_L l_L + {}^{xy} G_{M_1} l_{M_1}} \quad (3.25)$$

$${}^{yx} G_G = \frac{1}{{}^{yx} A_L l_L + \frac{l_{M_2}}{{}^{yx} G_L l_G} + \frac{l_{M_2}}{{}^{yx} G_{M_2} l_G}} \quad (3.26)$$

3. NON-LINEAR BEHAVIOUR OF MASONRY

where:

$${}_{yx}A_L = \frac{{}_{xy}G_L h_G}{{}_{xy}G_L h_L + {}_{xy}G_{M_1} h_{M_2}} \quad (3.27)$$

$${}_{xz}G_G = \frac{1}{\frac{{}_{xz}A_L t_L}{{}_{xz}G_L t_G} + \frac{t_{M_3}}{{}_{xz}G_{M_3} t_G}} \quad (3.28)$$

where:

$${}_{xz}A_L = \frac{{}_{xz}G_L l_G}{{}_{xz}G_L l_L + {}_{xz}G_{M_1} l_{M_1}} \quad (3.29)$$

$${}_{zx}G_G = \frac{1}{\frac{{}_{zx}A_L l_L}{{}_{zx}G_L l_G} + \frac{l_{M_1}}{{}_{zx}G_{M_1} l_G}} \quad (3.30)$$

where:

$${}_{zx}A_L = \frac{{}_{zx}G_L t_G}{{}_{zx}G_L t_L + {}_{zx}G_{M_3} t_{M_3}} \quad (3.31)$$

$${}_{zy}G_G = \frac{1}{\frac{{}_{zy}A_L h_L}{{}_{zy}G_L h_G} + \frac{h_{M_2}}{{}_{zy}G_{M_2} h_G}} \quad (3.32)$$

where:

$${}_{zy}A_L = \frac{{}_{zy}G_L t_G}{{}_{zy}G_L t_L + {}_{zy}G_{M_3} t_{M_3}} \quad (3.33)$$

$${}_{yz}G_G = \frac{1}{\frac{{}_{yz}A_L t_L}{{}_{yz}G_L t_G} + \frac{t_{M_3}}{{}_{yz}G_{M_3} t_G}} \quad (3.34)$$

where:

$${}_{yz}A_L = \frac{{}_{yz}G_L h_G}{{}_{yz}G_L h_L + {}_{yz}G_{M_3} t_{M_2}} \quad (3.35)$$

3.7.1.3 Poisson's ratio

The poisson's ratio in the corresponding directions can be summarized in the following expression:

$${}_{ij}\nu_G = \frac{2 {}_{ij}G_G}{\sqrt{{}_i E_G {}_j E_G}} - 1 \quad (3.36)$$

where i and j are the directions on the x , y and z axes. Thus, substituting the following equations are obtained:

$${}_{xy}\nu_G = \frac{2 {}_{xy}G_G}{\sqrt{{}_x E_G {}_y E_G}} - 1 \quad {}_{yx}\nu_G = \frac{2 {}_{yx}G_G}{\sqrt{{}_y E_G {}_x E_G}} - 1 \quad (3.37)$$

$$x_z\nu_G = \frac{2_{xz}G_G}{\sqrt{x}E_G zE_G} - 1 \quad z_x\nu_G = \frac{2_{zx}G_G}{\sqrt{z}E_G xE_G} - 1 \quad (3.38)$$

$$y_z\nu_G = \frac{2_{yz}G_G}{\sqrt{y}E_G zE_G} - 1 \quad z_y\nu_G = \frac{2_{zy}G_G}{\sqrt{z}E_G yE_G} - 1 \quad (3.39)$$

3.7.2 Numerical implementation

This strategy was implemented in the *FEAP* program (Taylor, 2017), within the same routine of the plastic-damage constitutive model. Special attention was taken in the compatibility of this implementation with the algorithms already programmed, *i.e.*, the algorithms for the plastic-damage constitutive mode and the SRI scheme. For this purpose, a new subroutine was added which function is to create the homogenized elastic constitutive matrix, using the expressions derived by López et al. (1999).

Options were attached within the coded algorithm for the selection of schemes according to the number of known mechanical parameters of the constituent materials of the masonry, *e.g.*, mechanical parameters already homogenized or parameters independent for each constituent material (fig. 3.23).

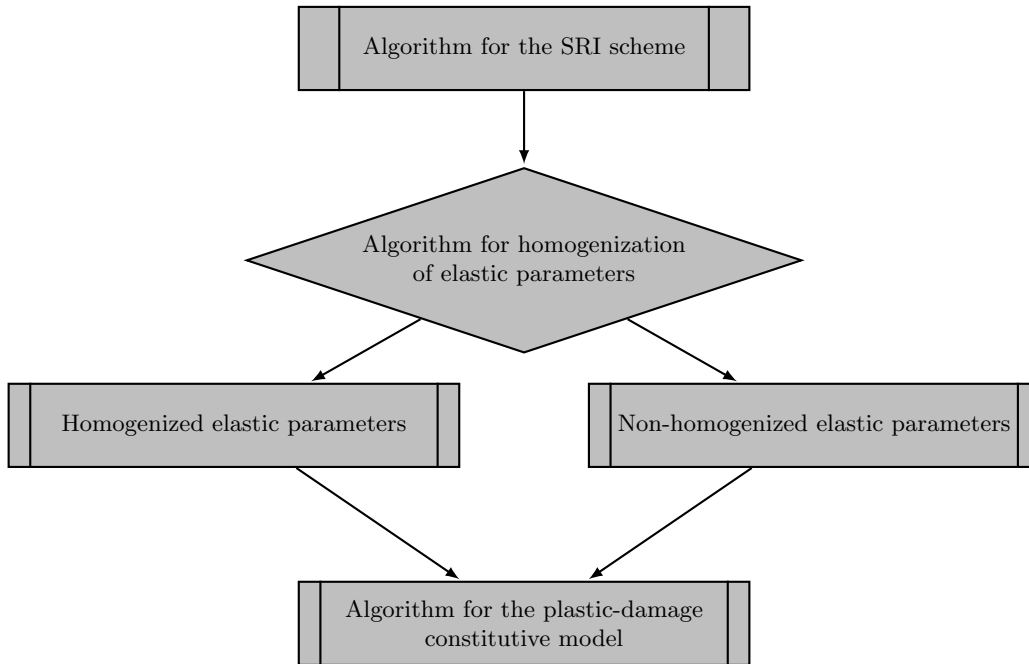


Figure 3.23. Flow diagram of the algorithms implemented in *FEAP* (Taylor, 2017)

3.7.2.1 Debugging test

The same set of experiments used in section 3.6 that were carried out at the Federal Institute of Technology in Zurich (ETH Zurich), see Lurati and Thürlimann (1990) and

3. NON-LINEAR BEHAVIOUR OF MASONRY

Lurati et al. (1990) (fig. 3.17), were selected for testing the coded algorithm. Also, the same mesh, employed in the section 3.6, composed of 420 4-node quadrilateral finite elements was used. In this analysis, the variation of the mechanical elastic parameters of the masonry according to the x and y directions, is considered by means of the implemented homogenization criterion. The mechanical parameters are included in table 3.2.

As mentioned above, at this stage, only the elastic parameters were homogenized. Therefore, in this example, a large enough values of tensile and compressive strengths were assigned to prevent the masonry from entering in its non-linear range, since the the main interest is to evaluate the quality in the approximation of the upward elastic branch. The reaction-displacement diagram obtained by the mentioned analysis is shown in fig. 3.24. Here, it can be seen that the upward elastic branch of the experimental results is adequately approached.

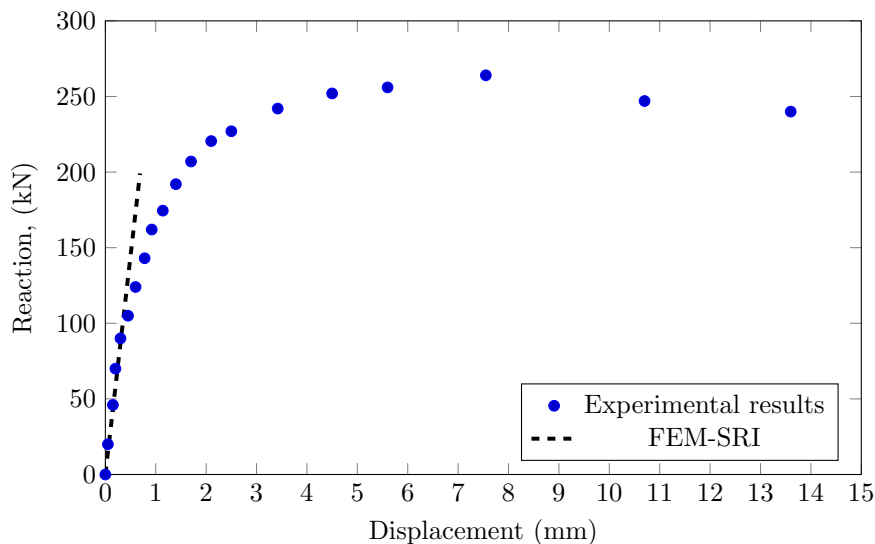


Figure 3.24. Displacement-reaction diagram of the $W1$ wall

3.8 Homogenized plastic flow

For studying the orthotropic behaviour of masonry, once the elastic limit, defined by a yield function developed for isotropic materials, is exceeded, López et al. (1999) proposed a strategy based on the Theory of the Mapped Spaces. With this theory, the existence of an orthotropic space (real) and an isotropic space (fictitious), in which the evolution of the yield surface is carried out during the analysis, is assumed. This strategy allows the possibility for employing yield functions originally developed for isotropic materials in the study of orthotropic ones by applying linear transformations (fig. 3.25).

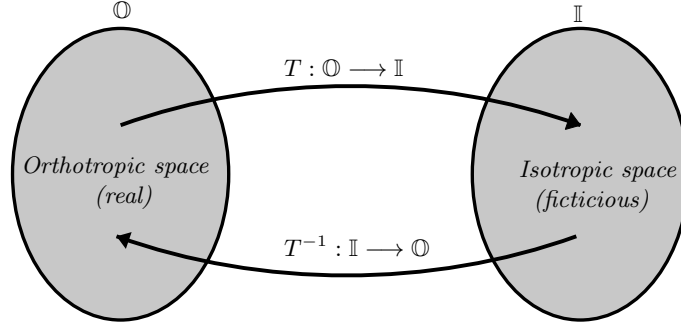


Figure 3.25. Schematic representation of the linear transformation for the isotropic and orthotropic spaces

3.8.1 Transformation spaces

As reference, some of the expressions to transform the different components of plastic deformation from isotropic space to the orthotropic one are included (López et al., 1999). Equations 3.40, 3.42 and 3.44 are derived for the x , y and z directions, respectively. Also, the eq. 3.45 allows the xy -plane transformation.

$${}_x\varepsilon_G^p = \left[A_x^p l_{M_2} + \left(\frac{1}{l_g} - A_x^p \right) (l_L + l_{M_1}) \right] {}_x\varepsilon_G^p \Big|_{\text{Mohr}} \quad (3.40)$$

where:

$$A_x^p = \frac{{}_x E_L {}_x E_{M_1} {}_x E_{M_2} h_{M_2}}{{}_x E_{M_1} {}_x E_{M_2} h_{M_2} l_L + {}_x E_L {}_x E_{M_2} h_{M_2} l_{M_1} + {}_x E_L {}_x E_{M_1} h_L l_{M_1}} \left(\frac{l_L}{{}_x E_L l_G} + \frac{l_{M_1}}{{}_x E_{M_1} l_G} \right) \quad (3.41)$$

$${}_y\varepsilon_G^p = \left[A_y^p h_{M_1} + \left(\frac{1}{h_G} - A_y^p \right) h_L + \frac{h_{M_2}}{h_G} \right] {}_y\varepsilon_G^p \Big|_{\text{Mohr}} \quad (3.42)$$

where:

$$A_y^p = \frac{{}_y E_L {}_y E_{M_1} l_{M_1}}{{}_y E_{M_1} l_{M_1} h_L + {}_y E_L l_L h_{M_1}} \frac{h_L}{{}_y E_L h_G} \quad (3.43)$$

$${}_z\varepsilon_G^p = \frac{({}_{xz}\nu_G + {}_{xy}\nu_G {}_{yz}\nu_G) {}_x\varepsilon_G^p \Big|_{\text{Mohr}} + ({}_{yz}\nu_G + {}_{xz}\nu_G {}_{yx}\nu_G) {}_y\varepsilon_G^p \Big|_{\text{Mohr}}}{-1 + {}_{xy}\nu_G {}_{yx}\nu_G} \quad (3.44)$$

$${}_{xy}\gamma_G^p = \left(\frac{h_L + h_{M_2}}{h_G} \right) {}_{xy}\gamma_G^p \Big|_{\text{Mohr}} \quad (3.45)$$

where:

$$A_{\gamma}^p = G_{M_1} \frac{l_{M_1}}{l_G} \left(\frac{G_L l_G}{G_L l_L + G_{M_1} l_{M_1}} \right) \frac{h_L}{G_L h_G} \quad (3.46)$$

3.8.2 Numerical implementation

As in the previous stage, this strategy was implemented in the *FEAP* program (Taylor, 2017), within the same routine of the plastic-damage constitutive model. As in the case of homogenization of elastic parameters, special care was taken in the compatibility of this implementation with the algorithm already programmed for the constitutive model. For this purpose, the previously created subroutine was extended so that, in addition to building the homogenized elastic constitutive matrix, the transformation of the fictitious isotropic space to the real orthotropic space was carried out (fig. 3.26).

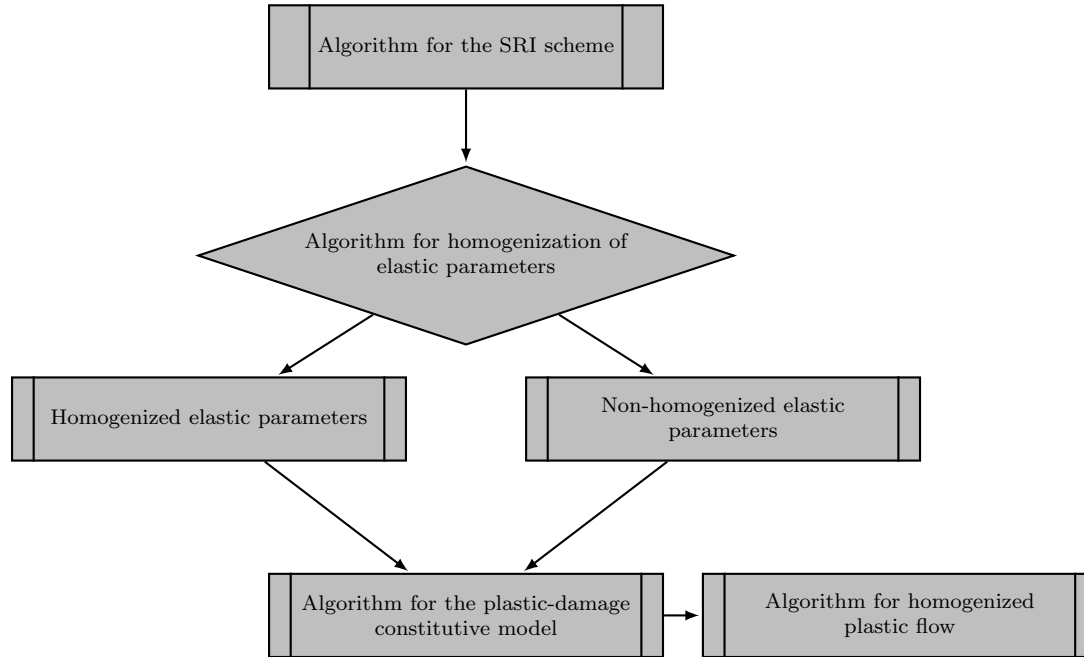


Figure 3.26. Flow diagram of the algorithms implemented in *FEAP* (Taylor, 2017)

3.8.2.1 Debugging tests

The set of experiments carried out at the Federal Institute of Technology in Zurich (ETH Zurich) by Lurati and Thürlimann (1990) and Lurati et al. (1990) (fig. 3.17), were used again in this section. The mechanical properties are summarized in table 3.2. In fig. 3.27, the numerically approximated reaction-displacement diagram is shown and compared to the experimental results. From this figure, some important observations can be made. First, similar behaviour is observed between the two curves. Second, there is still a weak approximation in the gradual yield that occurs in the experiment in comparison to the numerically approximated yield. Third, it can be concluded that the experiment is not the

most accurate to highlight the main attractiveness of the model, such as the degradation of mechanical parameters. Additionally, in the fig. 3.28, the distribution of the principal strains is included. These results are comparable to those ones of the experiment (see fig. 3.21).

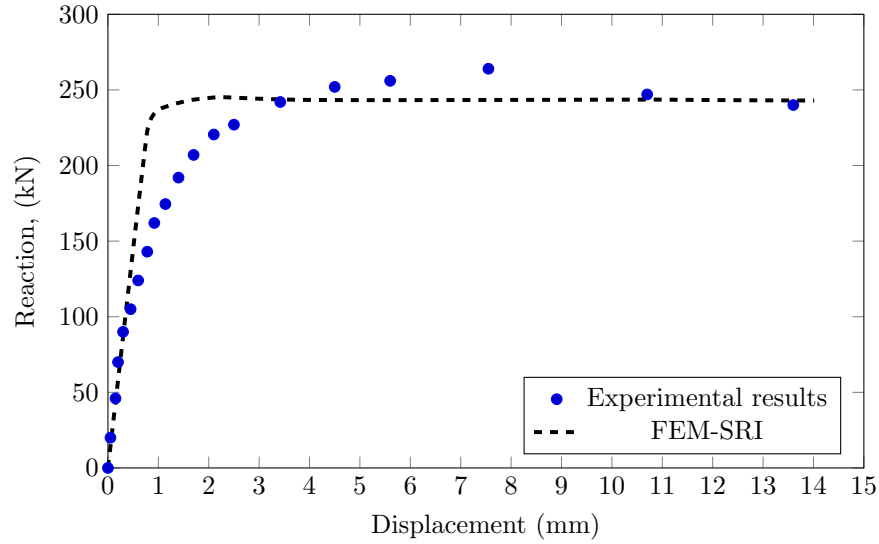


Figure 3.27. Displacement-reaction diagram of the W1 wall

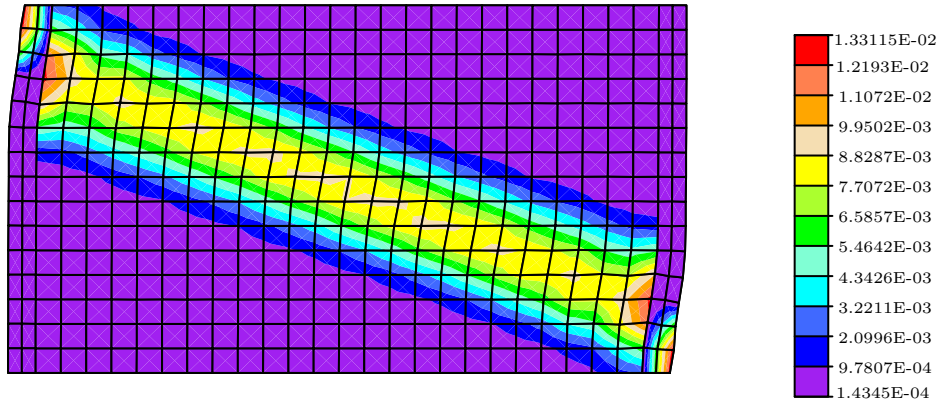


Figure 3.28. Distribution of principal strains at the end of the analysis

Application through a plastic-damage constitutive model

4.1 Introduction

In this chapter, two validation examples of the complete proposal of this thesis are included. Two types of walls were selected from the set of experiments carried out at the Eindhoven University of Technology (TU Eindhoven).

In these examples, the numerical implementations performed in the program *FEAP* (Taylor, 2017) and described in the chapters 2 and 3, *i.e.* the SRI scheme, the plastic-damage constitutive model (Oller, 2001) and the homogenization technique (López et al., 1999), were used.

In each of the following sections, a description of the experiment and the construction of the numerical model, in order to approximate the obtained experimental results, is included. Additionally, the results are widely discussed.

4.2 Shear walls (TU Eindhoven)

A series of tests on shear walls carried out by Raijmakers and Vermeltoort (1992) and Vermeltoort and Raijmakers (1993), at the Eindhoven University of Technology (TU Eindhoven), were selected. In their experiments, shear walls with and without openings were considered. In this dissertation, both types of walls were analyzed. This experiment was selected because of its relevance, since these experimental results are widely used in the literature for validation and calibration of numerical models, *e.g.*, the works of Lourenço (1996), Pelà et al. (2013), Quinteros et al. (2014), Milani and Bertolesi (2017) and Zucchini and Lourenço (2009). Also, in the work of Pari et al. (2021) these series of tests were employed to illustrate the application of a proposal of an interface model for sequentially linear analysis.

4.2.1 Shear walls without openings

Initially, the case of shear walls without openings (named J4D, J5D, J6D and J7D) was studied. These walls were 990 mm wide and 1000 mm high. They were built with 16 active brick courses and two additional courses clamped in steel beams 70 mm high, as depicted in fig. 4.1. The bricks were made of solid clay with dimensions of $210 \times 52 \times 100$ mm and joined with 10 mm mortar layers. These specimens were tested for different pre-compression loads before starting the application of lateral displacements, δ , in a monotonic increasing manner. The corresponding pre-compression loads were $p = 30$ kN for J4D and J5D walls, $p = 120$ kN for J6D wall and $p = 210$ kN for J7D wall (Lourenço, 1996; Quinteros et al., 2014). In fig. 4.1 both the geometry of the walls and the steps of the test are shown.

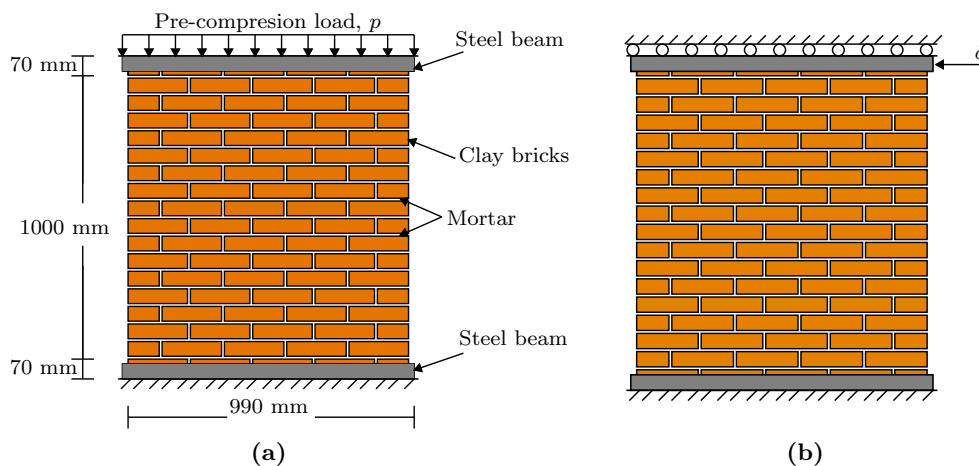


Figure 4.1. Analysis steps of the shear wall without openings (JD) of TU Eindhoven: (a) pre-compression loads and (b) lateral displacement

The mechanical properties of the materials used in the construction of these walls are described in detail in the works of Raijmakers and Vermeltoort (1992) and Vermeltoort and Raijmakers (1993) and summarized by Lourenço (1996). The mechanical parameters are included in table 4.1 for the bricks and in table 4.2 for the mortar joints. Additionally to these parameters, an initial cohesion of $c = 1.4\sigma_t$, an angle of internal friction $\phi = 36.9^\circ$ and an angle of dilatancy $\psi = 0^\circ$ were considered for the analysis.

Table 4.1. Mechanical parameters for the bricks considered in the analysis

Elasticity modulus	Poisson's ratio	Tensile strength	Fracture energy
$E = 16700$ MPa	$\nu = 0.15$	$\sigma_t = 2.0$ MPa	$G_f^I = 0.08$ N mm/mm ²

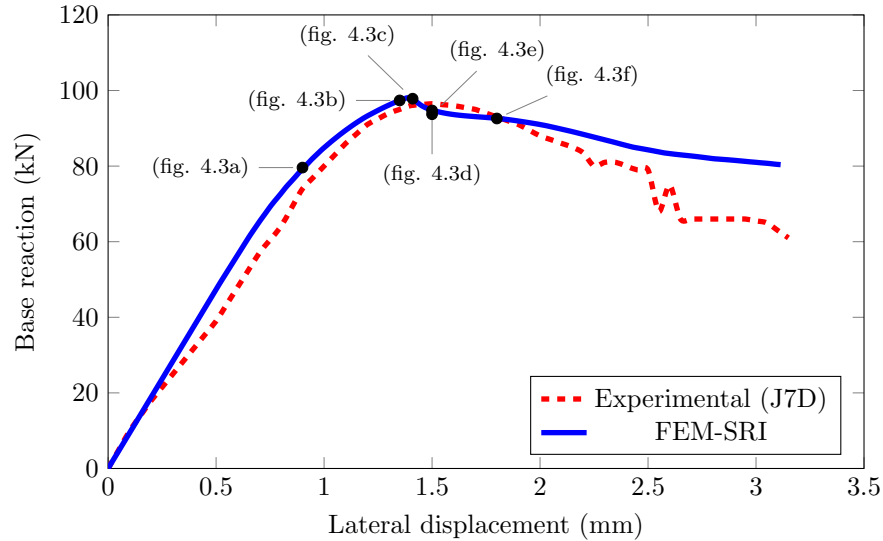
For the numerical model, in order to select the appropriate mesh density, a convergence analysis was performed. The resulting mesh was composed of 676 4-node quadrilateral elements arranged in a structured manner. The SRI scheme within the homogenized plastic-damage constitutive model, described in the previous chapter, was used. As in the experiment, the analysis of the numerical model consisted of two steps. In the first step, a pre-compression load of $p = 210$ kN (corresponding to the J7D wall) was applied, and

Table 4.2. Mechanical parameters for the mortar joints considered in the analysis

Elasticity modulus, E (MPa)	Poisson's ratio ν	Tensile strength, σ_t (MPa)	Fracture energy, G_f^I (N mm/mm ²)	Compressive strength, σ_c (MPa)	Fracture energy, G_f^{II} (N mm/mm ²)
0.80	0.15	0.25	0.018	0.16	2.8
1.00		0.16	0.012	0.16	
0.80		0.16	0.012	0.16	

in the second step the increasing monotonic displacements, δ , were applied (fig. 4.1).

Figure 4.2 includes the comparison of the reaction-displacement curve obtained in the numerical analysis described in the previous paragraphs against the experimental results of the J7D wall. From this comparison, it may be observed that the general behaviour of both curves is similar. A difference is appreciated in a part of the elastic branch that has been found in other numerical approximations such as that of Lourenço (1996). Also, it is observed that the magnitude of the highest base reaction is quite similar, however, it is identified that there is a small difference in the displacement in which it occurs. Additionally, in the numerically approximated curve of fig. 4.2 are indicated six intermediate states of the analysis which were selected to show the evolution of the plastic-damage variable during the analysis (figs. 4.3a to 4.3f).

**Figure 4.2.** Reaction-displacement experimental and numerical curves of the J7D wall

Finally, fig. 4.4 contains both the state of the plastic-damage variable and the state of the cohesion at the end of the numerical analysis. As it may be seen, the analysis approximates reasonably well the state of the J7D wall at the end of the experiment reported in Raijmakers and Vermeltoort (1992) and Vermeltoort and Raijmakers (1993) (fig. 4.5).

4. APPLICATION THROUGH A PLASTIC-DAMAGE CONSTITUTIVE MODEL

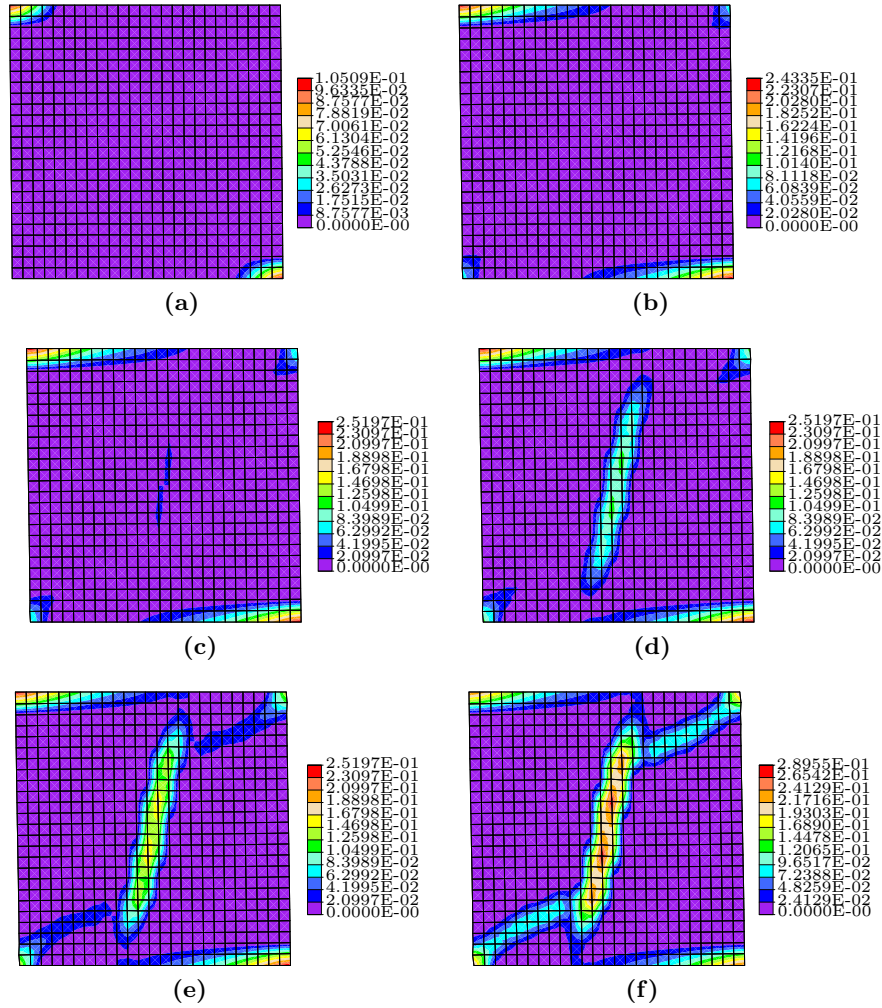


Figure 4.3. Six intermediate analysis states of the plastic-damage variable at (a) 0.9 mm, (b) 1.35 mm, (c) 1.41 mm, (d) 1.50 mm, (e) 1.59 mm and (f) 1.80 mm

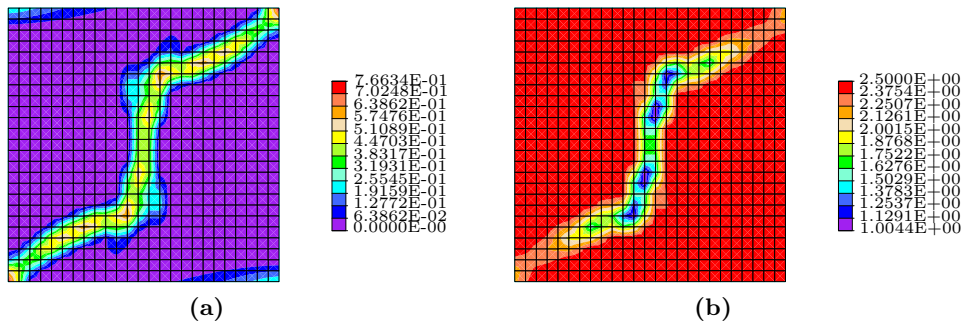


Figure 4.4. Final state of the constitutive model internal variables: (a) plastic-damage and (b) cohesion

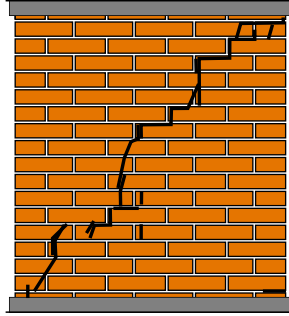


Figure 4.5. Cracks observed at the end of the experiment on the wall J7D (Lourenço, 1996)

4.2.2 Shear walls with opening

Subsequently, the experimental results of the test of the shear wall with an opening (named J2G and J3G) were used. These walls were subjected to a pre-compression load of $p = 30$ kN. The geometry and location of the opening is shown in fig. 4.6. In this figure, it can be seen that the opening is located from the seventh to the thirteenth row of bricks. The mechanical properties of the constituent materials were the same as the shear wall without openings (Raijmakers and Vermeltoort, 1992; Vermeltoort and Raijmakers, 1993) (tables 4.1 and 4.2).

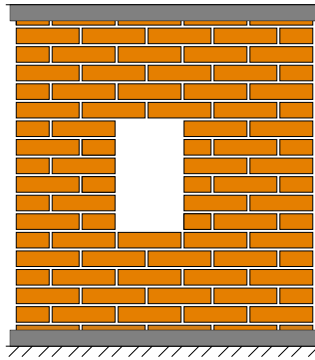


Figure 4.6. Geometry of the shear wall with openings of the TU Eindhoven

For the numerical model, as in the previous example, in order to select an appropriate mesh density, a convergence analysis was performed. The resulting mesh was composed of 800 4-node quadrilateral elements arranged in a structured manner. To simulate the non-linear behaviour of the masonry, the same homogenized plastic-damage model was used. As in the previous case, the analysis was performed in two steps. In the first one, the pre-compression load was applied ($p = 30$ kN) and in the second one the lateral displacements were imposed.

Figure 4.7 includes the comparison of the reaction-displacement curves obtained from the numerical analysis, as described in the previous paragraphs, against the experimentally

obtained curves for the J2G and J3G walls. Furthermore, the numerical approximation of this curve obtained by Pelà et al. (2013) was added for comparison purposes. Furthermore, six intermediate states of the analysis were selected to show the evolution of the plastic-damage variable (figs. 4.8a to 4.8f).

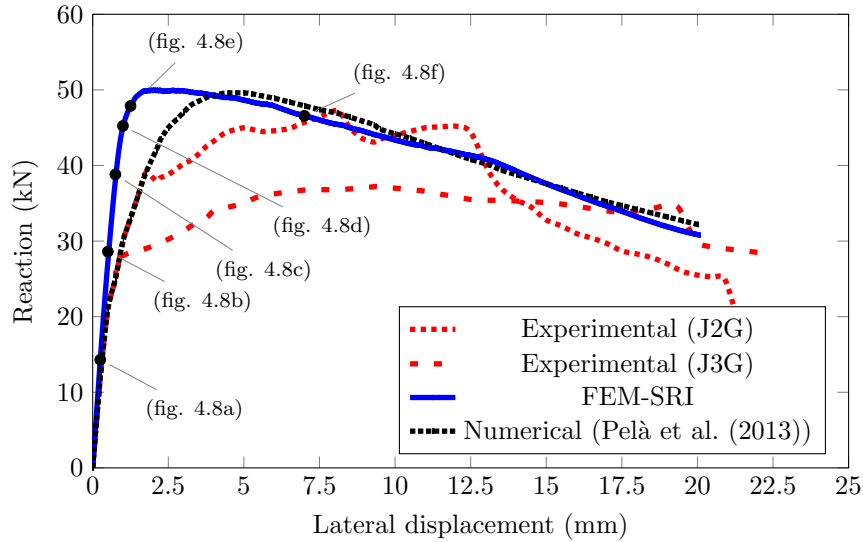


Figure 4.7. Reaction-displacement experimental and numerical curves of the J2G and J3G walls

From this figure, several observations can be made. First, it may be seen that, although both walls (J2G and J3G) were tested under the same conditions, their results are not entirely consistent, especially regarding the highest and ultimate reactions. Second, in the sources consulted in which the results of these experiments are numerically simulated (Lourenço, 1996; Milani and Bertolesi, 2017; Pelà et al., 2013; Quinteros et al., 2014), it was found that all these numerical approximations, including the one corresponding to the present work, were similar to the behaviour of the J2G specimen. Third, the approximated curve in this work coincides quite well with the one approximated by Pelà et al. (2013). Fourth, an important difference can be seen in the post-yielding zone, since in the experiment a change in the slope may be appreciated, while this is not the case in the numerical approximation.

Finally, in fig. 4.9 are included both the state of the plastic-damage variable and the state of the cohesion at the end of the numerical analysis. It can be seen that the analysis approximates the state of the J2G and J3G walls at the end of the experiment (Raijmakers and Vermeltoort, 1992; Vermeltoort and Raijmakers, 1993) (fig 4.10).

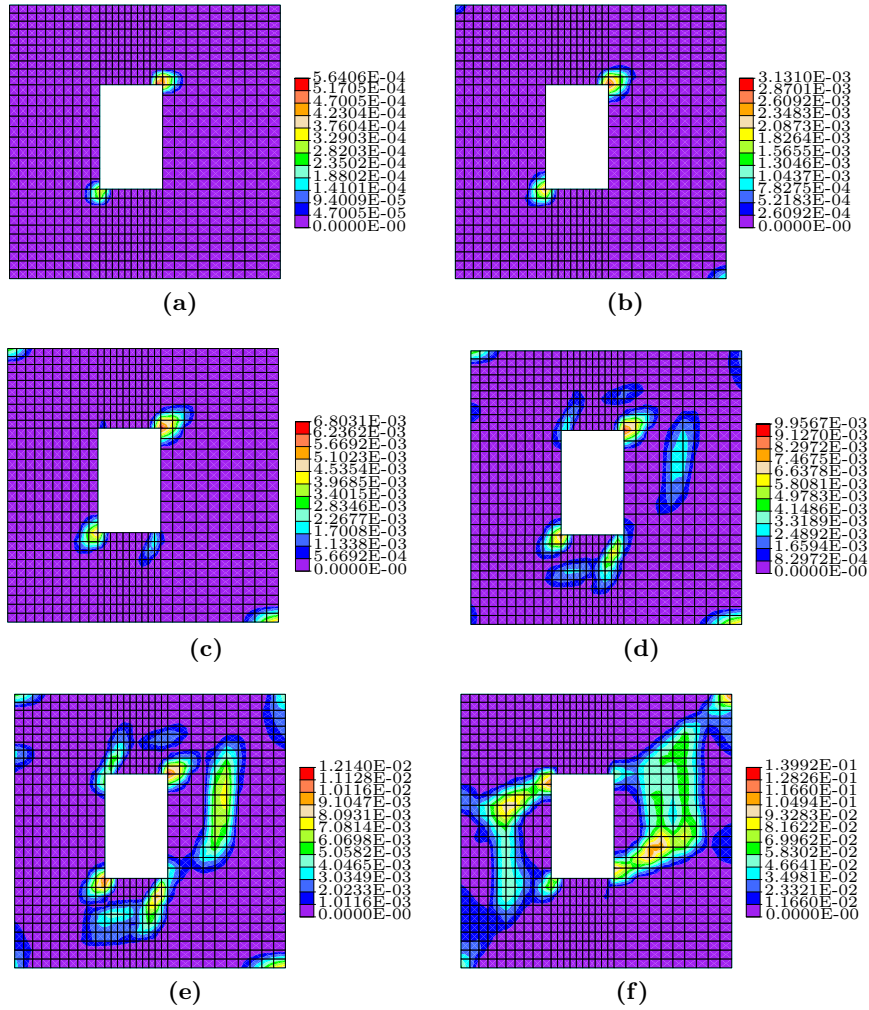


Figure 4.8. Six intermediate analysis states of the plastic-damage variable at (a) 0.25 mm, (b) 0.50 mm, (c) 0.75 mm, (d) 1.00 mm, (e) 1.25 mm and (f) 7.00 mm

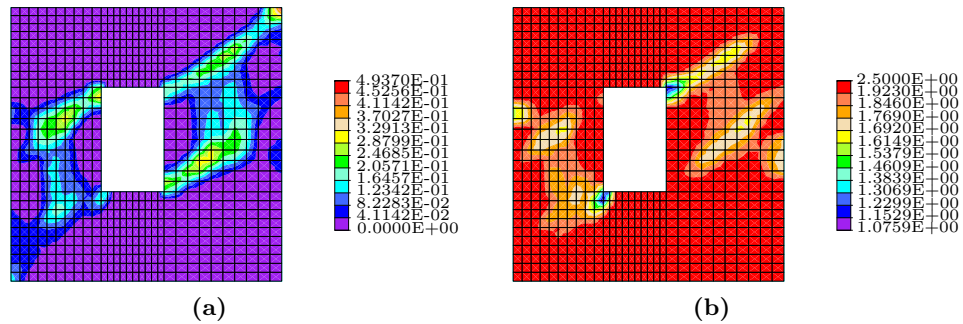


Figure 4.9. Final state of the constitutive model internal variables: (a) plastic-damage and (b) cohesion

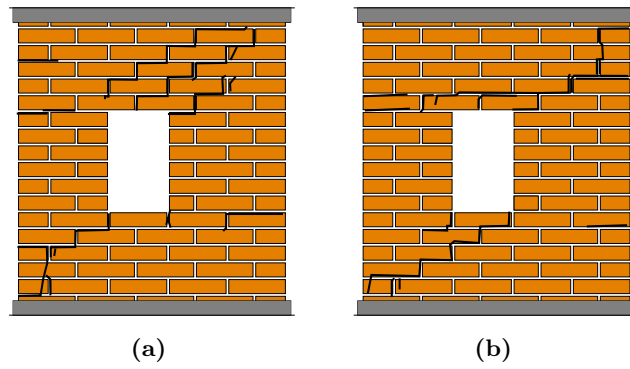


Figure 4.10. Cracks observed at the end of the experiment on the walls (a) J2G and (b) J3G (Lourenço, 1996)

Application through sequentially linear analysis

5.1 Introduction

As an alternative for applying the SRI scheme proposed in this dissertation, this chapter describes a method based on sequentially linear analysis (SLA) with saw-tooth softening, proposed by Rots (2001b and 2004), and applied to the study of masonry constructions. This method consists on the execution of multiple linear analysis of the same structure with sequentially degraded mechanical properties. This strategy was implemented through the SRI scheme. Additionally, validation and application examples were included in this chapter. The results obtained with these examples are widely discussed.

5.2 Procedure for proportional loading

According to Rots (2001a), the main focus of the SLA procedure is the study of the fracture phenomenon in quasi-fragile materials, such as masonry. This procedure approximates the softening in the corresponding stress-strain curve by a saw-tooth pattern, *i.e.*, saw-tooth softening law (fig. 5.1). As its name indicates, the ALS procedure consists of performing a series of analyses in which the behaviour of the material is always linear elastic. For this purpose, after a linear analysis, the critical element is located and, then, the stiffness of that element is degraded. This procedure is repeated until the elements where it is assumed that cracks will appear are totally degraded. With this sequentially linear model, the snap-back behaviour, associated with the brittle fracture of masonry, are numerically reproduced with lower computational effort in comparison to a non-linear analysis.

This procedure starts with the discretization of the structure using solid finite elements. These elements must be 4-node quadrilaterals, to apply RI through a 1×1 quadrature in the elements where damage is assumed to occur. The material behavior is assumed to be linear elastic in each of the analyses. As initial parameters of the material, to each element

a Young's modulus, E , a Poisson's ratio, ν , and a tensile strength, f_t , are assigned. Then, the following procedure is carried out sequentially (Rots and Invernizzi, 2004):

1. Assign the external load as a reference unit load.
2. Perform a linear-elastic analysis conventionally.
3. From the results, identify the critical element *i.e.*, the element for which the principal tensile stress, σ_t , is closest to its current strength, f_t . According to Rots and Invernizzi (2004), this principal stress-strain criterion is widely accepted in the Mode I fracture mechanics of quasi-fragile materials.
4. Calculate the scale factor, λ , as the current strength divided by the principal tensile stress of the critical element (eq. 5.1).

$$\lambda = \frac{f_t}{\sigma_t} \quad (5.1)$$

5. Calculate the critical global load as the product of the scale factor by the unit load and, also, its corresponding global displacement, so that a load-displacement curve can be constructed for the structure.
6. Reduce the Young's modulus, E , and the tensile strength, f_t , of the critical element, according to a saw-tooth tensile softening stress-strain curve as described below (fig. 5.1).
7. Repeat the steps 2 to 6 for the structure for which E and f_t of the critical element were reduced.
8. With all the load-displacement configurations found in the step 5, build the overall load-displacement curve.

Finally, the deformed mesh must be plotted. According to Rots and Invernizzi (2004), these graphs reveal the location of the fracture because the series of critical weakened elements will show the largest strains, representing the width of the crack.

The success of this method depends on the way in which the stiffness and strength of the critical element is progressively reduced. This is the essence of the procedure. In a very simplified manner, E could be reduced to zero immediately after one element is selected as a critical element for the first time. However, according to Rots (2001a) this simplification benefits the mesh dependence of the results.

5.3 Saw-tooth softening law

In this method, the tensile softening stress-strain diagram is defined by the Young's modulus E , the tensile strength f_t , the shape of the diagram and the fracture energy G_f divided by the crack width h , represented by the area under the diagram (Rots and Invernizzi,

2004). Accordingly, for a linear softening diagram, the ultimate strain ε_u is expressed as in eq. 5.2.

$$\varepsilon_u = \frac{2G_f}{f_t h} \quad (5.2)$$

In the procedure described in the last section, the softening diagram is reproduced by consecutive reductions of the Young's modulus E with eq. 5.3 (Rots, 2001a).

$$E_i = \frac{E_{i-1}}{a} \quad \forall i \in \{1, 2, \dots, n\} \quad (5.3)$$

Here, i represents the current tooth in the saw-tooth diagram and a the factor for which the Young's modulus of the critical element is reduced. Furthermore, n is the amount of reductions that are applicable in total to one element until is considered as totally damaged, *i.e.*, number of teeth in the saw-tooth diagram. To avoid numerical issues, it is advisable to keep a very low residual value of Young's modulus, *e.g.* 10^{-6} times the initial Young's modulus. The reduced tensile strength, f_{t_i} , corresponding to E_i , is taken according to the envelope of the softening diagram (eq. 5.4) (Rots, 2001b).

$$f_{t_i} = \varepsilon_u E_i \left(\frac{D}{E_i + D} \right) \quad (5.4)$$

where:

$$E_i = \frac{E}{a^i} \quad D = \frac{f_t}{\varepsilon_u - \left(\frac{f_t}{E} \right)} \quad (5.5)$$

Here, D is the tangent to the stress-strain softening diagram. An example of this type of curve is included in the fig. 5.1 for the mechanical parameters included in table 5.1 considering 10 teeth and $a = 2$.

Table 5.1. Mechanical parameters considered for the stress-strain diagram of fig. 5.1

Elasticity modulus	Poisson's ratio	Tensile strength	Fracture energy	Crack width
$E = 38000$ MPa	$\nu = 0.20$	$f_t = 3.0$ MPa	$G_f = 0.06$ N/mm	$h = 5.0$ mm

In fig. 1 the formation of teeth in the approximation due to the reduction of the Young's modulus is showed. Similarly, the reduction of the tensile strength from its initial value of 3 MPa to a residual value very close to zero is observed. It should be noted that there is a clear underestimation by the approximation. This suggests that the result of the procedure is susceptible, among other factors, to the number of teeth selected.

5.4 Combined procedure of SLA with SRI

In this dissertation, a proposal to combine the SLA procedure with the application of the SRI scheme, described and validated in chapter 2, is presented. This SLA-SRI procedure is very attractive to be implemented for the following reasons:

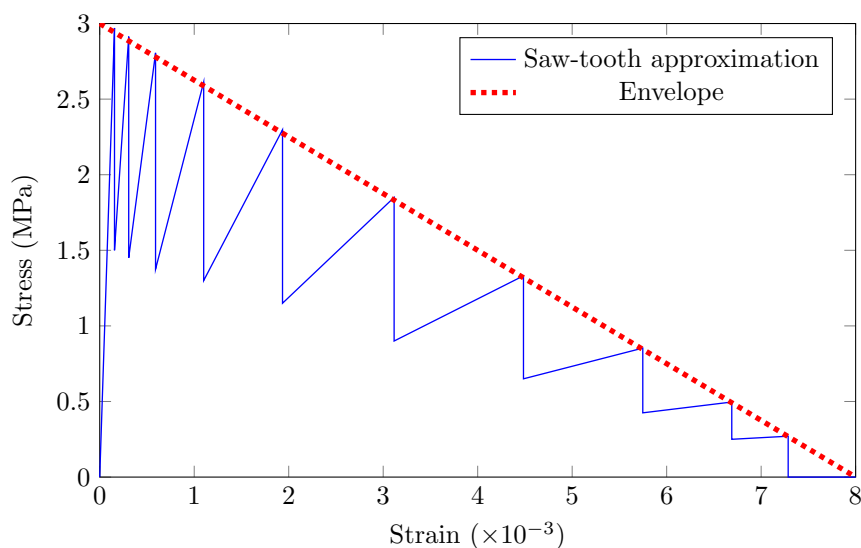


Figure 5.1. Softening in stress-strain curve (Rots, 2001b)

- As established by Rots (2001b), this SLA strategy obtains good-enough approximations with coarse meshes. This characteristic is shared with the SRI scheme, for which enrichment of results for coarse meshes were tested in chapter 2.
- In the original procedure of the SLA, reduced integration, without any stabilization, was used in the elements where cracking is expected to occur. This means that if the maximum tensile principal stress is identified at the only one integration point of certain element in the potential crack path, the stiffness and strength of that critical element is degraded. This characteristic is attractive for the SRI scheme, in which it is possible to evaluate stresses at a single integration point with numerical stability. Moreover, all the elements composing the mesh can be integrated through SRI without numerical issues.
- The study of massive masonry structures, including historic buildings, is form interest in this research. Therefore, the implementation of this SLA strategy, optimized for the structural analysis of ancient masonry, in conjunction with the SRI scheme is attractive.
- Both strategies, SLA and SRI, have the focus of being computationally economical and efficient. Therefore, by combining them, it is expected to have a strategy that is practical and efficient to apply, which offers support for fast decision making to help preserve historic buildings.

5.4.1 Numerical implementation

For numerical implementation purposes, the programming language *Python* (Van Rossum and Drake, 2009) was selected, especially because of its high compatibility with different operating systems. Furthermore, this language allows analytical integration for the

conditions imposed by a particular problem which is attractive for the SRI scheme implementation. The objective is to have an independent computational tool that allows the study of problems with this SLA-SRI strategy and that, in addition, can continue to be developed to expand its applications with new developments such as those mentioned in the introduction of this dissertation.

A flow diagram that summarizes the coded algorithm is shown in fig. 5.2. In the pre-processing stage, the *GiD* program (Ribáó et al., 2019) is used. This program is widely used by both academic and professional community dedicated to perform FEM analysis. Thus, the required algorithms were developed so that the output file of the *GiD* program (Ribáó et al., 2019) works directly as an input file for the computational tool developed in this research. Once all the mechanical parameters of the material are captured, the corresponding saw-tooth softening curve is computed and the processing stage begins by executing the SLA procedure. Finally, in the post-processing stage, both the reaction-displacement diagrams and the deformed mesh configuration at the end of the analysis are plotted and showed to the user (fig. 5.3).

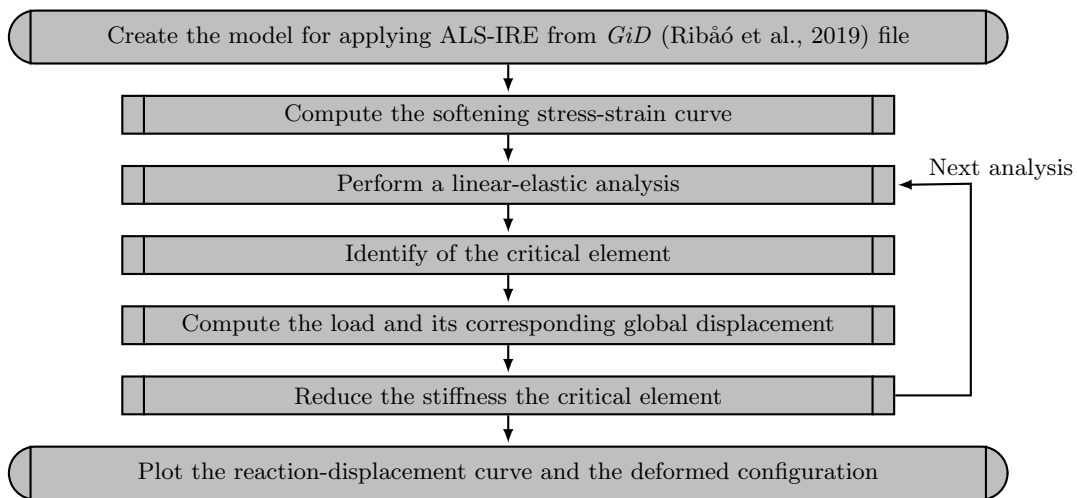


Figure 5.2. Flow diagram of the implemented algorithm

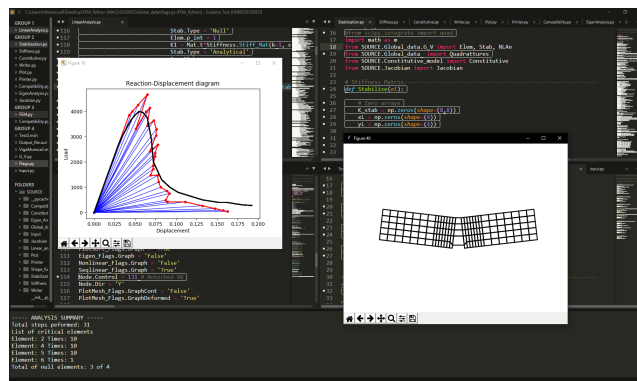


Figure 5.3. Screen capture of the developed software

5. APPLICATION THROUGH SEQUENTIALLY LINEAR ANALYSIS

The steps that were performed for this numerical implementation are as follows:

- Development of the required algorithms for the numerical evaluation of the stiffness matrix of a 4-node quadrilateral finite element employing FI, RI and SRI.
- Creation of an script for reading output files of the program *GiD* (Ribão et al., 2019) for the construction of the numerical model of a complete mesh.
- Development of a programming routine that allows the imposition of boundary conditions for the solution of a particular problem.
- Elaboration of an algorithm that performs an assembly of a global stiffness matrix.
- Elaboration of routines for plotting deformed configurations, stress fields and load-displacement diagrams.
- Creation of scripts to generate an output file and to write on screen useful information and partial results to review the status of the analysis.
- Development of the necessary algorithms for the identification of the critical element after a linear analysis and its subsequent degradation in stiffness and strength. In addition to the calculation of the scale factor to find the overall critical load and displacement.
- Development of the necessary procedure for the execution of the multiple sequential analysis required to approach a given problem.

5.4.2 Validation examples

As a validation example, a notched beam studied by Rots (2001a) is analyzed. The geometry and dimensions of the symmetric notched beam are shown in fig. 5.4.

Initially, the mesh of fig. 5.5 was built. The 4-node quadrilateral finite elements in this mesh are arranged in such a way that they benefit the beginning of the crack in the notch. For the SLA strategy, all the elements in the mesh were integrated using a FI scheme, except for the elements over the depth of the beam which were integrated using RI and, for SLA-SRI strategy, all elements were integrated using the SRI scheme but only the elements over the depth of the beam can be selected as critical elements.

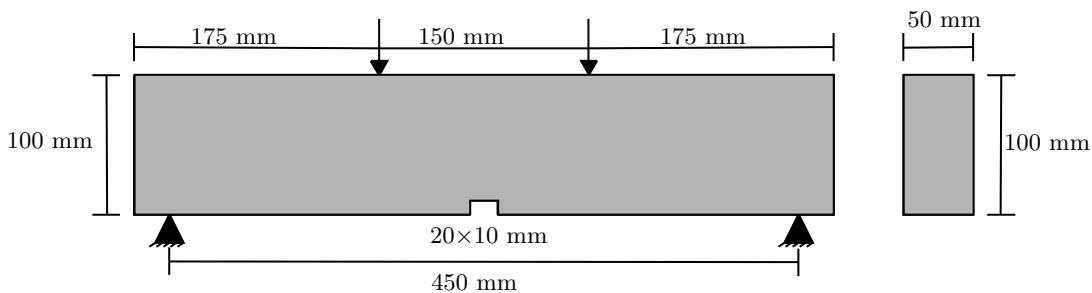


Figure 5.4. Geometry of the notched beam

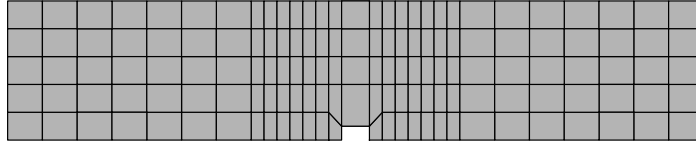


Figure 5.5. Mesh employed in the analysis of the notched beam

The mechanical properties were selected according to Rots (2001a) and summarized in table 5.2. The stress-strain curve and its saw-tooth approximation for these material properties are included in fig. 5.1 Three different analysis were performed considering 5, 10 and 20 teeth. Therefore the a factor was taken as 4, 2 and $\sqrt{2}$, for each number of teeth, respectively. The results, for both SLA and SLA-SRI, are shown in figs. 5.6, 5.7 and 5.8. In these figures, as a comparison, a reference curve was added. This curve was obtained by Rots (1993) from a non-linear softening analysis for a discrete line crack with the same parameters.

Table 5.2. Mechanical parameters considered in the analysis of the notched beam

Elasticity modulus	Poisson's ratio	Tensile strength	Fracture energy	Crack width
$E = 38000$ MPa	$\nu = 0.20$	$f_t = 3.0$ MPa	$G_f = 0.06$ N/mm	$h = 5.0$ mm

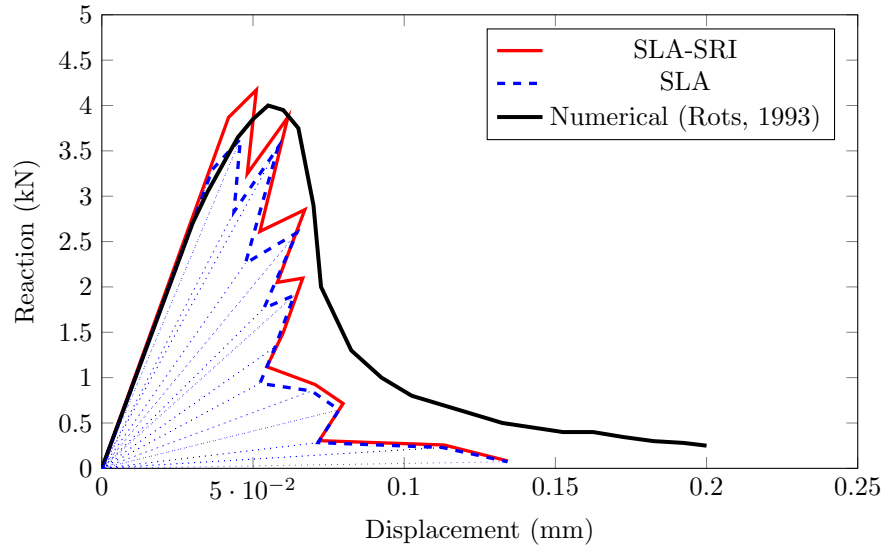


Figure 5.6. Reaction-displacement diagram for the notched beam (5 teeth)

In these figures, it can be seen that the larger number of teeth, the smoother the envelope of both SLA and SLA-SRI. Also, it can be noted that all the numerical approximations underestimate the reaction-displacement numerically obtained by Rots (1993), but the ones approximated by SLA-SRI are slightly closer to it. Finally, all the results were consistent with the ones computed by Rots (2001a). Additionally, in fig. 5.9 the deformed configuration of the notched beam is shown.

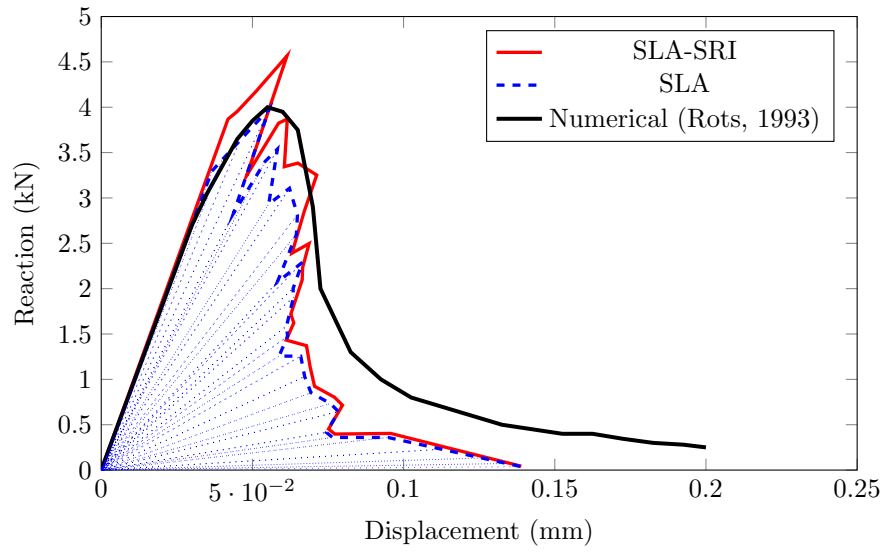


Figure 5.7. Reaction-displacement diagram for the notched beam (10 teeth)

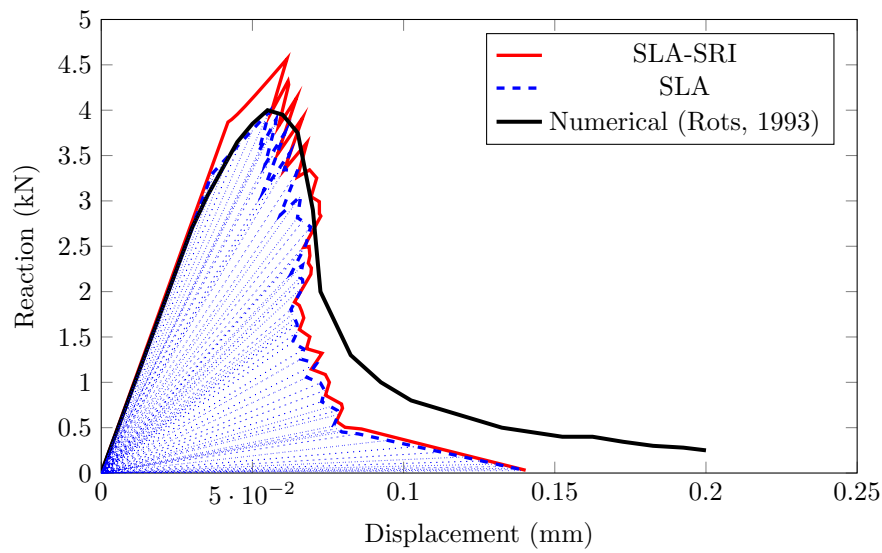


Figure 5.8. Reaction-displacement diagram for the notched beam (20 teeth)

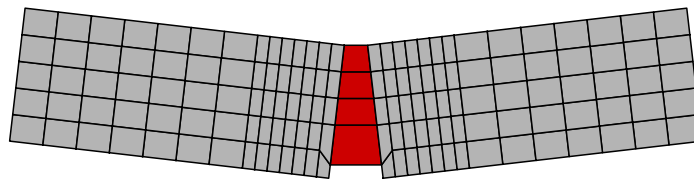


Figure 5.9. Deformed configuration of the notched beam after the SLA-SRI procedure

5.5 Mesh regularization procedure

From the results obtained in the previous section, it is clear that a mesh regularization procedure is required to overcome the effect of the mesh sensitivity in the analysis. For this reason, Rots and Invernizzi (2004) proposed a procedure based on an adjustment factor, k , that seeks to compensate the underestimation in the area in the saw-tooth softening diagram (fig. 5.10). According to Rots and Invernizzi (2004), there are three options to compensate this underestimation through the k factor. In the first one, only the tensile strength is updated through the k factor (eq. 5.6). As an alternative, instead of updating the tensile strength, only the ultimate strain is updated (eq. 5.7).

$$f_t^* = k f_t \quad (5.6)$$

$$\varepsilon_u^* = k \varepsilon_u \quad (5.7)$$

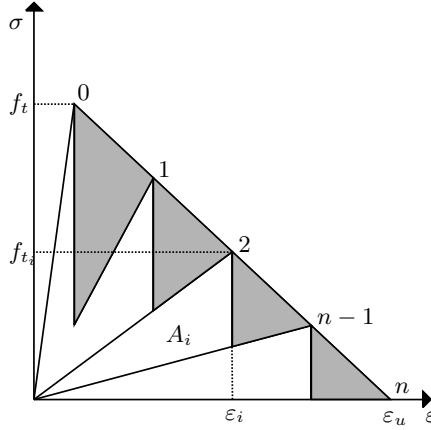


Figure 5.10. Underestimated area in the softening diagram through the saw-tooth approximation (Rots and Invernizzi, 2004)

Finally, the third option is to update both parameters, *i.e.* tensile strength and ultimate strain, employing both eqs. 5.6 and 5.7. This regularization scheme is shown in fig. 5.11 and the k factor can be obtained with eq. 5.8 (Rots and Invernizzi, 2004). In this equation, n is the number of teeth considered in the diagram.

$$k = \sqrt{\frac{G_f/h}{\sum_{i=0}^{n-1} \frac{1}{2}(f_{t_i}^2/E_i) b_i}} \quad (5.8)$$

where:

$$b_i = \begin{cases} \left(1 - \frac{1}{a}\right), & \text{if } 0 \leq i < n - 1 \\ 1, & \text{if } i = n - 1 \end{cases} \quad (5.9)$$

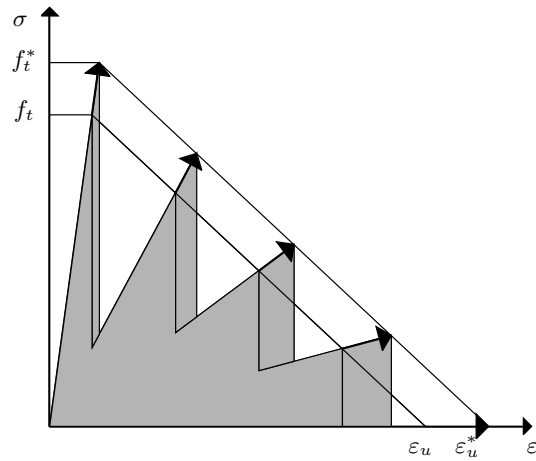


Figure 5.11. Procedure for compensating the underestimated area in the softening diagram through the saw-tooth approximation (Rots and Invernizzi, 2004)

5.5.1 Validation examples

The notched beam analyzed in the previous section was selected to be studied with this regularization procedure (table 5.2). Once again, models with 5, 10 and 20 teeth were considered, the k factors are equal to 1.35, 1.17 and 1.08, respectively (table 5.3). The results are shown in figs. 5.12, 5.13 and 5.14 for both SLA and SLA-SRI.

Table 5.3. Adjustment factors, k , for each model

Model	Adjustment factor	Tensile strength updated	Ultimate strain updated
5 teeth	$k = 1.35$	$f_t^* = 4.05$ MPa	$\epsilon_u^* = 10.8 \times 10^{-3}$
10 teeth	$k = 1.17$	$f_t^* = 3.51$ MPa	$\epsilon_u^* = 9.36 \times 10^{-3}$
20 teeth	$k = 1.08$	$f_t^* = 3.24$ MPa	$\epsilon_u^* = 8.64 \times 10^{-3}$

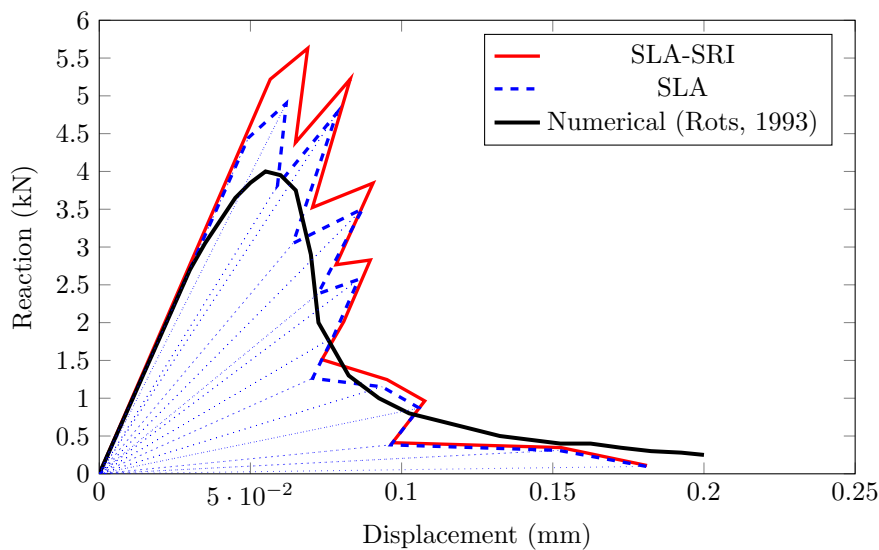


Figure 5.12. Reaction-displacement diagram for the notched beam (regularized, 5 teeth)

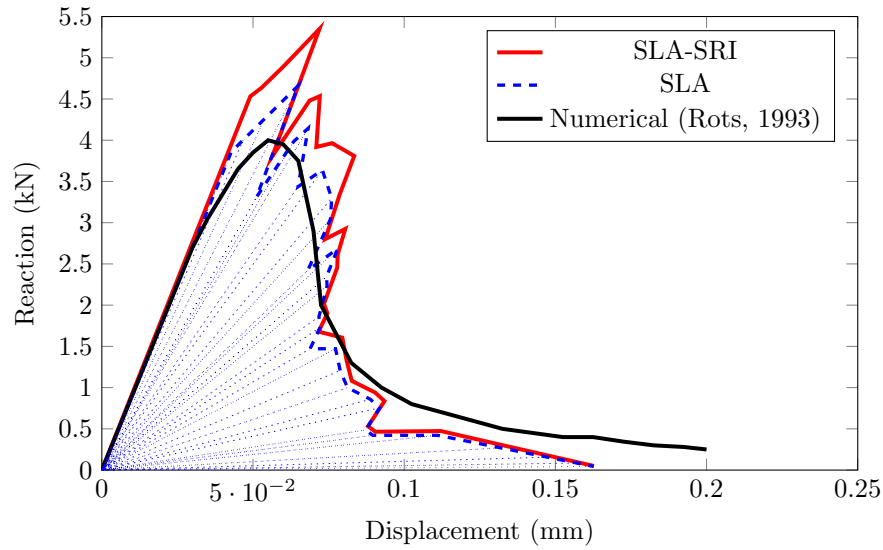


Figure 5.13. Reaction-displacement diagram for the notched beam (regularized, 10 teeth)

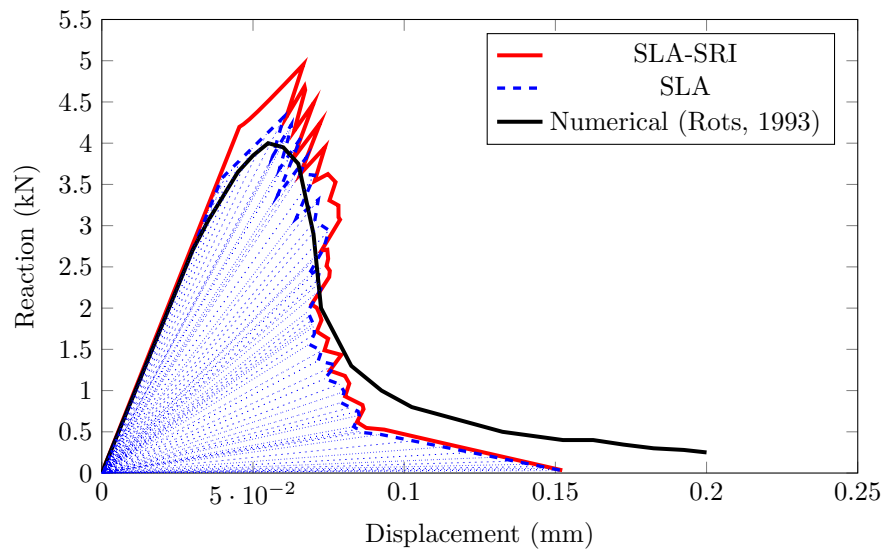


Figure 5.14. Reaction-displacement diagram for the notched beam (regularized, 20 teeth)

In these figures, it can be noted that the approximations are closer to the numerical approximation of Rots (1993) than the ones obtained in the previous section with no mesh regularization procedure, especially in the area under the curve. Nevertheless, there is an overestimation in the yield reaction and an underestimation in the last part of the curve. Finally, it can be concluded that the more the number of teeth the closer the approximation.

5.6 Application

To apply the SLA-SRI procedure, two application examples were selected. Both examples were studied by Juárez and Ayala (2010) and are ideal to be modeled with this strategy since they present a mode I failure. The first one consists of a beam for which its cross-section is variable and, in addition, have two notches. In the second example, a constant cross-section beam with a single notch is studied.

5.6.1 Variable cross-section notched beam

The first example consists on a variable cross-section beam with a double notch of 25 mm length each one, as shown in fig. 5.15. This beam is totally restrained in its left end and free in the right one in which the displacements are imposed. In the work of Juárez and Ayala (2010), this beam was analyzed through a non-linear mixed finite element formulation with an isotropic continuum damage model for the material. The mesh was built employing only 4-node quadrilateral finite elements so that the SRI scheme can be applied (fig. 5.16). All the elements in the mesh were integrated using this SRI scheme, but only the mechanical properties of the elements between the notches can be reduced.

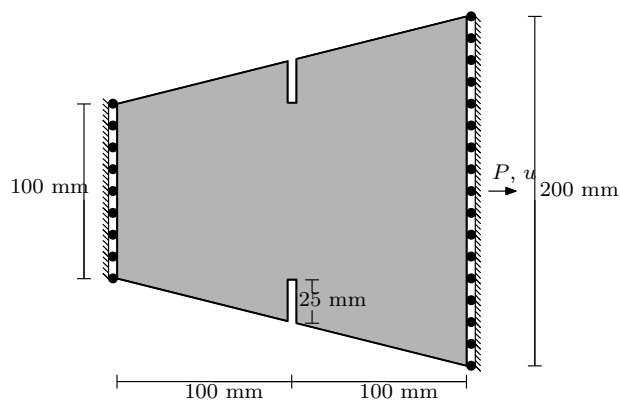


Figure 5.15. Geometry of the variable cross-section notched beam (Juárez and Ayala, 2010)

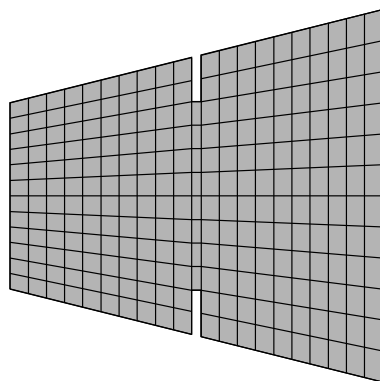


Figure 5.16. Mesh employed in the analysis of the variable cross-section notched beam

The mechanical properties of the material are the ones of table 5.4 and were selected according to Juárez and Ayala (2010). For the SLA application, 10 teeth were considered with a factor $a = 2$.

Table 5.4. Mechanical parameters considered in the analysis of the variable cross-section notched beam

Elasticity modulus	Poisson's ratio	Tensile strength	Fracture energy	Crack width
$E = 16900$ MPa	$\nu = 0.20$	$f_t = 2.4$ MPa	$G_f = 0.3$ N/mm	$h = 5.0$ mm

In fig 5.17 the reaction-displacement curves, with no mesh regularization procedure, for both SLA and SLA-SRI, are shown. Additionally, the curve obtained by Juárez and Ayala (2010) is also included for comparison purposes. Here, it can be noted a clear similarity between SLA and SLA-SRI. As expected, both curves underestimate the behaviour numerically approximated by Juárez and Ayala (2010) since no mesh regularization is considered.

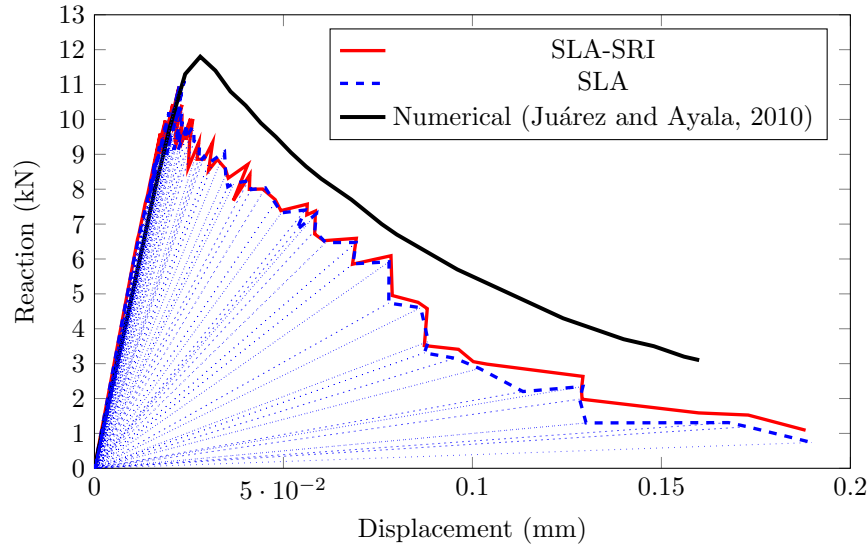


Figure 5.17. Reaction-displacement diagram for the variable cross-section notched beam

Additionally, an analysis including the mesh regularization procedure is performed. The computed k factor is equal to 1.28 and, consequentially, the regularized tensile strength is 3.08 MPa and the regularized ultimate strain is 0.064 (table 5.5).

Table 5.5. Adjustment factor, k

Model	Adjustment factor	Tensile strength updated	Ultimate strain updated
10 teeth	$k = 1.28$	$f_t^* = 3.08$ MPa	$\varepsilon_u^* = 64 \times 10^{-3}$

In fig. 5.18 it can be noted that both schemes, SLA and SLA-SRI are closer than the numerical approximation. The difference in the shape of the curves can be explained by the fact that the yield of the variable cross-section notched beam is mainly governed by a pure tensile behaviour, so the shape of the curve approximated through the SLA procedure

tends to resemble straight line. This suggests the need to employ a non-linear saw-tooth softening.

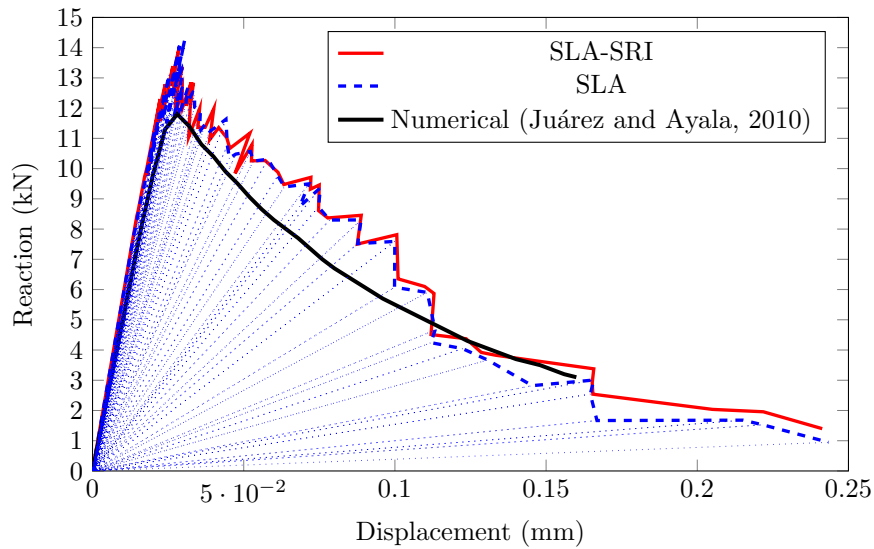


Figure 5.18. Reaction-displacement diagram for the variable cross-section notched beam (regularized)

Finally, in fig. 5.19 the deformed configuration after the SLA-SRI analysis of the beam is shown. This is similar to reported in the work of Juárez and Ayala (2010).

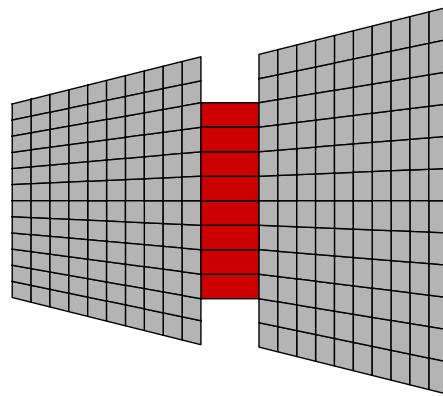


Figure 5.19. Deformed configuration of the variable cross-section notched beam

5.6.2 Notched beam

The second application example consists on a notched beam, shown in fig. 5.20, that was tested by Kormeling and Reinhardt (1983) and numerically analyzed by Juárez and Ayala (2010). The experimental tests were carried out in the Delft University of Technology and were aimed to determine the fracture energy of concrete and epoxy modified concrete. For

this purpose, several specimens, such as the shown in fig. 5.20, were tested (Kormeling and Reinhardt, 1983).

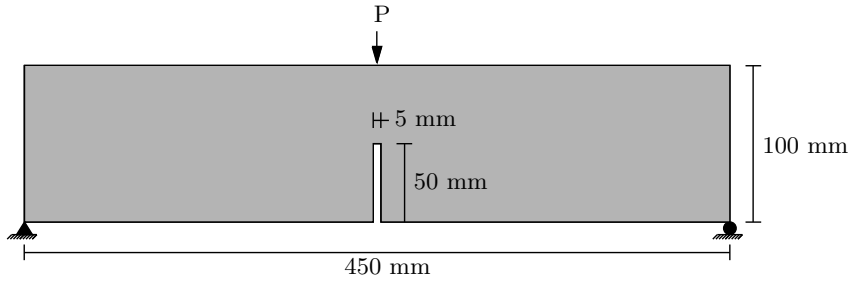


Figure 5.20. Geometry of the notched beam (Juárez and Ayala, 2010)

For the analysis through SLA and SLA-SRI, the mesh of fig. 5.21 was built. The mesh is composed only by 4-node quadrilateral finite elements. The mechanical properties for the material of table 5.6 were considered. These properties were selected according to Juárez and Ayala (2010) and Kormeling and Reinhardt (1983). For the SLA application, 20 teeth were considered with a factor $a = \sqrt{2}$.

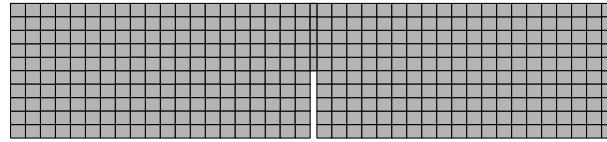


Figure 5.21. Mesh employed in the analysis of the notched beam

Table 5.6. Mechanical parameters considered in the analysis of the notched beam

Elasticity modulus	Poisson's ratio	Tensile strength	Fracture energy	Crack width
$E = 20000 \text{ MPa}$	$\nu = 0.20$	$f_t = 2.4 \text{ MPa}$	$G_f = 0.113 \text{ N/mm}$	$h = 5.0 \text{ mm}$

The reaction-displacement curves, with no mesh regularization procedure, for both SLA and SLA-SRI, are shown in fig 5.22. For comparison purposes, the curve obtained by Juárez and Ayala (2010) and the corresponding ones of the experimental tests were included. From the results, it can be noted a clear similarity between SLA and SLA-SRI and with the experimental results. Similarly to the previous example, both curves underestimate the behaviour numerically approximated by Juárez and Ayala (2010) since no mesh regularization is considered.

In fig. 5.23 the results for a mesh regularization procedure are included. Accordingly, the k factor is equal to 1.11 and the regularized tension strength is 2.65 MPa and the regularized ultimate strain is 0.02 (table 5.7).

Table 5.7. Adjustment factor, k

Model	Adjustment factor	Tensile strength updated	Ultimate strain updated
20 teeth	$k = 1.11$	$f_t^* = 2.65 \text{ MPa}$	$\varepsilon_u^* = 20 \times 10^{-3}$

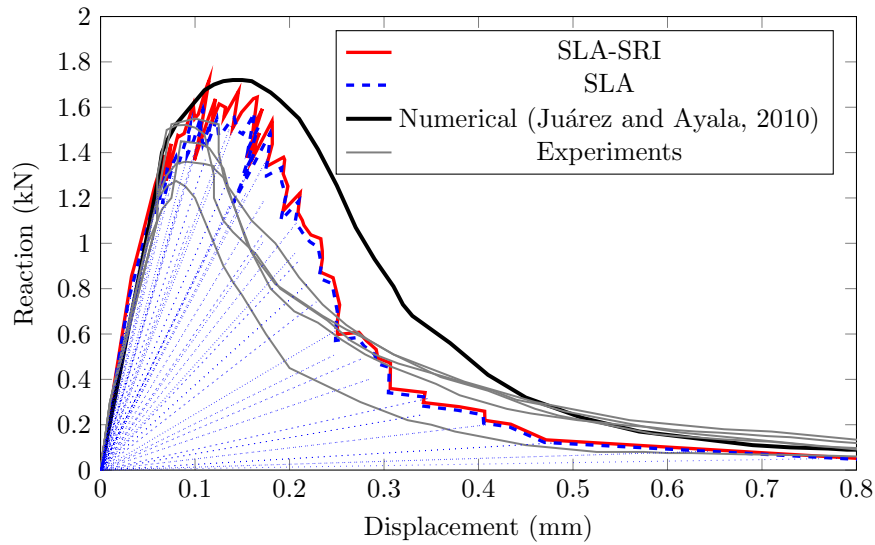


Figure 5.22. Reaction-displacement diagram for the notched beam

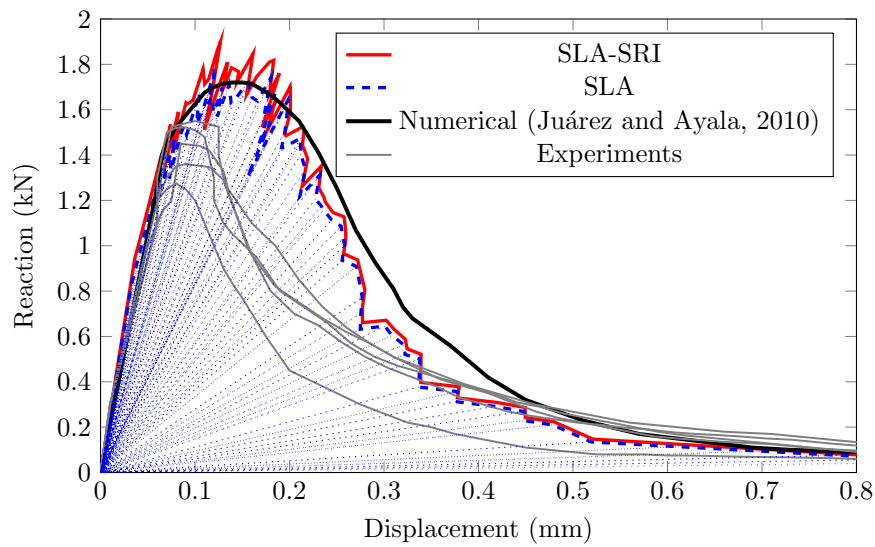


Figure 5.23. Reaction-displacement diagram for the notched beam (regularized)

From the fig. 5.23, it can be noted that both schemes, SLA and SLA-SRI, are closer than the numerical approximation also in the non-linear softening of the beam. Nevertheless, it also can be noted that the SLA approach with no mesh regularization procedure gives a better fit to the experimental tests. Finally, in fig. 5.24 the deformed configuration after the SLA-SRI analysis of the beam is shown. This is similar to reported in the work of Juárez and Ayala (2010)

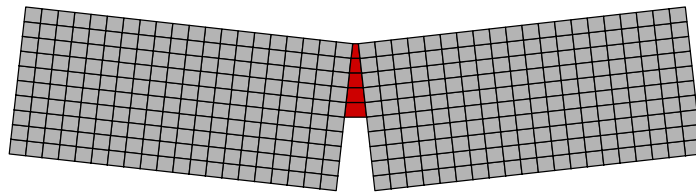


Figure 5.24. Deformed configuration of the notched beam

Conclusions

In this dissertation, a computationally efficient integration scheme for the non-linear analysis of structures was presented. The SRI scheme proposed herein, and applied to the 4-node quadrilateral finite element, successfully controls the hourglass effect by the addition of an analytically obtained stabilizer stiffness matrix to the sub-integrated one. This scheme allows a one-point constitutive model evaluation that considerably reduces the computational cost of analysis in comparison to the cost required in a conventional four-point evaluation. This SRI scheme was validated and applied through a plastic-damage constitutive model and SLA procedure.

In a first step, the strategy was reviewed at a single element, focusing in the mathematical issues generated at applying RI, generally leading to a rank-deficient stiffness matrix for the element. The proposed formulation correctly augments the rank of the one-point stiffness matrix, controls the zero-energy modes, and leads to a better representation of the linear-strain modes. Furthermore, its application is computationally economic, since no complex procedures are involved. Even though the numerical implementation of this formulation was only coded in the *FEAP* program (Taylor, 2017), it may also be successfully implemented in other software environments as the involved routines and subroutines created herein were computationally optimized and adapted to take advantage of the method.

Validation examples were included throughout the document. In these examples, interesting advantages were highlighted and discussed. For example, the considerable computational cost reduction was achieved in comparison with that of the FI conventional procedure. In fig. 6.1 are summarized the computing time comparison of seven of the examples studied in this paper. All the times showed in fig. 6.1 correspond to the same mesh density. It can be noticed an average computing-time reduction of 35.60% in this comparison. Therefore, it can be concluded that the analysis performed through SRI are around 1.55 times faster than the ones analyzed using FI for the same mesh. According to the results showed in chapter 2, this reduction of the computing time does not involve a loss of quality in the results (figs. 2.12, 2.16, 2.22 2.27 and 2.31). Also in fig. 6.1 is observed that the reduction is slightly higher when coarser meshes are used.

6. CONCLUSIONS

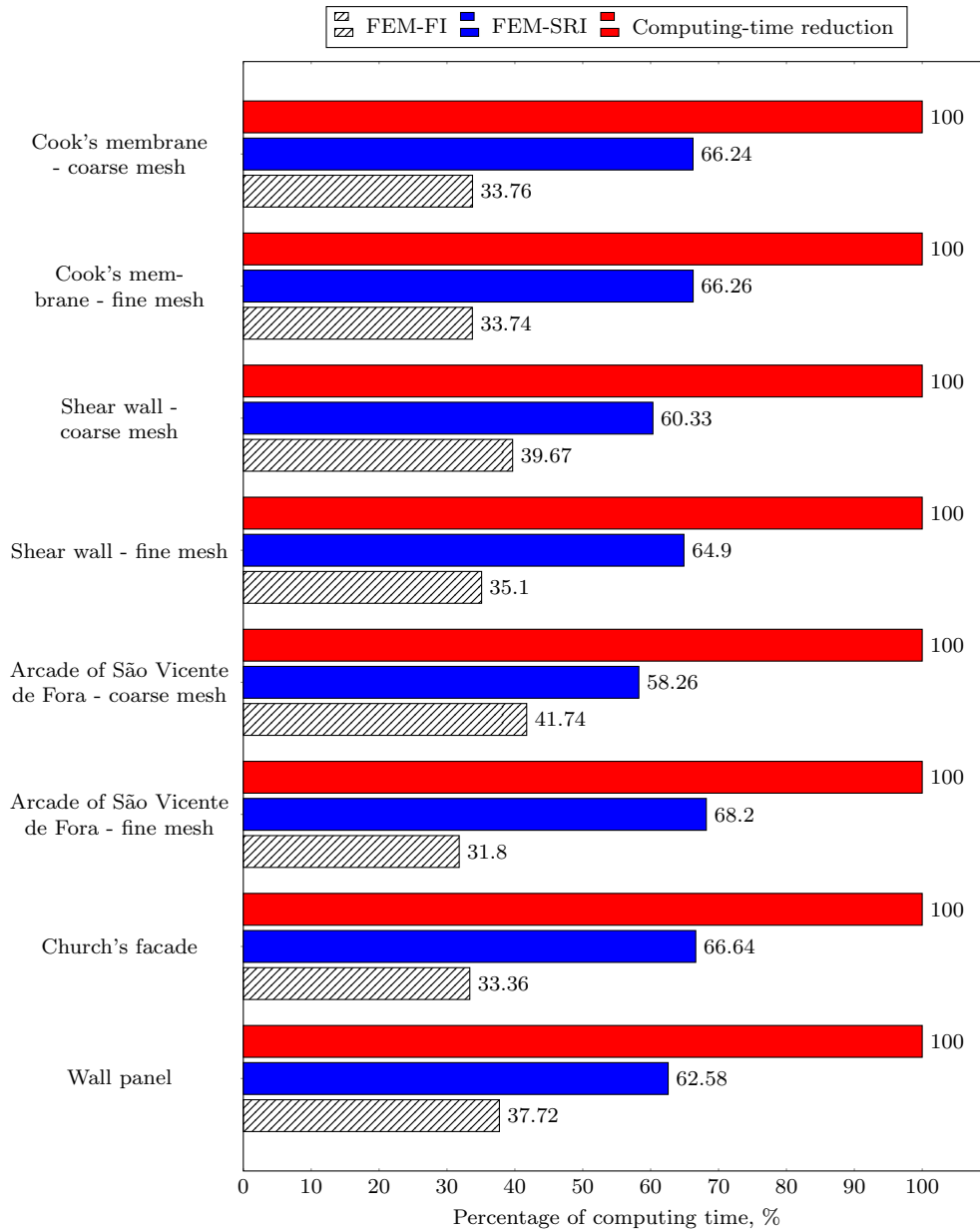


Figure 6.1. Computing-time reduction of the presented examples (comparison for same mesh density)

One of the most attractive advantage, discussed in this paper, for using the SRI scheme, is the possibility of using relative high coarse meshes in finite element non-linear analysis, which means an even higher reduction of the computational cost. One reason of this phenomenon is the improvement in the representation and the strain-energy contribution of the linear-strain deformation modes. In fig. 6.2 the computing-time reduction of four examples are included. In this figure, different mesh density are compared, *i.e.* coarser meshes for the SRI scheme and finer meshes for the FI scheme. Here, It can be noticed an average computing-time reduction of 85.75% in this comparison which means that the

SRI scheme is around 7 times faster than the FI scheme. Additionally, from figs. 2.12, 2.16, 2.22 and 2.39, it can be stated that this reduction of the computing time does not involve a loss of quality in the results. As a matter of fact, the results of the SRI scheme with coarser meshes are slightly better than the ones of FI with finer meshes.

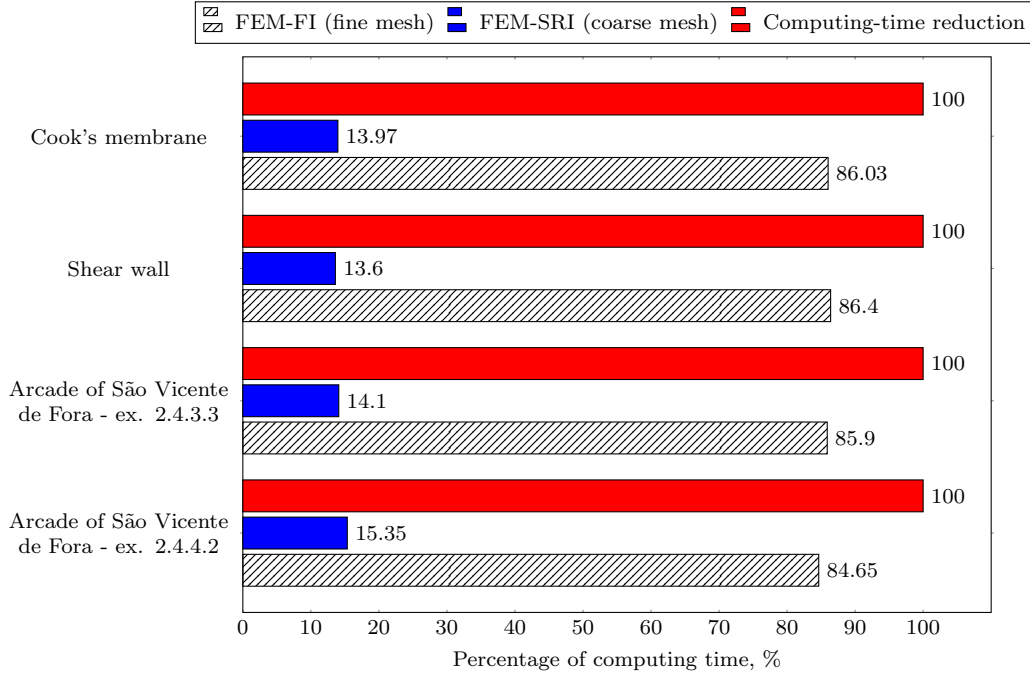


Figure 6.2. Computing-time reduction of the presented examples (comparison for different mesh density)

This reduction in computing-time opens up the possibility of analyzing complex 3D structures with this SRI scheme as the formulation here presented for 2D structures can be easily extended to 3D situations where the computational savings are more evident because the number of required integration points per element are evidently reduced. Also, taking advantage of the computational-cost reduction, this SRI scheme is attractive to be applied in dynamic analysis in which the computational demands are high.

In order to apply this SRI scheme to the analysis of masonry structures, a plastic-damage constitutive model with homogenization was implemented. This numerical implementation was also performed in the *FEAP* program (Taylor, 2017) and was optimized for being applied through the SRI scheme. In chapter 4, two application examples corresponding to shear walls were analyzed and compared to experimental results. In this examples, good-enough approximation were achieved regarding the overall behaviour of the shear walls.

As an alternative, the SRI scheme was also applied through SLA in chapter 5, SLA-SRI. This alternative was validated and compared to the original procedure of SLA, proving to be computationally efficient. The obtained results are comparable to the ones computed through a robust formulations based on the theory of damage. The program developed

6. CONCLUSIONS

for the application of this procedure represent a product of this dissertation that can be used for performing plane-stress analysis of masonry constructions.

One of the most attractive features of this SLA-SRI is the possibility of using the SRI scheme in all the elements of the mesh and not only in those where damage is assumed to occur. This may be attractive because of the reduction of computational time and the possibility of future developments in which different crack paths can be considered.

Additionally, this SLA-SRI is attractive to be improved with the inclusion of an algorithm for non-proportional loads and, in addition, with the inclusion of other softening laws, for example, non-linear behaviour and different behaviours for tension and compression. This can expand the field of application of the SLA-SRI strategy and, at the same time, can improve the quality of the approximation.

References

- Ambrosetti, C. (2000). *On the seismic behavior of a structural model of an arched monument: Numerical analysis with a friction model (in italian)*. Eng. Thesis, Politecnico di Milano, Italia.
- Amezcuca, H. R. (2016). *Formulation and numerical implementation of an improved finite element model and its application to the study of ancient masonry structures*. M. Eng Thesis, Instituto de Ingeniería, UNAM.
- Anthoine, A. (1995). Derivation of the in-plane elastic characteristics of masonry through homogenization theory. *International Journal of Solids and Structures*, 32(2):137–163.
- Bassa, B., Sabourin, F., and Brunet (2012). A new nine-node solid-shell finite element using complete 3d constitutive laws. *International journal for numerical methods in engineering*, 92(7):589–636.
- Belytschko, T. and Bachrach, W. E. (1986). Efficient implementation of the quadrilaterals with high coarse-mesh accuracy. *Computer Methods in Applied Mechanics and Engineering*, 54(3):279–301.
- Belytschko, T. and Bindeman, L. P. (1991). Assumed strain stabilization of the 4-node quadrilateral with 1-point quadrature for nonlinear problems. *Computer Methods in Applied Mechanics and Engineering*, 88(3):311–340.
- Belytschko, T., Liu, W., Moran, B., and Elkhodary, K. (2013). *Nonlinear Finite Elements for Continua and Structures*. John Wiley & Sons, Ltd.
- Belytschko, T., Ong, J., Liu, W. K., and Kennedy, J. M. (1984). Hourglass control in linear and nonlinear problems. *Computer Methods in Applied Mechanics and Engineering*, 43(3):251–276.
- Bettaieb, A. B., de Sena, J. V., de Sousa, R. A., Valente, R., Habraken, A., and Duchene, L. (2015). On the comparison of two solid-shell formulations based on in-plane reduced and full integration schemes in linear and non-linear applications. *Finite Elements in Analysis and Design*, 107:44–59.
- Bono, F., Tirelli, D., Verzelletti, G., Molina, G., and Renda, V. (1998). Shape memory alloy crossbracing of masonry walls: cyclic test of a large scale model and numerical analyses. *Workshop on Seismic Performance of Monuments*, pages 239–248.

REFERENCES

- Chávez, M. (2010). *Experimental validation of analytical models for the study of the seismic behaviour of historical structures (in spanish)*. Ph. D. Thesis, Instituto de Ingeniería, UNAM.
- Cook, R. D. (1974). Improved two-dimensional finite element. *Journal of the Structural Division*, 100(9):1851–1863.
- Cook, R. D., Malkus, D. S., and Plesha, M. E. (1989). *Concepts and applications of finite element method*. John Wiley Sons, Ltd.
- Correia, J. R., Branco, F. A., and de Brito, J. (2007). Analysis of São Vicente de Fora church, Portugal. *Proceedings of the Institution of Civil Engineers-Structures and Buildings*, 160(4):187–196.
- DeJong, M., Hendriks, M., and Rots, J. (2008). Sequentially linear analysis of fracture under non-proportional loading. *Engineering Fracture Mechanics*, 75(18):5042–5056.
- Eliáš, J., Frantík, P., and Vořechovský, M. (2010). Improved sequentially linear solution procedure. *Engineering fracture mechanics*, 77(12):2263–2276.
- Flanagan, D. P. and Belytschko, T. (1981). A uniform strain hexahedron and quadrilateral with orthogonal hourglass control. *International Journal for Numerical Methods in Engineering*, 17(5):679–706.
- Flores, F. G. (2016). A simple reduced integration hexahedral solid-shell element for large strains. *Computer Methods in Applied Mechanics and Engineering*, 303:260–287.
- Fredriksson, M. and Ottosen, N. S. (2004). Fast and accurate 4-node quadrilateral. *International Journal for Numerical Methods in Engineering*, 61(11):1809–1834.
- Ganz, H. and Thürlimann, B. (1984). *Tests on masonry walls under normal and shear loading (in german)*. Report No. 7502-4, Institute of Structural Engineering, ETH, Zurich, Zurich, Switzerland.
- GDF (2004). Complementary technical standards of the Construction code for the Federal District (in Spanish). *Official Gazzete of the Federal District, México D.F.*
- Giamundo, V., Sarhosis, V., Lignola, G., Sheng, Y., and Manfredi, G. (2014). Evaluation of different computational modelling strategies for the analysis of low strength masonry structures. *Engineering Structures*, 73:160–169.
- Giordano, A., Mele, E., and De Luca, A. (2002). Modelling of historical masonry structures: comparison of different approaches through a case study. *Engineering Structures*, 24:1057–1069.
- Invernizzi, S., Trovato, D., Hendriks, M., and Van de Graaf, A. (2011). Sequentially linear modelling of local snap-back in extremely brittle structures. *Engineering Structures*, 33(5):1617–1625.
- Juárez, G. and Ayala, A. (2010). Approximation of the failure process in solids with mixed finite elements using continuous damage (in spanish). *Revista internacional de métodos numéricos para cálculo y diseño en ingeniería*, 26(3):225–232.

-
- Kormeling, H. and Reinhardt, H. (1983). Determination of the fracture energy of normal concrete and epoxy modified concrete. *Delft University of Technology, Report*, pages 5–83.
- López, J., Oller, S., and Oñate, E. (1998). *Calculation of the masonry behaviour by means of finite elements*. Centro Internacional de Métodos Numéricos en Ingeniería.
- López, J., Oller, S., Oñate, E., and Lubliner, J. (1999). A homogeneous constitutive model for masonry. *International Journal for Numerical Methods in Engineering*, 46:1651–1671.
- Lourenço, P. B. (1996). *Computational strategies for masonry structures*. Ph. D. Thesis, TU Delft, Delft University of Technology.
- Lubliner, J., Oliver, J., Oller, S., and Oñate, E. (1989). A plastic-damage model for concrete. *International Journal of Solids and Structures*, 25:299–326.
- Lurati, F., Graf, H., and Thürlimann, B. (1990). *Experimental determination of the strength parameters of concrete masonry (in german)*. Report No. 8401-2, Institute of Structural Engineering, ETH, Zurich, Zurich, Switzerland.
- Lurati, F. and Thürlimann, B. (1990). *Tests in concrete masonry walls (in German)*. Report No. 8401-3, Institute of Structural Engineering, ETH, Zurich, Zurich, Switzerland.
- MathWorks (2019). *MATLAB Version 9.7 (R2019b)*. The MathWorks Inc., Natick, Massachusetts.
- Milani, G. and Bertolesi, E. (2017). Quasi-analytical homogenization approach for the non-linear analysis of in-plane loaded masonry panels. *Construction and Building Materials*, 146:723–743.
- Olivella, X. O. and de Saracibar, C. A. (2002). *Continuum Mechanics for Engineers (in spanish)*, volume 92. Universidad Politécnic de Catalunya.
- Oller, S. (1991). *Numerical modelling of frictional materials (in spanish)*. Centro Internacional de Métodos Numéricos en Ingeniería.
- Oller, S. (2001). *Fractura mecánica. Un enfoque global*. CIMNE.
- Oller, S., Oliver, J., Lubliner, J., and Oñate, E. (1988). A plastic-damage constitutive model for frictional materials. part i: Fundamental variables, yield and potential functions (in spanish). *Revista Internacional de Métodos Numéricos para Cálculo y diseño en ingeniería*, 4(4):397–432.
- Orduña, A., Roeder, G., and Peña, F. (2007). Seismic assessment of historical masonry constructions: comparison of three models of analysis (in spanish). *Revista de Ingeniería Sísmica, SMIS México*, 77:71–88.
- Orduña, A. (2017). Non-linear static analysis of rigid block models for structural assessment of ancient masonry constructions. *International Journal of Solids and Structures*, 128:23–35.
-

REFERENCES

- Orduña, A. (2003). *Seismic Assessment of Ancient Masonry Structures by Rigid Blocks Limit Analysis*. PhD thesis, Universidade do Minho, Portugal.
- Page, A. W. (1978). Finite element model for masonry. *Journal of the Structural Division*, 104(8):1267–1285.
- Pari, M., Swart, W., van Gijzen, M. B., Hendriks, M., and Rots, J. G. (2020). Two solution strategies to improve the computational performance of sequentially linear analysis for quasi-brittle structures. *International Journal for Numerical Methods in Engineering*, 121(10):2128–2146.
- Pari, M., Van de Graaf, A., Hendriks, M., and Rots, J. (2021). A multi-surface interface model for sequentially linear methods to analyse masonry structures. *Engineering Structures*, 238:112123.
- Pegon, P., Pinto, V. P., and Gérardin, M. (2001). Numerical modeling of stone-block monumental structures. *Computers and Structures*, 79(22):2165–2181.
- Pelà, L., Cervera, M., and Roca, P. (2013). An orthotropic damage model for the analysis of masonry structures. *Construction and Building Materials*, 41:957–967.
- Pietruszczak, S. and Niu, X. (1992). A mathematical description of macroscopic behaviour of brick masonry. *International journal of solids and structures*, 29(5):531–546.
- Pinto, A. V., Verzeletti, G., Molina, F. J., and Plumier, C. (1998). *Seismic Tests on the S. Vicente de Fora Model*. Report, National Laboratory for Civil Engineering, Lisbon.
- Quinteros, R. D., Bellomo, F., Nallim, L. G., and Oller, S. (2014). A model for the structural analysis of masonry behaviour through homogenization techniques (in spanish). *Mecánica Computacional*, 33(1):1253–1269.
- Raijmakers, T. M. and Vermeltfoort, A. T. (1992). *Deformation controlled tests in masonry shear walls (in Dutch)*. Report, TNO-Bouw, Delft, The Netherlands.
- Ribàó, R., Pasenau, M., Escolano, E., Ronda, J., Gonzalez, L., and Rosa, E. (2019). *GiD v14 user manual*. CIMNE, Barcelona.
- Rots, J. (1993). The smeared crack model for localized mode-i tensile fracture. *Numerical Models for Fracture Mechanics*, pages 101–113.
- Rots, J. (2001a). The role of structural modelling in preserving amsterdam architectural city heritage. *Historical Constructions*, pages 685–696.
- Rots, J. (2001b). Sequentially linear continuum model for concrete fracture. *Fracture mechanics of concrete structures*, 13:831–839.
- Rots, J. and Invernizzi, S. (2004). Regularized sequentially linear saw-tooth softening model. *International Journal for Numerical and Analytical Methods in Geomechanics*, 28:821–586.
- Rots, J. G., Belletti, B., and Invernizzi, S. (2008). Robust modeling of rc structures with an “event-by-event” strategy. *Engineering Fracture Mechanics*, 75(3-4):590–614.

- Sarhosis, V. (2011). *Computational modelling of low bond strength masonry*. Ph. D. Thesis, University of Leeds, UK.
- Simo, J. C. and Taylor, R. L. (1986). A return mapping algorithm for plane stress elastoplasticity. *International Journal for Numerical Methods in Engineering*, 22(3):649–670.
- Slobbe, A., Hendriks, M., and Rots, J. (2012). Sequentially linear analysis of shear critical reinforced concrete beams without shear reinforcement. *Finite Elements in Analysis and Design*, 50:108–124.
- Taylor, R. L. (2017). *FEAP, A Finite Element Analysis Program, Programmers Manual*. Department of Civil and Environmental Engineering, University of California at Berkeley.
- Van Rossum, G. and Drake, F. L. (2009). *Python 3 Reference Manual*. CreateSpace, Scotts Valley, CA.
- Vermeltfoort, A. and Raijmakers, T. (1993). *Deformation Controlled Tests in Masonry Shear Walls. Part 2 (in Dutch)*. Report, TNO-Bouw, Delft, The Netherlands.
- Yu, C., Hoogenboom, P., and Rots, J. (2018). Incremental sequentially linear analysis to control failure for quasi-brittle materials and structures including non-proportional loading. *Engineering Fracture Mechanics*, 202:332–349.
- Zienkiewicz, O. C. and Taylor, R. L. (2013). *The finite element method. Volume 1: Its basis and fundamentals (seventh edition)*, volume 1. Elsevier.
- Zucchini, A. and Lourenço, P. B. (2009). A micro-mechanical homogenisation model for masonry: Application to shear walls. *International Journal of Solids and Structures*, 46(3-4):871–886.